Phase boundary mapping for exploring new thermoelectric Zintl compounds

Thesis by
Saneyuki Ohno

In Partial Fulfillment of the Requirements for the
degree of
Doctor of Philosophy

CALIFORNIA INSTITUTE OF TECHNOLOGY
Pasadena, California

2017
Defended June 2nd, 2017

Saneyuki Ohno
ORCID: 0000-0001-8192-996X

Acknowledgements

Firstly, I would like to thank my advisor, Prof. Jeff Snyder. None of this work would have been possible without his insightful guidance, advice, and help based upon his expert knowledge and experience. One of the greatest achievements of my research life both at Caltech and Northwestern in the past five years is to work with such an open-minded, relaxed, patient, and passionate boss. Moving a lab, preparing in two days, and giving the first presentation at my first international conference, and performing PhD research, in general, were all difficult challenges, but they became highlights of this joyful and fulfilling journey because of his support.

The former and current members of Caltech/Northwestern thermoelectric group taught and provided me with what I needed to make progress. I thank Prof. Alex Zevalkink for patiently guiding my first year of research and teaching me all of the basics of thermoelectrics. Thanks to Dr. Sabah Bux for providing wonderful opportunities to collaborate with NASA-JPL on thermoelectric Zintl compounds. The time shared both inside and outside of the lab with Stephen Dongmin Kang and Taeyeon Lee, who also moved from LA to Chicago, was absolutely precious and Stephen's comments and ideas significantly enriched this thesis. I also thank Dr. Umut Aydemir for helping me with his rich knowledge of chemistry especially in structure analysis. Prof. Teruyuki Ikeda, Tristan Day, and Dr. Fivos Drymiotis taught me how to handle the rapid hot pressing systems. Prof. Wolfgang Zeier taught me the fundamentals of crystallography and FullProf. The numerous samples prepared by Kazuki Imasato, Miles David Kurtz, and Michael Joseph Wucher, transport measurements conducted by Sevan Chanakian at JPL, and the phase diagram calculation provided by Shashwat Anand made my research possible. I thank Ian Witting, Sam Miller, and Max Wood for their frequent help in improving the outputs. I would also like to thank all of the lab mates both at Caltech and Northwestern who have contributed to create a relaxed, cheerful, positive, and productive atmosphere within the lab, which was essential to accomplish this work.

I would like to acknowledge the NASA Science Mission Directorate's Radioisotope Power Systems Thermoelectric Technology Development for research funding, and Japan Student Service Organization (JASSO) for five years of financial support. I am grateful to collaborators around the world: Hiromasa Tamaki at Panasonic Corporation (Japan), who provided defect calculations, Jan Pöhls at Dalhousie University (Canada), who conducted thermal characterizations, Maximilian Kai at

Northwestern University (US), who made band structure calculations, and Stefan Maier at CRISMAT (France) for preparation of $BaBiTe_3$.

I owe a lot to the friends that I've made both at Caltech and Northwestern as well, in particular my classmates Chris, Stefan, Eric, Ho-il, Albert, Ho-Hsuan, Hwang Fu, and Horie, for collaboration to help overcome tough coursework, and my teammates, Yu, Yoshimi, Phil, Leon, Enrique, Juba, Cataclysmics, and Team Iran, for playing soccer together.

I would like to thank my families, both parents and in-laws, for their support and encouragement. The consistent supplies (especially foods and drinks) all the way from Japan have definitely enriched my life as a graduate student.

Lastly, I would like to give my greatest thanks to Saori, my wife, for her understanding and continuous support. Even when she was first told that I had decided to leave Japan for purely personal challenges, she smiled and said, "as you like", and has supported me for over five years. Without her, my time as a graduate student would have been joyless and unbearable.

Abstract

Understanding and controlling the defect chemistry of bulk materials can vastly increase the opportunities for discovering highly efficient thermoelectrics. Good thermoelectrics are degenerate semiconductors and there are two types: *n*-type thermoelectrics, whose charge carriers are electrons, and *p*-type thermoelectrics conducting holes as carriers. Although normally one type can attain superior thermoelectric properties to the other depending on the electronic band structure of a material, a formation of the unfavorable defects sometimes prevents a material from obtaining desired type. Similarly, even if the desired carrier type is realized, the Fermi level, which is a measure of the carrier density, could be kept from the optimum due to the formation of compensating defects. It has been known from growing binary semiconductors for electronics and optoelectronics such as GaAs and GaN that a growth condition can substantially alter the defect concentration of resulting samples. This is primarily due to the change in the reference atomic chemical potentials, but such defect engineering has not been utilized for the bulk thermoelectric research, resulting in overlooking the promising candidate materials.

In this work, we established an experimental methodology to fully explore all the accessible variations in chemical potentials of a target phase and demonstrated its implementation. Although a pursuance of purity of samples to be measured is a common experimental concept in solid-state chemistry, in practice, a small single-phase region of semiconductors allows samples to have certain amount of impurities. Since different multi-phase equilibria have discrete chemical potentials, only when all the boundaries of the multi-phase equilibria around target phase are mapped out in nominal composition space are the measured transport properties of resulting samples properly correlated with their atomic chemical potential.

Utilizing this experimental concept we call "phase boundary mapping", we have identified the mechanism of obtaining the superior *n*-type conduction in Mg_3Sb_2-based compounds. To achieve their exceptionally high thermoelectric figure-of-merit (zT = 1.5 at 750 K), the formation energy of Mg-vacancy needs to be suppressed with excess Mg but this condition had been missing for over 80 years due to the absence of experimental concept to fully investigate properties of a material. Implementing phase boundary mapping has also allowed an inexpensive thermoelectric Zintl compound $Ca_9Zn_{4+x}Sb_9$ to be one of the best thermoelectrics in the intermediate temperature range (zT = 1.1). We have also successfully reduced the

carrier concentration of $Yb_9Zn_{4+x}Sb_9$, which was originally thought to be impossible, leading to zT increased by a factor of five.

Published contents and contributions

1. Nasrin Kazem, Weiwei Xie, **Saneyuki Ohno**, Alexandra Zevalkink, Gordon Miller, G. J. Snyder, Susan Kauzlarich "High Temperature Thermoelectric Properties of the Solid-Solution Zintl Phase $Eu_{11}Cd_6Sb_{12-x}As_x$ ($x < 3$)" *Chemistry of Materials* **26**, 1393 (2014), DOI: 10.1021/cm403345a

   S. O. participated in analysis the thermal transport with point defect scattering model, and manuscript preparation

2. **Saneyuki Ohno**, Alex Zevalkink, Yoshiki Takagiwa, Sabah K. Bux, G. Jeffrey Snyder "Thermoelectric properties of the $Yb_9Mn_{4.2-x}Zn_xSb_9$ solid solution" *Journal of Materials Chemistry A* **2**, 7478 (2014), DOI: 10.1039/C4TA00539B

   S. O. participated in designing the research project, sample synthesis, structure and elemental analysis, electronic and thermal transport measurements, analysis of the experimental data, and writing of manuscript.

3. Alex Zevalkink, Jessica Swallow, **Saneyuki Ohno**, Umut Aydemir, Sabah Bux, and G. Jeffrey Snyder "Thermoelectric properties of the $Ca_5Al_{2-x}In_xSb_6$ solid solution" *Dalton Transactions* **43**, 15872 (2014), DOI: 10.1039/C4DT02206H

   S. O. participated in analysis the thermal transport with point defect scattering model, and manuscript preparation.

4. Umut Aydemir, Alex Zevalkink, Alim Ormeci, Heng Weng, **Saneyuki Ohno**, Sabah Bux, G. Jeffrey Snyder "Thermoelectric properties of the Zintl phases $Yb_5M_2Sb_6$ (M = Al, Ga, In)" *Dalton Transactions* **44**, 6767-6774 (2015), DOI: 10.1039/C4DT03773A

   S. O. participated in electronic and thermal transport measurements, and analysis of experimental data.

5. Nasrin Kazem, Antonio Hurtado, Fan Sui, **Saneyuki Ohno**, Alexandra Zevalkink, G. Jeffrey Snyder, and Susan M. Kauzlarich "High Temperature Thermoelectric Properties of the Solid-Solution Zintl Phase $Eu_{11}Cd_{6-x}Zn_xSb12$" *Chemistry of Materials* **27**, 4413-4421 (2015), DOI: 10.1021/acs.chemmater.5b01301

   S. O. participated in electronic and thermal transport measurements, analysis of experimental data, and manuscript preparation.

6. Nasrin Kazem, Julia V. Zaikina, **Saneyuki Ohno**, G. Jeffrey Snyder, and Susan M. Kauzlarich "Coinage-Metal-Stuffed $Eu_9Cd_4Sb_9$: Metallic Compounds with Anomalous Low Thermal Conductivities" *Chemistry of Materials* **27**, 7508-7519 (2015), DOI: 10.1021/acs.chemmater.5b03808

   S. O. participated in electronic and thermal transport measurements, analysis of experimental data, and manuscript preparation.

7. Umut Aydemir, Jan-Hendrik Pöhls, Hong Zhu, Geoffroy Hautier, Saurabh Bajaj, Zachary M. Gibbs, Wei Chen, Guodong Li, **Saneyuki Ohno**, Danny Broberg, Stephen Dongmin Kang, Mark Asta, Gerbrand Ceder, Mary Anne White, Kristin Persson, Anubhav Jain and G. Jeffrey Snyder "$YCuTe_2$: a member of a new class of thermoelectric materials with $CuTe_4$-based layered structure" *Journal of Materials Chemistry A* **4**, 2461-2472 (2016), DOI: 10.1039/C5TA10330D

   S. O. participated in electronic and thermal transport measurements, analysis of experimental data, and manuscript preparation.

8. **Saneyuki Ohno**, Umut Aydemir, Maximilian Amsler, Jan-Hendrik Pöhls, Sevan Chanakian, Alex Zevalkink, Mary Anne White, Sabah K. Bux, Chris Wolverton, and G. Jeffrey Snyder "Achieving $zT > 1$ in inexpensive Zintl phase $Ca_9Zn_{4+x}Sb_9$ by phase boundary mapping" *Advanced Functional Materials* **27**, 1606361 (2017) DOI: 10.1002/adfm.201606361

   S. O. participated in designing the research project, sample synthesis, structure and elemental analysis, electronic and thermal transport measurements, analysis of the experimental data with phase boundary mapping, and writing of manuscript.

9. Ami Nomura, Ken Kurosaki, Seongho Choi, Manabu Ishimaru, Atsuko Kosuga, Thomas Chasapis, **Saneyuki Ohno**, G. Jeffrey Snyder, Yuji Ohishi, Hiroaki Muta, and Shinsuke Yamanaka "Chalcopyrite $ZnSnSb_2$: A Promising Thermoelectric Material" *Submitted*

   S. O. participated in measurements and analysis of optical absorption and Hall effect, and manuscript preparation.

10. **Saneyuki Ohno**, Kazuki Imasato, Shashwat Anand, Hiromasa Tamaki, Stephen Dongmin Kang, Hiroki K. Sato, Tsutomu Kanno and G. Jeffrey Snyder "Phase

boundary mapping to obtain *n*-type Mg_3Sb_2-based thermoelectrics" *Submitted*

S. O. participated in designing the research project, sample synthesis, structure and elemental analysis, electronic and thermal transport measurements, analysis of the experimental data with phase boundary mapping, and manuscript preparation.

11. Stefan. Maier, **Saneyuki Ohno**, Guodong Yu, Geoffroy Hautier, Stephen Dongmin Kang, Thomas Chasapis, David Berthebaud, G. Jeffrey Snyder and Franck Gascoin "Chemical bonding, defect chemistry and thermoelectric properties of *n*-type $BaBiTe_{3-x}Se_x$ (x = 0, 0.05 and 0.1)" *Submitted*

    S. O. participated in microscope and elemental analysis, electronic and thermal transport property measurements, analysis of the experimental data with effective m^* model, and manuscript preparation.

Contents

List of Figures

List of Tables

C h a p t e r 1

Introduction

In the winter of 1820, an Estonian-German physicist, Johann Christoph Seebeck, announced that he had found a new *magnetic* effect at the session of Berlin Academy of Science.[1] Seebeck placed a magnetic needle compass in the circuit of two dissimilar metals, heated one of the joints, and observed a deflection of the needle of a compass (See Fig.1.1). Based on the observation, he concluded that there is a linear relationship between the compass angle and the temperature difference between hot and cold joints, and tried to explain it by magnetic polarization of two metals.[2] Soon after, his theory was rectified by Danish physicist Hans Christian Oersted.[3] The deflection of a compass needle was actually caused by the magnetic field induced from electric current, which Oersted defined as "Thermoelectricity". Thermoelectricity refers to the current produced by an electric potential built up due to a temperature difference. Later, this effect was recognized as the Seebeck effect. The discovery of the Seebeck effect led to historical findings: the Peltier effect (1834) is the inverse effect of the Seebeck effect (electric current induces temperature gradient),[4] and the renowned Ohm's law (1826), which was found by a German physicist, Georg Simon Ohm, who applied the Seebeck effect to obtain constant voltage from the temperature difference between ice and boiling water.[5]

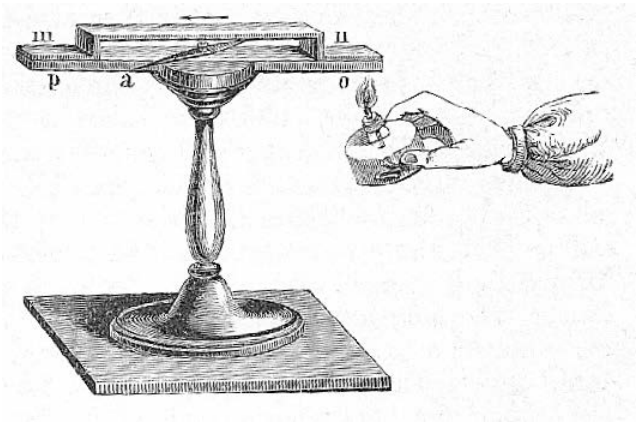

Figure 1.1: A classic instrument for demonstrating the thermoelectric effect. From Adolphe Ganot, *Traité élémentaire de physique expérimentale et appliquée et de meteorologie: illustré de 568 belles gravures sure bois intercalées dans le texte* (Paris: L'auteur-éditeur, 1859). p.707

About 200 years later, thanks to robustness, scalability, and high reliability, solid-state thermoelectric generators converting heat directly into electricity are used as power sources on Mars rovers such as Curiosity and space crafts for deep space exploration, like Voyagers I and II.[6] Thermoelectric generators are also considered to be one of the key technologies to realize a society "that is able to satisfy its needs without diminishing the chance of future generations."[7] Over 60% of the energy generated in the US is lost, mostly as waste heat, similar to other industrialized countries such as Japan;[8] thus harvesting even a fraction of it with thermoelectric devices could save a significant amount of energy.

The intense studies on thermoelectrics, especially in the past decade, have raised the efficiency of thermoelectric generators to over 9%.[9] However, despite the long history of thermoelectrics, the efficiency is still low compared to other sustainable energy sources and too expensive for widespread usage in the society. While a large portion of cost ineffectiveness of thermoelectric devices arise from the restricted ability of the heat exchanger,[10] a critical bottleneck of the device and cost efficiency is the poor performance of thermoelectric materials themselves. Therefore, exploration of new thermoelectric materials and discovery of new strategies to enhance the properties of existing materials are essential.

1.1 Thermal energy conversion and efficiency

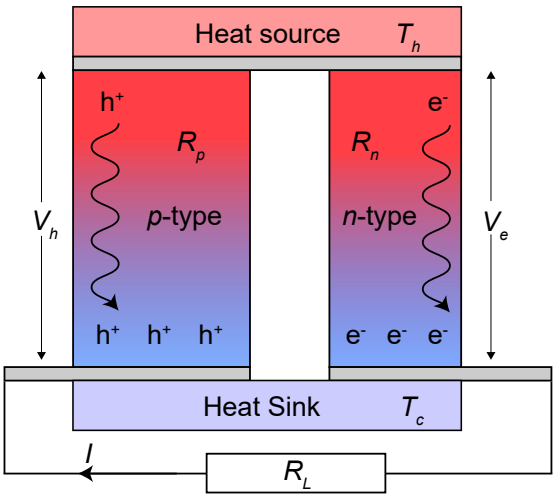

Figure 1.2: Schematic image of a thermoelectric generator. A pair of *p*-type and *n*-type thermoelectric materials is a minimum unit of the thermoelectric generator.

If one opens up a thermoelectric generator, numerous pairs of *n*-type and *p*-type ther-

moelectric materials (legs) joined by a conducting strips can be seen. A schematic illustration of a basic unit, which consists of a pair of thermoelectric legs, is shown in Fig.1.2. Applying a temperature gradient across the legs causes the charge carriers (electrons in n-type and holes in p-type) in thermoelectric materials to diffuse from the hot side to the cold side and produce an electric potential in each leg. The voltage between the two ends is proportional to the temperature difference across each substance, and the proportionality coefficient is defined as Seebeck coefficient, α,

$$\alpha = -\frac{\Delta V}{\Delta T}. \tag{1.1}$$

The sign of α is positive when the *e.m.f.* causes a current flow from cold side to hot side (p-type; left side in Fig.1.2; $\alpha_p = \frac{|V_h|}{\Delta T}$, where $\Delta T = T_h - T_c$), and negative when it is from hot to cold (n-type; right side in Fig.1.2; $\alpha_n = -\frac{|V_e|}{\Delta T}$).[11] The absolute value of the Seebeck coefficient is called thermopower ($|\alpha|$). In contrast to metals, which are normally used in thermocouples to produce only a tiny voltage (*e.g.* 0.9 μV/K for W at 300 K),[12] here the optimized semiconductors for thermoelectric application can generate hundreds of microvolts per degree. When a material contains both p- and n-type carriers, the generated thermopower by the Seebeck effect will be compensated and the net electric potential will become small. Therefore, degenerate semiconductors which possess an energy gap to have largely asymmetric p- and n-type carrier densities as well as a good electrical conductivity are favorable for good thermoelectrics.

In order to understand the basic principles for thermoelectric research, we shall calculate an efficiency of a simple thermoelectric device shown in Fig. 1.2 with a traditional method.[13–16] Here we assume the electrical resistivities (ρ_p and ρ_n), thermal conductivities (κ_p and κ_n), and Seebeck coefficients (α_p and α_n) of each materials are constants within the legs. Electrical resistances (R_p and R_n) and thermal conductances (K_p and K_n) of each legs can be described with areas of cross sections (S_p and S_n) and lengths ($l_p = l_n = l$) of each legs (See Fig. 1.2):

$$R = R_p + R_n = (\frac{\rho_p}{S_p} + \frac{\rho_n}{S_n})l \tag{1.2}$$

$$K = K_p + K_n = \left(\kappa_p S_p + \kappa_n S_n\right)\frac{1}{l} \tag{1.3}$$

$$KR = \kappa_p\rho_p + \kappa_n\rho_n + \kappa_p\rho_n\frac{S_p}{S_n} + \kappa_n\rho_p\frac{S_n}{S_p}. \tag{1.4}$$

Since the *e.m.f.* caused by the Seebeck effect is $V = V_h + V_e = \alpha_p\Delta T - \alpha_n\Delta T$, the power ($w$) delivered to the load, R_L, is

$$w = I^2R_L = \left[\frac{(\alpha_p - \alpha_n)(T_h - T_c)}{R_p + R_n + R_L}\right]^2 R_L. \tag{1.5}$$

Considering the Peltier effect associated with an electric current (I) and that half of the joule heating in legs goes back to the source, the efficiency η_w can be described as the ratio of w to the energy absorbed from hot side of the device.

$$\begin{aligned}\eta_w &= \frac{w}{(\alpha_p - \alpha_n)IT_h + (K_p + K_n)(T_h - T_c) - \frac{1}{2}I^2(R_p + R_n)} \\ &= \frac{T_h - T_c}{T_h}\cdot\frac{M}{1 + M + \frac{(1+M)^2}{T_h}\frac{KR}{\alpha^2} - \frac{1}{2}\frac{\Delta T}{T_h}},\end{aligned} \tag{1.6}$$

where M is the ratio of the load resistance to the sum of the resistances of legs $\left(M = \frac{R_L}{R_p+R_n}\right)$. According to Eq. 1.6, hot side and cold side temperatures, M, and $\frac{KR}{\alpha^2}$ $(= \frac{1}{Z})$ are the quantities that determine the efficiency of thermoelectric devices. The necessary condition to obtain the best possible efficiency is to have minimum KR by finding an optimum ratio of S_p and S_n to minimize the thermal absorption. This is achievable by choosing proper materials and geometry of the device. A larger area of cross section or shorter leg can reduce R but increase K while a smaller cross section and longer leg tend to have lower K but R will be increased accordingly. Therefore, the length of legs and cross sections have to be optimized. When they are optimized ($l_pS_n/l_nS_p = \sqrt{\kappa_p\sigma_p/\kappa_n\sigma_n}$), Z becomes

$$\begin{aligned}Z &= \frac{\alpha^2}{KR} \\ &= \frac{\alpha^2}{(\sqrt{\kappa_p\rho_p} + \sqrt{\kappa_n\rho_n})^2}.\end{aligned} \tag{1.7}$$

With fixed Z, T_h, and T_c, the maximum efficiency, η_{max}, can be calculated through a straightforward calculation of $\frac{\partial\eta}{\partial M} = 0$. The optimum M is then obtained as $M_{opt} = \sqrt{1 + Z\overline{T}}$, where $\overline{T} = \frac{T_h+T_c}{2}$, which gives the maximum efficiency of

$$\eta_{max} = \frac{T_h - T_c}{T_h} \cdot \frac{\sqrt{1 + Z\overline{T}} - 1}{\sqrt{1 + Z\overline{T}} + \frac{T_c}{T_h}}. \tag{1.8}$$

In the end, the maximum efficiency becomes a product of the Carnot efficiency ($\frac{T_h - T_c}{T_h}$; reversible factor) and a function of $Z\overline{T}$ (irreversible factor). $Z\overline{T}$ is called a dimensionless figure of merit and, as $Z\overline{T}$ increases, the irreversible factor in η_{max} monotonically increases. Although this $Z\overline{T}$ is a "device" figure of merit which consists of the properties of two legs, a figure of merit for a "material" can be defined as a similar form:

$$zT = \frac{\alpha^2}{\kappa\rho}T. \tag{1.9}$$

Conventionally, capital Z is used for the device figure of merit and lower-case z is used for the material figure of merit.[14] With a material zT, the optimum local reduced efficiency ($\eta_{r,opt}$: an optimized irreversible factor of the local conversion efficiency) can be obtained by $T_h/T_c \to 1$,[17]

$$\eta_{r,opt} = \frac{\sqrt{1 + zT} - 1}{\sqrt{1 + zT} + 1}. \tag{1.10}$$

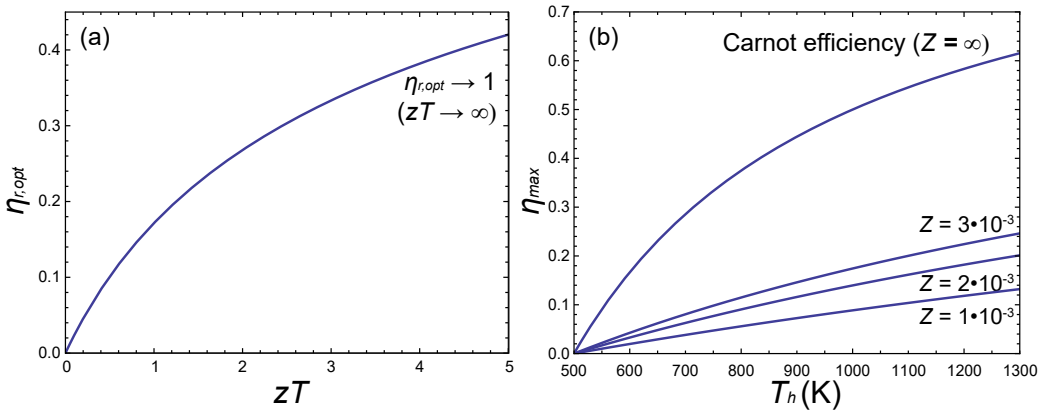

Figure 1.3: The monotonically increasing local and device efficiencies as a function of figure of merit. (a) When zT is infinitely high, the irreversible factor becomes unity, and the efficiency becomes reversible (Carnot efficiency). (b) The higher $Z\overline{T}$ the legs have, the higher efficiency the device achieve.

The larger zT a material has, the higher local efficiency it can achieve. Fig. 1.3(a) shows the irreversible factor of a local efficiency, which monotonically increases

as zT increases. When zT is infinitely large, $\eta_{r,opt}$ becomes unity and the total efficiency becomes identical to the Carnot efficiency. Material with zT greater than unity are considered as practical thermoelectric material while the highest reported zT of the bulk material is about 2.[18, 19]

Fig.1.3(b) shows the T_h dependency of the total device efficiency as a function of Z. Here the temperature of the heat sink is fixed at 500 K (T_c = 500K). A device with $Z = 2\times10^{-3}$ can have $Z\overline{T} = 1$ when T_h = 1000 K. The range of the temperature shown in Fig.1.3(b) is about the same as the practical temperature range of the thermoelectric generators for Mars rovers and space crafts (500 K to 1300 K). These generators for space applications are called radioisotope thermoelectric generators (RTG), containing $^{238}PuO_2$ as a heat source and radiating heat into outer space as a heat sink. The efficiency of the current RTGs (called Multi-Mission Radioisotope Thermoelectric Generator, or MMRTG) utilized in the latest Mars rover, Curiosity, is only 6 to 7 %.[6] The next generation RTG, with a thermoelectric Zintl compound first reported in the research shown in Chapter 5 combined with other Zintl compounds, is now under development at NASA-JPL. Segmenting materials possessing different maximum temperatures for figure of merit could achieve efficiency as high as 17 % if properly implemented.

One might wonder how the device efficiency can be calculated when the segmentation or temperature dependencies in transport properties exists for the devices with segmentation or temperature dependent thermoelectric properties can exactly be calculated.

Here, to treat segmentation and temperature dependency of materials properties properly, it is briefly discussed how to obtain the exact device efficiency (η_{max}) from each material's thermoelectric transport properties. To calculate the exact η_{max}, we need to consider one more constraint. While $\eta_{r,opt}$ (Eq.1.10) gives the best possible local reduced efficiency at a given temperature, the "true" efficiency ($\eta_{r,true}$) can be slightly different due to this constraint arising from "relative current density", u, which is defined as the ratio of the electrical current density to the heat flux by thermal conduction. Reformulating the efficiency in terms of this u, $\eta_{r,true}$ can be expressed as

$$\eta_{r,true} = \frac{u\frac{\alpha}{z}\left(1 - u\frac{\alpha}{z}\right)}{u\frac{\alpha}{z} + \frac{1}{zT}}. \tag{1.11}$$

Based on this reformulation, $\eta_{r,true}$ can be described as an intensive parameter derivable from thermodynamic state functions. Interested readers can learn detailed derivation in ref.[17] At a given temperature, $\eta_{r,true}$ becomes a function of u, and the u maximizing $\eta_{r,true}$ is referred to as compatibility factor, s,

$$s = \frac{\sqrt{1+zT}-1}{\alpha T}. \tag{1.12}$$

When $u = s$, $\eta_{r,true}$ is optimized and becomes identical to the $\eta_{r,opt}$ at a given temperature. However, once the initial condition is fixed, u over the entire temperature range is uniquely determined through a simple ordinal differential equation of the heat equation (see ref.[20]). When $u = s$ over the entire temperature range, the efficiency can reach the theoretical maximum but, in practice, it is not possible due to the temperature dependency of material's properties. There is no analytical expression to obtain the best initial u to maximize $\eta_{r,true}$ but the u giving the maximum efficiency at highest temperature can be acquired numerically. η_{max} can be formulated with relative current densities at heat source and sink by

$$\eta_{max} = 1 - \frac{\alpha_c T_c + \frac{1}{u_c}}{\alpha_h T_h + \frac{1}{u_h}}. \tag{1.13}$$

One can find the u maximizing this efficiency at a desired temperature giving the optimum u for the system. The device ZT can be calculated back from this η_{max} with Eq.1.8 if necessary.

It is important to note that utilizing the relative current density is a way not only to compute the exact efficiency of the thermoelectric device, but also to provide a guideline for choosing the materials for segmentation. Just segmenting thermoelectric materials with high zT is not alway preferable to achieve higher device efficiency because of the constraint by u. Since u for a system is uniquely determined by the initial condition, when each segmented material has substantially different optimum u, which is s, it is possible the segmentation can even negatively effect the total device efficiency. Segmenting materials with similar s is required to enhance the efficiency.[20]

One of the ultimate goals of thermoelectric research is to realize a thermoelectric generator with high efficiency. To construct an efficient thermoelectric generator, the compatibility factor becomes key to enhancing the device efficiency by segmentation. However, to take full advantage of segmentation with the knowledge of compatibility factor, we need to have enough choices of materials with high zT. "It is very easy to make a bad battery out of a good material, but it is impossible to make a good battery out of a bad material." This is a statement made by Bo Brummerstedt Iversen in the annual meeting of Danish Battery Society in 2015.[21] The same thing can be said for thermoelectric devices and it is important to develop better thermoelectric materials to boost efficiency. As discussed in this section, zT is a matrix to evaluate the performance of a material as thermoelectric. Starting with the following section, we will discuss the strategy to examine and enhance the "potential" of thermoelectric materials.

1.2 Examine a potential as a thermoelectric

The higher the zT a material possesses, the better the thermoelectric performance is. However, the best possible zT for a material can be realized only when the interdependent physical quantities are balanced to be optimized.[22] In the expression of zT, it is important to recall that there are two contributions to the thermal conductivity if there is no bipolar effect. One is an electronic portion (κ_e) and the other one is a contribution from the lattice (κ_L). Therefore, the expression of zT becomes

$$zT = \frac{\alpha^2\sigma}{\kappa_e + \kappa_L}T. \tag{1.14}$$

In Eq. 1.14, there are three components that are dependent on each other *via* the majority carrier concentration; α, ρ (= $1/\sigma$, where σ is electrical conductivity), and κ_e. Fig.1.4 shows the interdependency of those physical quantities on the carrier concentration. As the carrier density increases, thermopower decreases while electrical conductivity and electronic contribution to thermal conductivity increase. As a consequence, the optimum (best possible) zT is often attained when the majority carrier concentration is around 10^{19} to 10^{21} cm^{-3}. Since zT is dependent on the majority carrier concentration as mentioned above, even when zT of a material determined by experiments is low, optimization of the majority carrier concentration can drastically enhance the thermoelectric performance of that material.

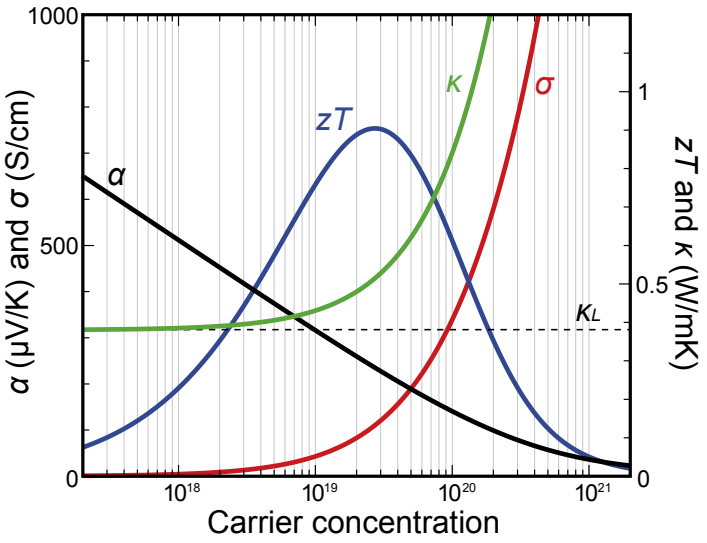

Figure 1.4: Interdependency of physical quantities contributing to zT. Good thermoelectric materials are typically semiconductors which have carrier concentration around 10^{19} to 10^{21} cm^{-3} so that the properties can strike the balance to have optimum zT. The curve for each properties is generated based on the experimental results of the thermoelectric material, $Ca_9Zn_{4+x}Sb_9$ at 775 K, as will be discussed in Chapter 5.

Effective m^* model

While the figure of merit zT, which indicates the maximum efficiency of a material as a thermoelectric, can readily be calculated from the experimentally obtained transport properties, the "potential" of the investigated material as a thermoelectric cannot be predicted unless an appropriate model is applied. There are some simple and useful models available to examine the "potential" of materials as thermoelectrics.[23–27] One of the powerful models is called the effective m^* model, where m^* is an effective mass. The electronic transport properties are determined by the states near the band edge, which can typically be well described with an effective mass. To the first order, the dispersion around the band edge can be considered as parabolic for most band conductors. Since an effective mass is a slowly changing function, it can be a good way to collect measured quantities and transform them into a metric that characterizes the band structure. In addition, it is eminently advantageous, especially for ones synthesizing and measuring materials in the lab, to have a tool to examine the "potential" of the material as a guide for experiments without conducting computational calculations, even if the model is accurate only to the first order. Judging from the conclusion, this effective m^*

model has been applied to many different systems and confirmed to be very useful for planning experiments (*e.g.* determining the doping direction for optimization) or for understanding the transport phenomena (*e.g.* investigating the effect of band offset, multi-band conduction, or mixed scattering).[28–35]

Here we briefly discuss how the effective m^* model can be used to predict a material's "potential". The following equations are obtained through Boltzmann transport theory within the effective m^* model assuming the acoustic phonon scattering as the dominant scattering mechanism. This assumption of scattering is, in general, sufficient for most thermoelectrics utilized above room temperature. $F_i(\eta)$, k_B, e, and h are the Fermi-Dirac integral function, Boltzmann constant, electron charge, and Plank constant, respectively.

$$F_i(\eta) = \int_0^\infty \frac{x^i}{1+\exp(x-\eta)}dx \tag{1.15}$$

$$\alpha(\eta) = \frac{k_B}{e}\left[\frac{2F_1(\eta)}{F_0(\eta)} - \eta\right] \tag{1.16}$$

$$n_H(\eta) = 4\pi\left(\frac{2m_S^* k_B T}{h^2}\right)^{3/2}\frac{F_{1/2}(\eta)}{r_H} \tag{1.17}$$

$$\mu_0 = \frac{e\tau_0}{m_C^*} = \frac{\sigma}{en_H}\frac{2F_0(\eta)}{F_{-0.5}(\eta)} = \mu_H(\eta)\frac{2F_0(\eta)}{F_{-0.5}(\eta)} \tag{1.18}$$

$$\kappa(\eta) = \kappa_L + \kappa_e(\eta) = \kappa_L + L(\eta)\sigma(\eta)T \tag{1.19}$$

$$L(\eta) = \left(\frac{k_B}{e}\right)^2\frac{3F_0(\eta)F_2(\eta) - 4F_1(\eta)^2}{F_0(\eta)^2}. \tag{1.20}$$

Experimentally measured thermopower can determine the reduced chemical potential ($\eta(= E_F/k_BT)$ where E_F is the Fermi level) of the investigated sample by Eq. 1.16. With this η and measured Hall carrier concentration (n_H), the effective mass (m_S^*) can be obtained. This m_S^* is called Seebeck mass since it is calculated from measured α and n_H through Eqs. 1.16 and 1.17 (r_H is the Hall factor). The other important value is a mobility parameter (μ_0) which can be obtained from the measured Hall mobility by Eq. 1.18. τ_0 is a part of carrier relaxation time independent

of energy (*e.g.* $\tau_E = \tau_0(E/k_BT)^{-1/2}$ when acoustic phonon scattering is dominant) and m_C^* is a harmonic average of masses along each direction. This mobility parameter is a descriptor of the conductivity with respect to a given band structure and Fermi level. When there is only one parabolic band in the real electronic band structure contributing to the transport, $m_C^* = m_S^*$. Larger m_C^* leads to higher Seebeck coefficient but lower mobility, which results in lower conductivity. Once m_S^* and μ_0 are obtained from experimental data, then $\alpha(\eta)$ and $\sigma(\eta)$ (= $\mu_H(\eta)en_H(\eta)$) can be calculated as a function of η within the model. The total thermal conductivity can also be obtained as a function of η ($\kappa(\eta)$) as shown in Eqs. 1.19 and 1.20 with the lattice contribution to the thermal conductivity obtained at a given temperature. $L(\eta)$ in Eq. 1.19 and 1.20 is a Lorenz number. Since the carrier concentration is a function of η, all the transport properties can be scaled as a function of n_H instead of η, demonstrated by the curves in Fig. 1.4 being calculated with this method.

Material quality factor

Here, to introduce a physical parameter indicating the material's "potential" as a thermoelectric, we shall go back to the expression of figure of merit zT. Based on the knowledge of the effective m^* model, we can redefine the expression of zT as a function of only η and B.

$$\begin{aligned} zT(\eta, B) &= \frac{\alpha(\eta)^2\sigma(\eta)}{\kappa_L + \kappa_e(\eta)}T \\ &= \frac{\alpha(\eta)^2\sigma(\eta)}{\kappa_L + L(\eta)\sigma(\eta)T}T \\ &= \frac{\left(\frac{2F_1(\eta)}{F_0(\eta)} - \eta\right)^2}{3\left(\frac{F_2(\eta)}{F_0(\eta)}\right) - 4\left(\frac{F_1(\eta)}{F_0(\eta)}\right)^2 + \frac{3\sqrt{\pi}}{4}(F_0(\eta)B)^{-1}}, \end{aligned} \tag{1.21}$$

where

$$\begin{aligned} B &= 2e\left(\frac{k_B}{e}\right)^2\left(\frac{2\pi m_e k_B}{h^2}\right)^{3/2}\frac{\mu_0(m_S^*/m_e)^{3/2}}{\kappa_L}T^{5/2} \\ &\approx 4.322\times10^{-6}\ \frac{\mu_0(m_S^*/m_e)^{3/2}}{\kappa_L}T^{5/2}. \end{aligned} \tag{1.22}$$

This dimensionless factor B is called the "material quality factor"[1]. As is evident, all the physical quantities of a material are now included in B. Once this B is fixed, the predicted zT within this model can readily be calculated for different η as shown in Fig. 1.5. The best possible zT that a material of interest can reach with optimum η is solely dependent on B and it monotonically increases with increasing B. Finding optimum η corresponds to carrier concentration optimization. Therefore, B is a value that can properly assess the material's potential even before η optimization. Another merit to acknowledge B is that the potential of a material can be assessed without a Hall effect measurement, which is required to obtain m_S^* and μ_0 separately. The η of the material of interest can be estimated by Eq. 1.16 and zT can be obtained through typical measurement of α, σ, and κ. Plugging η and zT into Eq. 1.21 or just finding the point of (η, zT) in Fig. 1.5(b), one can easily obtain B without doing the full analysis like the one shown in Fig.1.4. This is a powerful method to quickly examine the potential of the material when one does not have an access to a high temperature Hall effect measurement system or a Hall measurement is not reliable for some reason (*e.g.* metallic samples with small Hall voltage; see Chapter 3).

1.3 Strategies of thermoelectric research

Material quality factor is a descriptor of a material's "potential" as a thermoelectric and is eminently useful when considering the effective strategies of thermoelectric research. The numerator of B is called weighted mobility ($\mu_0(m_S^*/m_e)^{3/2}$), and the denominator is the lattice thermal conductivity (κ_L). Therefore, the strategies of thermoelectric research can be classified into three parts.

1) Enhance the weighted mobility

2) Suppress the lattice thermal conductivity

3) Optimize η to obtain best possible zT

[1]The coefficient of B in Eq. 1.22 can differ depending on the formalism. Here we use a mobility parameter defined by Eq. 1.18. One might find a different definition of B using classical mobility, resulting in the coefficient of 5.745×10^{-6}.[36] Historically, this concept is introduced by Chasmar and Stratton in 1959.[37] Since then, some similar parameters called β parameter,[38] material parameter,[36] and quality factor [39] are reported but these are fundamentally all the same. The important thing is that all of the physical parameters are separable from the reduced chemical potential to be independently assessed.

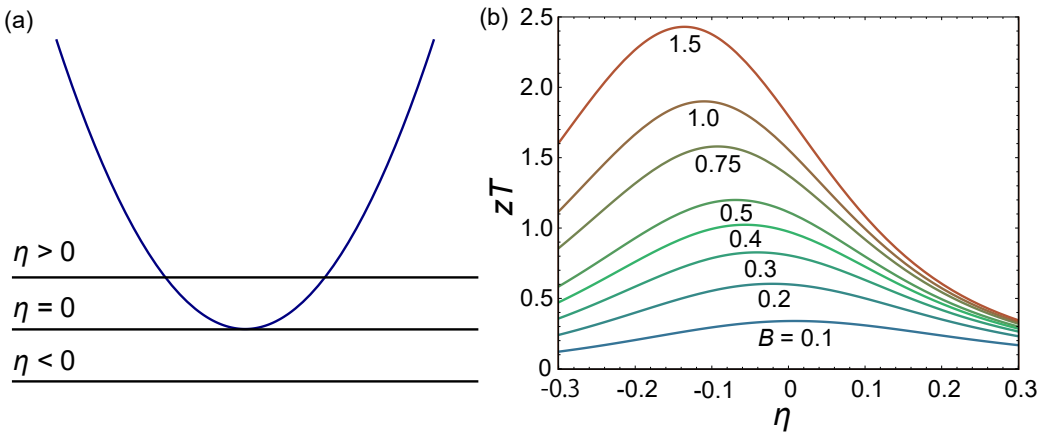

Figure 1.5: The relation between η, zT, and B. (a) Schematic of the effective m^* model. Reduced chemical potential η indicates the position of the Fermi level relative to a band with a constant m^*. Metals have η greater than zero, insulators have η less than zero, and good thermoelectrics have η around zero. (b) Material quality factor (B) dependency of zT as a function of η. Peak zT is obtained around $\eta = 0$. The higher the B is, the higher the best possible zT becomes.

1) Enhance the weighted mobility

One might think that increasing thermopower will simply result in larger B (or zT), but this is not the case. Since thermopower is dependent on m_S^*, as shown in Eq.1.23, under the effective m^* model with acoustic phonon scattering, a material with larger m_S^* (heavier or flatter band edge) can possess larger thermopower than the one with smaller m_S^* (lighter or sharper band edge) when T and n are fixed.

$$\alpha = \frac{8\pi^2 k_B^2}{3eh^2} m_S^* T \left(\frac{\pi}{3n}\right)^{2/3}. \tag{1.23}$$

However, a heavier band edge leads to lower carrier mobility, resulting in the reduction of electrical conductivity. This is why the weighted mobility should be considered.

Utilizing the effect of band convergence is a great strategy for enhancing the weighted mobility.[40] Here, one should remember that there are two different masses, m_S^* and m_C^*. These are dependent on each other *via* the valley degeneracy, N_v, and the effective anisotropy factor, $K^* = \left(\frac{m_b^*}{m_C^*}\right)^{3/2}$, where m_b^* is a geometric average of masses along each direction, as shown below:[26]

$$N_v K^* = \left(\frac{m_S^*}{m_C^*}\right)^{3/2}. \tag{1.24}$$

For the sake of simplicity, here we assume $K^* = 1$, which means there is no carrier pocket anisotropy. Under this assumption, the relation between m_S^* and m_C^* becomes

$$m_S^* = N_v^{2/3} m_C^*. \tag{1.25}$$

Therefore, increasing the valley degeneracy of N_v can enhance m_S^* without any detrimental effect on m_C^*, rising the weighted mobility to boost B.[2] Under the assumption of $K^* = 1$, m_C^* becomes identical to the single valley density of states mass m_b^*. The interested reader can refer to ref. [26] for more details on the effect of the effective anisotropy factor (K^*) to B. In short, higher K^* is the better for thermoelectrics. The effect of enlarged N_v has been confirmed in variety of systems such as PbTe,[40, 41] Bi_2Te_3,[42] SnTe,[43] Mg_2Si,[44] Skutterudites,[45] Half Heuslers,[46] and Zintl compounds[47, 48]. Many computational efforts have screened materials utilizing N_v as one of the strategies.[49, 50]

Comparison of *n*-type and *p*-type Mg_3Sb_2-based compounds discussed in Chapter 4 is a perfect example to understand the effect of enhanced weighted mobility *via* band convergence. It has long been believed that Mg_3Sb_2 and other compounds in the family with the same structure are persistently *p*-type semiconductors. However, a report in the fall of 2016 has shown *n*-type properties of Mg_3Sb_2-based compounds with extraordinarily high zT.[47] According to the computational band structure calculation, the valley degeneracy of the conduction band edge is $N_v = 6$, in contrast to the valence band edge which only has $N_v = 1$. Although the single valley density of states mass (m_b^*) of the conduction band edge is reported to be slightly larger (μ_0 for conduction band can be smaller than that of *p*-type),[47] the increase in the weighted mobility is experimentally observed by samples synthesized at Northwestern. It shows that *n*-type Mg_3Sb_2 possesses three times higher weighted mobility than *p*-type (45 cm^2/s for *n*-type and 15 cm^2/s for *p*-type). By achieving *n*-type conduction utilizing the conduction band edge, the increase in degeneracy counteracts the

[2] This valley degeneracy N_v is sometimes replaced by N_v^*, which is the effective valley degeneracy which considers the partial contributions from bands with slight offset. In that case, N_v explicitly indicates the number of identical, isolated Fermi surfaces.

decrease in μ_0, resulting in a larger weighted mobility. This means that Mg_3Sb_2-based compounds ultimately have a higher potential for *n*-type thermoelectrics compared to *p*-type.

Another common way to enhance weighted mobility is simply by increasing mobility. One might expect that an increase in the carrier mobility is a consequence of the reduction in the effective mass, which results in lowering the Seebeck coefficient and weighted mobility. However, the benefit from increased mobility can compete with the negative impact on the Seebeck coefficient, with the result being a function of the effective mass dependency of the relaxation time. Under the assumption of acoustic phonon scattering (deformation potential scattering) with a single valley electronic band structure, the energy independent term of carrier relaxation time (τ_0) has the following temperature and m_S^* dependency:[51, 52]

$$\tau_0 \propto \frac{1}{(m_S^* T)^{\frac{3}{2}}}. \tag{1.26}$$

Therefore, at a given temperature (see Eq. 1.18)

$$\mu_0 \propto \frac{1}{(m_S^*)^{\frac{5}{2}}}. \tag{1.27}$$

One good example is a study of $Yb_9Mn_{4.2-x}Zn_xSb_9$ solid solution shown in Chapter 6. Zn substitution on the Mn site results in a large reduction in effective mass, leading to enhancement of the potential as a thermoelectric material.

2) Suppress the lattice thermal conductivity

The lattice thermal conductivity in a given direction can be described by the integration over the product of the spectral heat capacity ($C_s(\omega)$), phonon group velocity ($v_g(\omega)$), and phonon relaxation time ($\tau(\omega)$) with respect to the frequency as shown in Eq. 1.28.[53]

$$\kappa_L = \frac{1}{3}\int_0^{\omega_{max}} C_s(\omega) v_g(\omega)^2 \tau(\omega) d\omega. \tag{1.28}$$

There are two major way of reducing κ_L. The first is by increasing the scattering rate of phonons, for instance by introducing disorder to reduce τ, and the second is by utilizing a complex unit cell to reduce the v_g^2 contribution. When there are

several mechanisms scattering phonons, the resulting effect can be described by the sum of the inverse phonon relaxation times (Matthiessen's rule):

$$\tau^{-1} = \sum_i \tau_i^{-1} \tag{1.29}$$

The typical scattering mechanisms that limit relaxation times in thermoelectrics are Umklapp (phonon-phonon) scattering ($i = U$), point defect scattering ($i = PD$), boundary scattering ($i = B$), dislocation core scattering($i = DC$), and dislocation strain scattering($i = DS$).

Umklapp scattering (phonon-phonon scattering) is often the dominant scattering mechanism at high temperature ($> \Theta_D$: Debye temperature) and becomes more prominent as temperature increases:

$$\tau_U^{-1} = \frac{(6\pi^2)^{1/3}}{2} \frac{\bar{M} v_g v_p^2}{k_B V^{1/3} \gamma^2 \omega^2 T}. \tag{1.30}$$

Here V is the atomic volume, $\bar{M}$ is the average atomic mass, v_p is the phase velocity ($v_p = v_g$ in the Debye approximation), and γ is the Grüneisen parameter (a measure of the anharmonicity in a crystal lattice). In an insulator, phonon-phonon scattering does not occur in a perfect crystal unless there is anharmonicity. In contrast, materials with high Grüneisen parameter such as PbTe, Cu_3SbSe_3, and SnSe have been reported to have low lattice contribution to the total thermal conductivity.[54–56] Finding materials with high Grüneisen parameter is also utilized in high-throughput material search.[57] Details of Umklapp scattering can be found in solid state physics textbooks.[58–60]

The following expression is for the relaxation time limited by point defect scattering:

$$\tau_{PD}^{-1} = \frac{V\omega^4}{4\pi v_p^2 v_g} \left(\sum_j f_j \left(1 - \frac{m_j}{\bar{m}}\right)^2 + \sum_j f_j \left(1 - \frac{r_j}{\bar{r}}\right)^2 \right), \tag{1.31}$$

where f_j is the fraction of atoms with mass m_j (radius r_j) and $\bar{m}$ ($\bar{r}$) is the average mass (radius) of the atoms on their sites.[53] Doping or alloying can lead to enhancement of point defect (alloy) scattering when the mass and/or size contrasts are large. This scattering is more prominent for higher frequency phonons and at lower temperatures, below where Umklapp scattering becomes dominant.

Here we introduce two examples: $Yb_{1-x}Ca_xMg_2Bi_2$ and $Ca_5Al_{2-x}In_xSb_6$. The alloy scattering model for lattice thermal conductivity was developed by Callaway *et al.* [61]. In the model, input values, average speed of sound (v_s) and Debye temperature (Θ_D), to predict the effect of point defect scattering are either experimentally or theoretically determined. Combined with experimentally observed lattice thermal conductivity of end members, κ_L of alloyed samples can be quantitatively calculated. Callaway *et al.* proposed the following relation between the lattice thermal conductivity of alloyed samples ($\kappa_{L,alloy}$) and that of the pure end members ($\kappa_{L,pure}$) when Umklapp and point-defect scattering are dominant.

$$\frac{\kappa_{L,alloy}}{\kappa_{L,pure}} = \frac{arctan(u)}{u} \tag{1.32}$$

$$u^2 = \frac{\pi\Theta_D\Omega}{2\hbar v_s^2}\kappa_{L,pure}\Gamma, \tag{1.33}$$

where Ω is the volume per atom and Γ is the scattering parameter. Γ normally has two components: one is the contribution from mass fluctuation (Γ_M) and the other is from strain fluctuation (Γ_S). However, in the case of $Yb_{1-x}Ca_xMg_2Bi_2$, the strain fluctuation is negligibly small due to the similar ionic radii of Ca and Yb. Using the modified Klemens model proposed in ref. [62], Γ_M can be calculated with the following equations:

$$\Gamma_M = \frac{\sum_{i=1}^{n} c_i \left(\frac{\bar{M}_i}{\bar{\bar{M}}}\right)^2 f_i^1 f_i^2 \left(\frac{M_i^1 - M_i^2}{\bar{M}_i}\right)^2}{\left(\sum_{i=1}^{n} c_i\right)}, \tag{1.34}$$

where

$$\bar{\bar{M}} = \frac{\sum_{i=1}^{n} c_i \bar{M}_i}{\sum_{i=1}^{n} c_i} \quad \text{and} \quad \bar{M}_i = \sum_k f_i^k M_i^k. \tag{1.35}$$

Eq.1.34 is the case when two different atoms with atomic masses of M_i^1 and M_i^2 are on each of the i^{th} sublattices (k = 1, 2), c_i are the relative degeneracies of the respective sites, and f_i^k is a fractional occupation. Note that n = 3, c_1 = 1, $c_2 = c_3$ = 2, k = [Yb, Ca, Mg, Bi], $f_1^{Yb} = 1 - x$ and $f_i^{Ca} = x$ for $Yb_{1-x}Ca_xMg_2Bi_2$, in which case Eq. 1.34 and 1.35 become

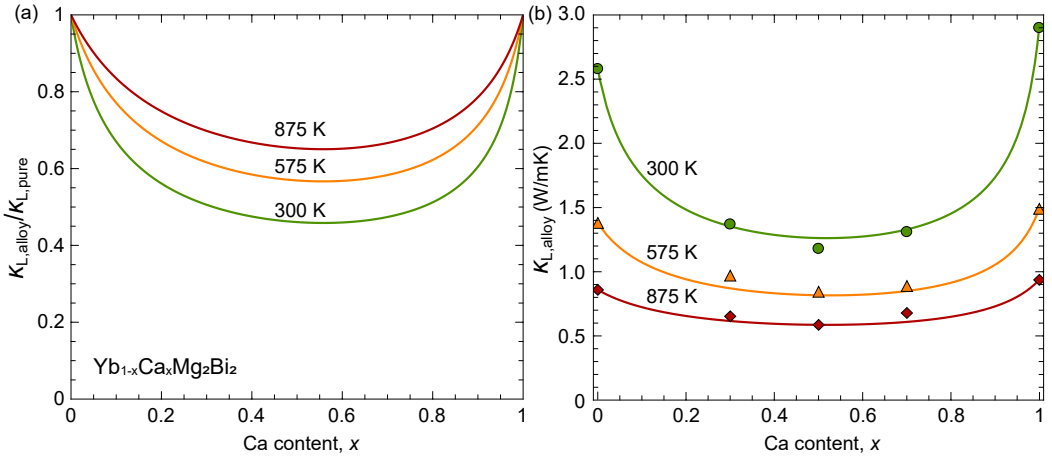

Figure 1.6: The effect of alloying on the lattice thermal conductivity of $Yb_{1-x}Ca_xMg_2Bi_2$. The x-axis is the Ca content and the y-axis is (a) the ratio between lattice thermal conductivity with and without alloy scattering and (b) the lattice thermal conductivity. The alloying effect is more prominent at low temperature because Umklapp scattering becomes more dominant at higher temperature. The solid curves in (b) are the lattice thermal conductivities predicted by the alloy scattering model at each temperatures and symbols are the experimental data from ref. [63].

$$\bar{\bar{M}} = \frac{1}{5}\left[M_1^{Yb} \times (1-x) + M_1^{Ca} \times x + M_2^{Mg} \times 2 + M_3^{Bi} \times 2\right] \tag{1.36}$$

and

$$\begin{aligned}\Gamma_M &= \frac{1}{5}\left[c_1\left(\frac{\bar{M}_1}{\bar{\bar{M}}}\right)^2 f_1^1 f_1^2\left(\frac{M_1^{Yb} - M_1^{Ca}}{\bar{M}_1}\right)^2 + 0 + 0\right] \\ &= \frac{1}{5}\left[\left(\frac{M^{Yb} - M^{Ca}}{\bar{\bar{M}}}\right)^2 x(1-x)\right].\end{aligned} \tag{1.37}$$

Once Γ_M is set, the ratio of $\kappa_{L,alloy}$ and $\kappa_{L,pure}$ can be calculated as a function of x *via* u. The effect that alloying has on κ_L of $Yb_{1-x}Ca_xMg_2Bi_2$ is shown in Fig.1.6. Fig.1.6(a) shows the amount of reduction in lattice contribution to thermal conductivity due to alloy scattering. Fig. 1.6(b) shows the comparison of the calculated values (solid curves) and the experimentally determined κ_L of samples with x = 0, 0.3, 0.5, 0.7, and 1. The values used in the calculation (v_s = 1616 m/s and Θ_D = 222 K) and experimentally determined κ_L in Fig. 1.6(b) were obtained

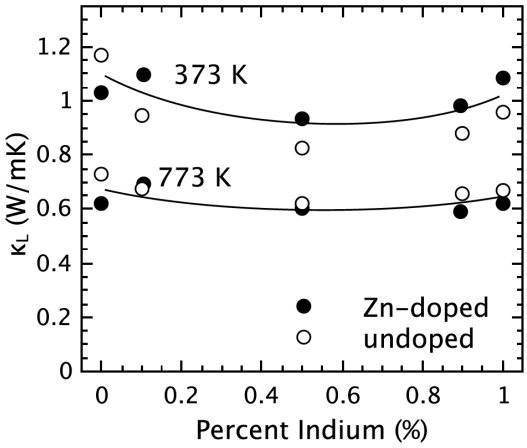

Figure 1.7: The effect of alloying on the lattice thermal conductivity of $Ca_5Al_{2-x}In_xSb_6$. The x-axis is In concentration with respect to Al and the y-axis is lattice thermal conductivity. This figure is reproduced with permission of the publisher.[29]

based on the reported data in ref. [63]. As can be seen in Fig. 1.6(a), the effect of alloy scattering becomes less prominent at higher temperature since the effect of Umklapp scattering becomes stronger. The effect of alloy scattering becomes larger with increasing mass difference and disorder, though it should be noted that point defects also increase the scattering rate of carrier mobility simultaneously.[44, 62, 64]

Another example of alloy scattering is $Ca_5Al_{2-x}In_xSb_6$, where the model proposed by Klemens was applied to consider both mass and strain fluctuations.[65] This model has been successfully applied to $Si_{1-x}Ge_x$ and $Ga_{1-x}In_xAs$, among others, to describe the large reduction in lattice thermal conductivity.[66, 67] Fig. 1.7 shows the results of modeling, which is reported in ref. [29].

The expression for the relaxation time limited by boundary scattering is

$$\tau_B^{-1} = \frac{v_g}{d}, \tag{1.38}$$

which is the most common approach for grain boundary scattering. Here, the mean free path is treated as independent of frequency (gray model), and simply equal to the average grain size d.[68] The effect of boundary scattering can be prominent by nanostructuring or reducing grain sizes, especially for low-frequency phonons, and has been demonstrated in nano-crystalline Si, $Si_{1-x}Ge_x$, and yttria stabilized zirconia.[69–71]

The following expressions are for the relaxation times limited by dislocations in a grain boundary. These can be treated as scattering by dislocation cores and strains with the following expressions:[72, 73]

$$\tau_{DC}^{-1} = \left(\frac{2}{sd}\right)\frac{V^{4/3}}{v_g}\omega^3 \tag{1.39}$$

$$\tau_{DS}^{-1} = 0.6 \times B_{D,eff}^2\left(\frac{2}{sd}\right)(\gamma+\gamma_1)^2\omega\left[\frac{1}{2}+\frac{1}{24}\left(\frac{1-2r}{1-r}\right)^2\times\left(1+\sqrt{2}\left(\frac{v_L}{v_T}\right)^2\right)^2\right], \tag{1.40}$$

where $B_{D,eff}$ and γ_1 are the magnitude of effective Burgers vector and the change in Grüneisen parameter. In Klemens's model [74], the dislocation density (N_D) was used instead of $2/(sd)$ (s is the average spacing between dislocation cores). These two scatterings mechanisms (τ_{DC} and τ_{DS}) could be replaced with τ_B with reasonable values of $B_{D,eff}$ and N_D when the average grain size is an observed parameter (grain boundary dislocation strain model).[73] It has been demonstrated that dislocation scattering can effectively increase the scattering rate of remaining mid-frequency phonons. For example, intentionally introducing vacancies followed by annihilation can enhance the dislocation scattering and results in reduction of lattice thermal conductivity of PdSe.[75] The advantage to utilizing dislocation scattering has also been demonstrated with PbTe by varying the concentration of Na in $Pb_{0.97}Eu_{0.03}Te$.[76]

Up to here, many scattering mechanisms to reduce τ_i^{-1} have been discussed, but lattice thermal conductivity can also be reduced by decreasing the contribution from $v_g(\omega)^2$ (see in Eq. 1.28). Introducing large and complex unit cell structures is one way of reducing $v_g(\omega)^2$. This inherent effect is one of the main reasons thermoelectric Zintl compounds have emerged as a promising class of thermoelectrics, as will be discussed in section 1.4, with details of $v_g(\omega)^2$ reduction in section 1.4.

3) Optimize η to obtain the best possible zT

Even if one obtains a material with high B, that material cannot be practically used unless the Fermi-level (or reduced chemical potential) is optimized by tuning the carrier concentration. Doping is the most common way to change the carrier concentration. In PbTe, substituting Pb with elements having a fewer number of valence electrons, such as Na, is one way to make p-type PbTe by creating holes.

Similarly, replacing Te with I can add an electron to the structure which makes it *n*-type. Doping can also be used to reduce the number of carriers; a thermoelectric Zintl compound, $Ca_9Zn_{4.3}Sb_9$, has an excess number of holes compared to the optimum. Replacing Ca atoms with La, which has one more valence electron, can provide an additional electron per La atom. This compensates a hole, leading to a reduction of the total number of majority carriers.

Defect engineering is another way of tuning the majority carrier concentration. For example, it has been reported that the defect chemistry of AZn_2Sb_2 (A = Yb, Eu, Ca, and Sr) Zintl compounds (see the structure in Fig. 1.9) can be modified by replacing the cation site atom.[77] It has been experimentally shown that AZn_2Sb_2 compounds are degenerate *p*-type semiconductors. Defect formation energy calculations elucidated that the most stable defects are cation vacancies, whose formation energies become higher with increasing electropositivity of the cation site atom. This increase in formation energy leads to fewer defects being formed, resulting in lower carrier concentration.[77] The trend in carrier concentration as a function of electronegativity of the cation site atom has been experimentally demonstrated not only in the AZn_2Sb_2 system but also in a multitude of thermoelectric Zintl compounds.[32, 78–81] Defect engineering can also be achieved by controlling the atomic chemical potential of a matrix phase by equilibrating it with different secondary phases. This defect engineering through atomic chemical potential can be experimentally performed with a concept we call "phase boundary mapping", which will be discussed in the Chapter 2.

1.4 Zintl Compounds

Zintl-Klemm-Busmann formalism

In this section, starting from a history of Zintl phases, an implementation of simple electron counting to understand the structure and bonding, along with the definition of "Zintl compounds" are discussed.

A German chemist, Eduard Zintl, conducted the first systematic studies on the compounds consisting of alkali and alkaline earth metals with the electronegative metals and semimetals of Groups 13 to 15 [3].[82–84] Zintl prepared numerous intermetallic compounds to investigate their structures and bondings in the early

[3]Note that the notation of groups of chemical elements can be different in the literatures. Group 13 and 15 become Groups IIIB and VB in the old IUPAC, International Union of Pure and Applied Chemistry, which was mainly used in Europe, and Groups IIIA and VA in CAS, Chemical Abstract Service, used in US.

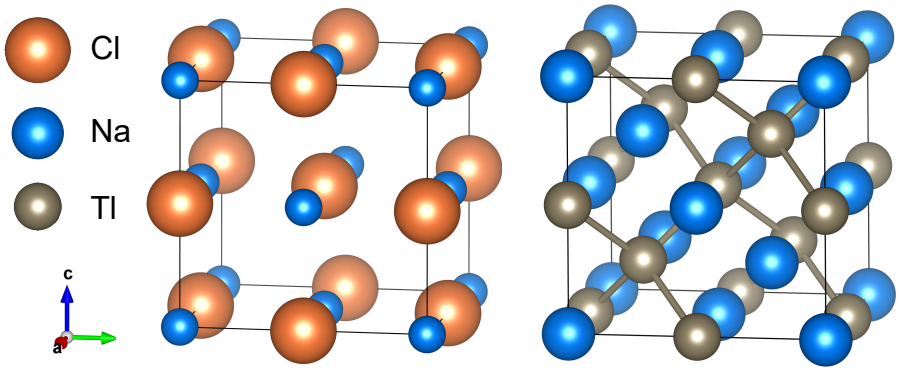

Figure 1.8: Crystal structure of NaCl and NaTl. NaTl is a classic example of a Zintl phase. Na atoms provide their electrons, which are, in turn, acquired by Tl atoms to form covalent bonds to satisfy valence.[87]

20th century, and these compounds were listed by F. Laves and referred to as "Zintl phases".[85] Chemically, these Zintl phases are classified somewhere between metals and insulators (the explicit definition is not easily determined), and their salt-like characteristics result in high melting point, brittleness, and poor electrical conductivity compared to other intermetallic compounds.[86] In Zintl phases, while the electropositive cations filling the spaces in between sublattices donate their electrons, a covalently bonded anionic skeleton forms the framework of the crystal structure to satisfy the valence requirement. A comparison of NaTl (Zintl phase) and NaCl (ionic compound) is one of the classic examples to illustrate how the electron transfer from cations to the anionic sublattice occurs in Zintl phases (see Fig. 1.8).[84] In NaCl, a Na atom donates one electron to Cl to be Na^+, while Cl becomes Cl^- to satisfy the octet rule. On the other hand, in NaTl, a Tl atom does not become 1- by itself, rather Tl atoms form covalently bonded "Zintl anions" to satisfy an electronic octet. With electrons transfered from more electropositive cations, Na in this case, Tl forms 4 covalent bonds, like group 14 elements. Klemm and Busmann generalized this valence counting interpretation of Zintl phases, and it is now called Zintl-Klemm-Busmann concept.[85]

Implementing the simple valence electron counting concept is useful to understand the structure and stoichiometry of a material. Assuming there is no bond between cations and all the bonds between anions contains two electrons, the valence electron count (VEC) per formula unit of the binary Zintl phase A_aX_x (A: electropositive cation, X: electronegative anion) is given by Eq. 1.41.

$$VEC = \frac{a \cdot e(A) + x \cdot e(X)}{x}, \tag{1.41}$$

where e(A) and e(X) are the number of valence electrons of element A and X, respectively. The 8 - N rule, a classical valence rule for insulator, is used to predict the number of covalent bonds to satisfy the octet rule. In the NaTl example, $VEC = 4$ so each Tl atom has $8-VEC = 4$ covalent bonds. Similarly, $VEC = (1\cdot2+2\cdot4)/2 = 5$ in $CaSi_2$, and thus $8 - VEC = 3$ results in a coordination number of 3 for the anion partial structure.[88] The Zintl-Klemm-Busmann concept can be utilized not only for binary materials to understand their structures and stoichiometry, but also for complex ternaries. An example of a ternary Zintl phase is $YbZn_2Sb_2$ (AM_2Pn_2, where A, M, and Pn are a cation (Yb), metal, or transition metal (Zn), and pnictogen (Sb), respectively). The electropositive atom Yb provides 2 electrons to be Yb^{2+}, and then atoms with similar electronegativity (Zn and Sb) form covalently bonded substructure to be $[Zn_2Sb_2]^{2-}$, resulting in the layered structure as shown in Fig. 1.9. Here, $[Zn_2Sb_2]^{2-}$ anionic frame becomes isoelectronic with ZnS and forms a wurtzite-like structure, absorbing electrons from intercalated Yb^{2+} sheets.

By definition, the classic Zintl phases are valence precise semiconductors with the net count of the valence electrons being zero (Zintl-Klemm-Busmann concept). However, in practice, there are Zintl phases reported to be degenerate semiconductors due to imperfections (formation of vacancies, interstitials, *etc*) and such valence imbalance can also be explained by simple electron counting. Therefore, compounds possessing a structure well explained by the Zintl-Klemm-Busmann concept but exhibiting degenerate semiconducting (metallic) behavior are referred to as "Zintl compounds".[89] Zintl compounds often have carrier concentration of 10^{19} to 10^{21} cm^{-3} which is essential for good thermoelectric materials as mentioned in previous sections.

Thermoelectric Zintl compounds

Zintl compounds have emerged as a new class of thermoelectrics. Some of the heavily investigated thermoelectric Zintl compounds, especially in a past few decades, are Skutterudite (*e.g.*$CoSb_3$),[45, 90] Mg_2Si,[91, 92] Zn_4Sb_3,[93, 94] La_3Te_4,[33, 95, 96] and Clathrates (*e.g.* $Ba_8Ga_{16}Sn_{30}$).[97–99] These compounds, each with their own histories, have narrow band gap, tenable carrier concentration, and low lattice thermal conductivity. $Yb_{14}MnSb_{11}$, which is a member of the so-called 14-1-11

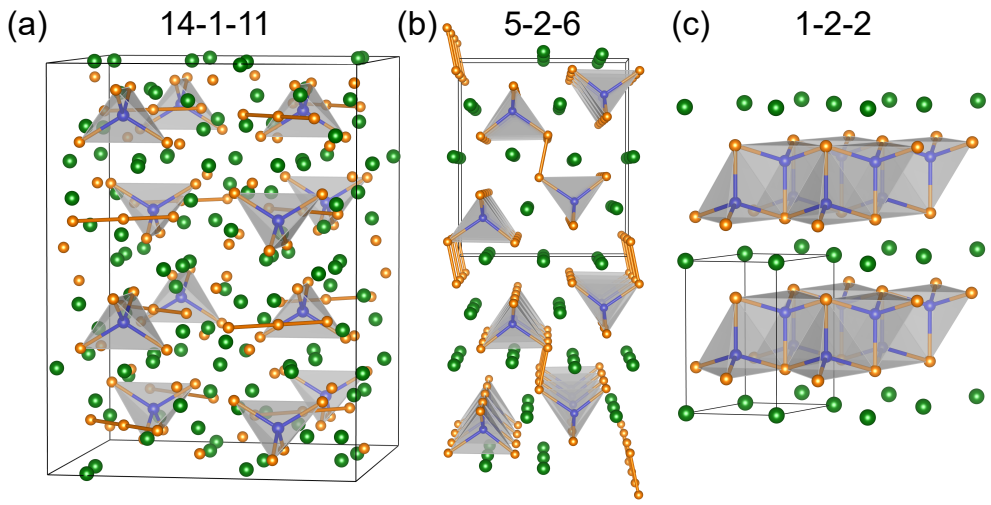

Figure 1.9: Example crystal structures of thermoelectric Zintl compounds consisting of cations (*A*, green spheres) filled in a covalently bonded anionic structure (blue (*M*) and orange (*Pn*) spheres). Tetrahedra are shown with gray. (a) 14-1-11: $Ca_{14}AlSb_{11}$ structure type ($I4_1/acd$) with isolated tetrahedra and Sb linear unit (0D anionic structure). (b) 5-2-6: $Ca_5Ga_2As_6$ structure type (Pbam) with ladder-like corner-sharing chains of MPn_4 tetrahedra (1D anionic stricture). (c) 1-2-2: La_2O_3 structure type (P-3m1) with a layered edge shared tetrahedra (2D anionic structure).

Zintl compounds, with $Ca_{14}AlSb_{11}$ structure type as shown in Fig.1.9,[4] is a relatively new thermoelectric material whose thermoelectric properties were first reported by Shawna *et al*. in 2006.[103] This material succeeded in overcoming the state-of-the-art of the time, SiGe, at high temperature (> 900 K) and is currently considered as a promising candidate for segmented devices for space application.[104–107] Following the success in 14-1-11, numerous Zintl compounds, especially complex pnictides, have been proven to have high zT such as 9-4-9,[30–32, 108], 5-2-6,[29, 109, 110] 1-2-2,[**Zhang2008**, 80, 81, 111–114], and 3-1-3,[28, 101] just name a few.

Of the thousands of Zintl phases whose thermoelectric properties have not been investigated, one strategy to search for compounds is to sort them by dimensionality

[4]Complex pnictide thermoelectric Zintl compounds are often referred to by their stoichiometry, but one should remember that complex Zintl phases with the same stoichiometry do not always form the same structure. This is one of the characteristics of Zintl compounds that attracts people's attention from a chemistry point of view. Their structures sometimes become completely different despite the same stoichiometry when their elements are substituted by atoms with the same valency but slightly different size. For example, the structure of Sr_3GaSb_3 is different from Sr_3AlSb_3, resulting in completely different transport properties.[100, 101] Semiconducting $Ca_5Al_2Sb_6$ with the structure shown in Fig.1.9 becomes a metallic compound forming a different structure ($Yb_5Al_2Sb_6$ structure type) simply by replacing Ca with Yb.[102]

of their anionic structure. Fig. 1.9 shows some example structures of thermoelectric Zintl compounds. The formula unit of $Ca_{14}AlSb_{11}$ structure type consists of 14 A^{2+} cations, 4 Pn^{3-} anions, $[MPn_4]^{9-}$ tetrahedron, and Pn_3^{7-} linear units. These sublattices are all isolated and can be considered as a 0D anionic structure. In addition to 14-1-11, compounds with $CaAl_2Si_2$ structure type have also been heavily investigated as thermoelectrics. As mentioned in section 1.4, 1-2-2 compounds possess layered (2D) anionic frame of $[Zn_2Sb_2]^{2-}$. Thermoelectric properties of 5-2-6 and 3-1-3 Zintl compounds have been investigated following the success in 0D (14-1-11) and 2D (1-2-2) thermoelectric Zintl compounds to examine the properties of 1D anionic structure. The $Ca_5Ga_2Sb_6$ structure type consists of extended 1D chains of corner shared MPn_4 tetrahedra. All 5-2-6 and 3-1-3 compounds have a 1D chain-like structure, though some have edge or face shared tetrahedra. Details are discussed in several reviews.[86, 89, 115, 116] The 9-4-9 type Zintl compounds have a unique structure. It consists of ribbon-like tetrahedra connected in one direction to form 1D infinite ladder-like sublattices which are bridged by the partially occupied interstitial transition metals sites to form a 2D structure.[117, 118] Therefore, the dimensionality of its anionic structure is somewhere between 1 and 2 depending on the partial occupancies.(See Chapter 5 and 6)

There are two key characteristics that make research of thermoelectric Zintl compounds fascinating: a) their rich chemistry and b) their inherently low thermal conductivity.

a) Rich chemistry of Zintl compounds

Since the same system can accommodate a variety of elements, Zintl compounds can be great "model cases" to examine the effect of chemical change to the thermoelectric properties. For example, Mg, Ca, Sr, Yb and Eu are candidates for a cation site atom of AM_2Pn_2, M can be Mn, Mg, Zn, or Cd.[63, 78, 79, 113, 119–127] In addition, Sb is not the only element for Pn but also As, Bi and P analogues exist.[81, 128–130] Similarly, $A_{14}MPn_{11}$ (A = Ca, Sr, Ba, Yb, Eu; M = Mn, Zn, Mg, Al; Pn = P, As, Sb, Bi),[105, 107, 131–137] $A_5M_2Pn_6$ (A = Ca, Eu, Sr, Yb, Ba; M = Al, Ga, In, Pn = Sb, Bi, As),[102, 108, 110, 138–142] and $A_9M_{4+x}Pn_9$ (A = Ca, Sr, Eu, Yb; M = Zn, Mn, Cd; Pb = Sb, Bi) also have a large variety of choices for the elements contained in the same system.[30–32, 117, 118, 143–145] In the AM_2Pn_2 system, the carrier concentration can increase when the A cation atom is replaced with a more electronegative atom. This trend can be explained by calculating the most stable defect formation energies.[77] Using metals or transition metals with spin,

such as Mn, can reduce the carrier mobility due to spin disorder scattering.[146] In Sb analogues of 9-4-9 and 1-2-2, using Zn as the transition metal leads to higher mobility since the effective mass becomes smaller.[31, 80, 122] In addition, some of the listed candidate atoms can be introduced at the same time to form solid solutions, which can reduce the lattice thermal conductivity, due to alloy scattering, and possibly change the carrier concentration by changing defect chemistry. These general trends shown experimentally in thermoelectric Zintl compounds can be chemically explained. Some reviews summarizes those chemical explanations.[86, 147]

As explained in Section 1.2, the maximized thermoelectric performance for one material can be obtained only when the carrier density of the material is optimized. Although some of thermoelectric Zintl compounds can naturally have the correct amount of defects to obtain desirable degenerate semiconducting behavior without tuning, in almost all the cases fine tuning of the carrier concentration is required. One effective way to finely increase or decrease the carrier concentration in various materials is doping, and Zintl phases often can accommodate several different types of dopant. For example, replacing a small fraction of Yb^{2+} by La^{3+} or Mn^{2+} by Al^{3+} in $Yb_{14}MnSb_{11}$ can reduce the majority hole concentration,[104, 105] and substituting some Ca^{2+} with Na^{1+} or Al^{3+} with Zn^{2+} in $Ca_5Al_2Sb_6$ can increase the carrier concentration.[109, 148]

b) Merit of complex structure

The other key for thermoelectric Zintl compounds is their inherently low lattice thermal conductivity, which arises from the complex unit cell structure of Zintl compounds. When the crystal structure becomes more complex, the lattice thermal conductivity (κ_L) becomes lower. From a chemistry point of view, the rigid covalently bonded anionic structure allows the electron or hole to conduct well, while loosely bound atoms filled in between anionic frames contribute to reduction of the lattice thermal conductivity. In addition, simply having a larger unit cell size or larger number of atoms in a unit cell can reduce the lattice thermal conductivity. For example, κ_L of $Yb_{14}MgSb_{11}$, $Yb_{14}MnSb_{11}$, and $Ca_{14}MnSb_{11}$ are around 0.5 - 0.6 W/mK at room temperature, κ_L of $Ca_5Al_2Sb_6$ and Sr_3GaSb_3 whose κ_L are around 1.2 W/mK, and κ_L of 1-2-2 compounds such as $CaZn_2Sb_2$ and $YbZn_2Sb_2$ are around of 2 W/mK.[79, 80, 101, 103, 104, 106, 107, 128, 149] Here, the order of the structural complexities are 14-1-11 (N = 208 where N is a number of atoms in one unit cell) > 5-2-6 and 3-1-3 (N = 26 and N = 28, respectively) > 1-2-2 (N

= 5). Since this general trend in κ_L can be explained qualitatively with a simple atomic chain, the origin of inherently low lattice thermal conductivity of complex materials is discussed in the following section.

Complex structure and low thermal conductivity

Consider a mono-atomic 1D chain with atomic weight m, elastic constant K, and atom spacing a. Assuming the interactions only between the nearest neighbor atoms and Born-von Karman boundary condition, the phonon dispersion relationship becomes a monotonically increasing single curve as a function of absolute value of wave numbers ($0 \leq |k| \leq \frac{\pi}{a}$). The lattice spacing of a is equivalent to the unit cell size in the real material. When the unit size of the monoatomic chain set to $2a$, the dispersion relation gets "folded", replacing one atom with two atoms of differing atomic mass (M), producing a gap between lower frequency (acoustic phonons) and higher frequency (optical phonons). The same effect occurs when different spring constants (G) are introduced.

Here, let's recall the expression of κ_L in Eq.1.28. The lattice thermal conductivity can be obtained by integrating the spectral lattice thermal conductivity, the product of $C_s(\omega)$, $v_g(\omega)$, and $\tau(\omega)$, over ω. At high temperature in Debye approximation ($T > \Theta_D$ where Θ_D is a Debye temperature), the Dulong-Petit law can be applied and the spectral heat capacity $C_{s,HT}(\omega)$ becomes

$$C_{s,HT}(\omega) = \frac{3k_B\omega^2}{2\pi^2 v_p^2 v_g}, \tag{1.42}$$

where v_p and v_g are the phase velocity and group velocity defined as

$$v_p = \frac{\omega}{k} \tag{1.43}$$

$$.v_g = \frac{d\omega}{dk}. \tag{1.44}$$

At T sufficiently higher than Θ_D, the dominant phonon scattering mechanism is most likely Umklapp scattering. Since the product of $C_s(\omega) \cdot \tau_U(\omega)$ (refer to Eq.1.30) is independent of ω, κ_L is solely dependent on the integration of $v_g(\omega)^2$ with respect to the frequency, as seen in Eq.1.28. In Eq. 1.44, $v_g(\omega)$ is the slope of the phonon dispersion relationship. By increasing the difference between K and G or M and m, the gap between the branch becomes larger and both branches flattens, and thus the integrated value of $v_g(\omega)^2$ becomes lower. Increasing unit cell size

by introducing even more atoms having different atomic masses or bondings with different spring constants leads to reducing the integration of $v_g(\omega)^2$ over ω. This is due to the folding and introducing of more gaps, and ultimately results in reduction of the lattice thermal conductivity.[53] Thus, the complex thermoelectric Zintl compounds, which have large unit cell structures consisting of various atoms and bondings (analogous to the substructure approach), can have inherently low lattice thermal conductivity.

One way of examining κ_L with the maximum scattering rate is to utilize Cahill's glassy (amorphous) limit model.[150] In 1907, Einstein constructed a model for atomic vibration of harmonic oscillators vibrating with the same frequency.[151] Although Einstein's model is known to fail at capturing the temperature dependency and magnitude of thermal conductivity of crystalline lattices, his model can be applied to highly disordered crystals such as amorphous solid as shown in ref. [152]. Assuming the shortest mean free path (maximum scattering rate) for all phonons as $l = \frac{\lambda}{2}$ (l is the mean free path and λ is the phonon wave length), the expression for glassy limit lattice thermal conductivity (κ_{glass}) becomes

$$\kappa_{glass} = \left(\frac{\pi}{6}\right)^{1/3} \frac{k_B}{V^{2/3}} \sum_i v_i \left(\frac{T}{\Theta_i}\right)^2 \int_0^{\frac{\Theta_i}{T}} \frac{x^2 e^x}{(e^x - 1)^2} dx, \tag{1.45}$$

where $\Theta_i = v_i(\hbar/k_B)(6\pi^2 n)^{1/3}$ (n is the number of density of atoms). At the high temperature limit ($\kappa_{glass,HT}$),

$$\kappa_{glass,HT} = \frac{1}{2}\left(\frac{\pi}{6}\right)^{1/3} k_B V^{-2/3}(2v_t + v_l), \tag{1.46}$$

where V is volume per atom. In the equations above, v_t and v_l are the transverse and longitudinal speeds of sound, which can experimentally be obtained using ultrasonic measurement.[5] The values of κ_{glass} in complex Zintl compounds are shown in various reports.[30–32, 100, 102, 138]

[5]Sometimes the value obtained from Cahill's model with experimentally determined speeds of sound is treated as the theoretical minimum lattice thermal conductivity but there are materials whose κ_L are lower than κ_{glass}.[18, 153–155] Deviation from the Debye approximation, temperature dependency of speed of sounds, or overestimation of Debye temperature can lead to overestimating the minimum thermal conductivity. Interested readers can refer to [156] for example.

1.5 Summary of research

This thesis primarily focuses on establishing the experimental concept we call "phase boundary mapping" and its implementation to utilize multi-phase equilibria for defect engineering through controlling atomic chemical potential of the target phase. It has been shown from growing binary semiconductors such as GaAs and GaN that the growth condition significantly affects the defect concentration of the resulting sample. However, it has not been utilized in bulk thermoelectric researches largely due to the lack of clear methodology and experimental demonstrations.

The prevalent concept of "line compounds" in solid state chemistry is that they are identical, if reasonably pure, since phase widths of these compounds are so narrow. Although the single-phase regions of line compounds are indeed fairly small, any compound has finite phase width due to point defects, which always exist because of the entropy. The total defect concentration in a material is determined by the formation energies of each defect, which can be controlled by changing the reference atomic chemical potentials of a system. Chemical potentials reflect the reservoirs for atoms that are involved in the defect formation. In other words, the coexisting phases in equilibrium uniquely determine the chemical potentials of the resulting sample at given temperature and pressure. Even though a nominal composition (an amount of starting materials) is exactly the same as the charge balanced composition of the target phase, in practice, a synthesized sample almost always contains a small amount of secondary phases.

Phase boundary mapping, whose details are discussed in Chapter 2, is an experimental concept to take advantage of accessible multi-phase equilibria, where the target matrix phase coexists with impurity phases. Thermodynamically, the degrees of freedom of a system in equilibrium can be determined by the number of components and phases at a given temperature and pressure, with multi-phase equilibria with no degrees of freedom tending to have significantly larger phase regions around the target line compound. By mapping out the boundaries of these wide multi-phase regions in nominal composition space, followed by systematic sample preparation with intentionally varied nominal compositions, the effect of the change in reference atomic chemical potentials can be properly correlated with the transport properties of resulting samples.

In Chapter 4, the mechanism of obtaining *n*-type conduction in Mg_3Sb_2-based compounds, which is a good demonstration of phase boundary mapping in a binary compound, is discussed. The investigation of the two distinctly different multi-phase

equilibria around a binary Zintl compound, Mg_3Sb_2, (Mg-excess and Sb-excess) with both computations and experiments elucidated the mechanism to obtain *n*-type conduction. Mg_3Sb_2 has a long history of research, but its *n*-type conduction has been found only recently to have exceptionally high zT. Originally, the large Mg-solubility in Mg_3Sb_2 as Mg interstitials was believed to be the source of its *n*-type conduction. However, our research concluded that the key for obtaining n-type conduction is suppressing the formation of "electron killers" (Mg-vacancies) by equilibration of Mg_3Sb_2 with elemental Mg.

Chapter 5 discusses the implementation of phase boundary mapping to optimize the carrier concentration of a complex Zintl thermoelectric $Ca_9Zn_{4+x}Sb_9$. Correlation between the phase regions of each sample and their transport properties revealed the step-wise change in carrier concentration as the phase region became more Zn-rich, which resulted in optimizing the carrier density of $Ca_9Zn_{4+x}Sb_9$. The zT of $Ca_9Zn_{4+x}Sb_9$ is one of the highest among the inexpensive thermoelectrics in the intermediate temperature range.

In Chapter 6, the thermoelectric properties of the new Zintl compound $Yb_9Zn_{4+y}Sb_9$ and the effect of alloying in $Yb_9Zn_{4.2-x}Mn_xSb_9$ are discussed. Substituting Mn with Zn reduced the effective mass leading to enhancement in the quality factor. However, the carrier density of $Yb_9Zn_{4+y}Sb_9$ was too high to be a good thermoelectric material. Although it was originally thought to be impossible to reduce the carrier concentration of $Yb_9Zn_{4+y}Sb_9$, applying the phase boundary mapping allowed realization of lower carrier density, leading to five times higher zT.

Chapter 2

Phase boundary mapping for defect engineering

2.1 Summary

Formation energies of point defects can be engineered through the control of atomic chemical potentials by purposely equilibrating the target phase with different sets of secondary phases. It can pave the way for, for example, suppressing the formation of killer defects enabling doping efficiency, and the optimizing charge carrier concentration without any extrinsic dopants. Such defect engineering can be experimentally achieved with a concept we call "phase boundary mapping" utilizing practically accessible different phase equilibria.

Binary semiconductors such as GaAs, GaN, ZnO, and ZnSe are often referred to as "line compounds" since their single-phase regions appear as a line on the binary phase diagram. However, in the real world, no crystal is perfect due to entropy and a certain amount of point defects always exists in a material at finite temperature.[157–161] These point defects always provide semiconductors a narrow but finite phase width and, in practice, one of the two edges of the "line" of single-phase region is experimentally accessible. Those edges correspond to the compositions of the target material in two different two-phase equilibria. Therefore, we can say that there are two distinctly different "thermodynamic states" in a binary semiconductor, which have discrete defect formation energies and, accordingly, different defect concentration and charge carrier concentration. Practically, the thermodynamic states of a sample can only be made sure when the secondary phase equilibrated with the target phase in a sample is detected. Thus, we purposely change the nominal composition (the amount of starting elements) until the secondary phase appears in XRD or SEM to map out the boundaries of phase regions in the nominal-composition space. This experimental concept is called "phase boundary mapping". Once the phase boundaries are mapped out with systematic sample characterization, the information of the thermodynamic states can be correlated to measured transport properties.

Single-phase regions of multinary semiconductors including ternaries and quaternaries also possess a small but finite phase width for the same reason. Normally, there are a multitude of different thermodynamic states around the single-phase

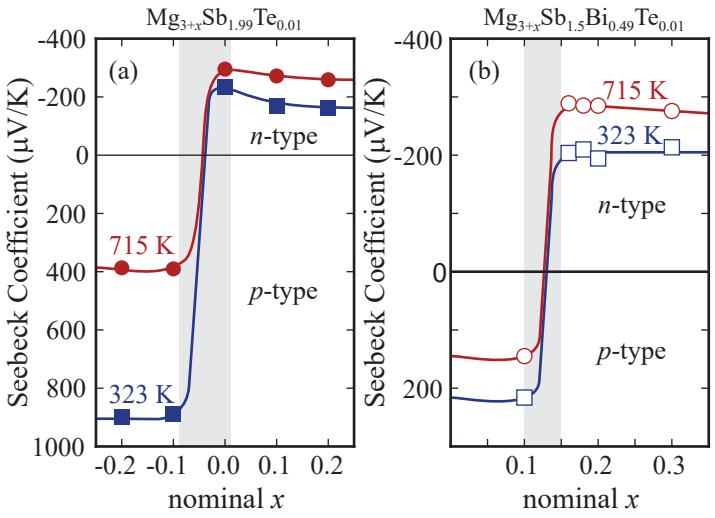

Figure 2.1: Seebeck coefficient of $Mg_{3+x}Sb_2$-based compounds as a function of nominal excess Mg content from its stoichiometric composition (x). The sign of Seebeck coefficient flips from positive to negative at a certain x where the location of phase boundary in nominal composition space. Slight difference in synthesis affects the location of the boundary (shaded region). Details of synthesis of two sets of samples are in Chapter 3.

region of a target phase which can be utilized for delicate tuning of the defect concentration in the multinary compounds. Precise carrier density optimization is particularly important for thermoelectrics to obtain the best possible efficiency from a material since all the properties are interdependent to each other via carrier concentration.

In the first part of this chapter, a few outcomes of applying phase boundary mapping to thermoelectric materials are introduced. Then, the knowledge of thermodynamics behind the phase boundary mapping is reviewed with some simple examples. In the following sections, starting from a simple example of a binary semiconductor, we'll also extend the discussion to cases of ternary compounds.

2.2 Major successes of phase boundary mapping

Two successful examples of implementing phase boundary mapping for thermoelectric materials are the cases of $Mg_{3+x}Sb_2$-based compounds and $Ca_9Zn_{4+x}Sb_9$, where x indicates the nominal composition (the amount of starting elements).

As shown in Fig. 2.1, our implementation of phase boundary mapping on $Mg_{3+x}Sb_2$-based compounds (systematic sample preparation with varying nominal Mg contents x) revealed a clear positive to negative transition of a sign in measured Seebeck

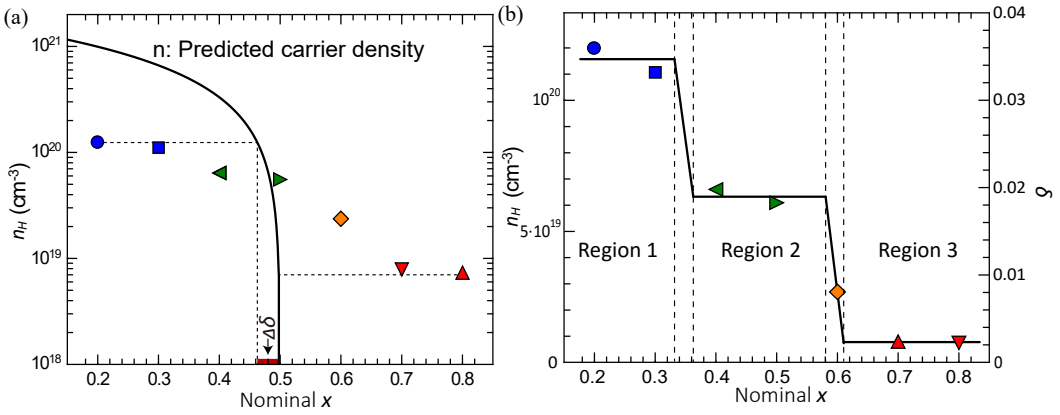

Figure 2.2: Carrier concentration of $Ca_9Zn_{4+x}Sb_9$ as a function of nominal Zn content x. The black solid curve in (a) is predicted carrier concentration based on the nominal composition, assuming that the entire hole carrier concentration arises from Zn deficiency. As the nominal composition becomes closer to the charge balanced composition ($x = 0.5$), the predicted carrier concentration becomes smaller and supposed to be n-type when $x \geq 0.5$. However, the experimental carrier concentration doesn't change as expected and shows step-wise reduction as shown in (b). The y-axis of (b) is indicating the actual composition of 9-4-9 phase ($Ca_9Zn_{4.5-\delta}Sb_9$) assuming Zn-deficiency is the only source of carriers. The gradual step-wise reduction can optimize the carrier concentration of $Ca_9Zn_{4.5-\delta}Sb_9$, resulting in zT = 1.1. Fig. (b) has been published in ref. [32] and been reproduced here with permission from a journal.

coefficient, indicating a transition from p-type to n-type thermoelectric. Such n-type $Mg_{3+x}Sb_2$-based compounds can achieve exceptionally high figure of merit (zT = 1.5) but they had not been discovered till late 2016 despite of the numerous past studies reporting their moderate p-type thermoelectric properties ($zT \leq 0.6$).[47, 82, 121, 162, 163] This is mainly because of the high volatility and reactivity of elemental Mg leading to the loss of Mg during the synthesis, which always results in samples with excess amount of Sb. Therefore, only by applying the phase boundary mapping could the Mg-excess $Mg_{3+x}Sb_2$-based compounds be attained and investigated.

Phase boundary mapping was also successfully applied to a complex thermoelectric Zintl compound, $Ca_9Zn_{4+x}Sb_9$ so called 9-4-9, enabling precise control on carrier concentration. $Ca_9Zn_{4+x}Sb_9$ structure becomes charge balanced when the composition is $Ca_9Zn_{4.5}Sb_9$ but it tends to be slightly Zn deficient.[144] This Zn deficiency creates holes to make this material degenerate p-type semiconductor. Assuming the change in carrier density solely caused by this Zn deficiency, the predicted amount

of created carriers can be calculated as the solid line in Fig. 2.2(a). However, it is clear that the trend in measured carrier concentrations doesn't follow the expected values. The $\Delta\delta$ in a Fig. 2.2(a) is the range of calculated composition of 9-4-9 phase based on measured Hall carrier concentration ($\Delta\delta$ = 0.034). Comparing this $\Delta\delta$ to the range of nominal Zn content (Δx = 0.6), change in the carrier concentration is significantly smaller but interestingly it still keeps decreasing gradually as more Zn added. This unexpected behavior can be understood by applying phase boundary mapping. Based on the secondary phases detected in samples, it has been confirmed that there are three regions containing 9-4-9 phase with different thermodynamic states in the nominal composition range we explored. Samples with almost the same carrier concentration (ones at the same plateau in Fig. 2.2 (b)) have the same set of secondary phases, and the step-wise change in carrier concentration occurs when the spices of secondary phases become different. This systematic reduction in carrier concentration as a result of utilizing different thermodynamic states leads to the exceptional thermoelectric performance of $Ca_9Zn_{4+x}Sb_9$.

2.3 Thermodynamic description of phase boundary mapping

Phase boundary mapping is a critical experimental concept to experimentally explore all the accessible thermodynamic states of a material; the basic knowledge of thermodynamics is sufficient to capture key physics: (I) atomic chemical potentials of coexisting phases become identical in equilibrium, (II) the degrees of freedom of the system of interest is determined by the Gibbs phase rule, and (III) defect formation energy at a given Fermi level is dependent on the atomic chemical potentials.

(I) Although the chemical potentials are often regarded as variables in simulations, there are some strict bounds due to impurities in a practical case. The chemical potential of an atom spices i for different phases coexisting in a system become identical in equilibrium. For example if there are P phases, the chemical potential of atom spices i becomes

$$\mu_i^{\alpha} = \mu_i^{\beta} = \cdots = \mu_i^{P}. \tag{2.1}$$

This is one of the equilibrium conditions. Details can be found in Appendix A.

(II) The largest number of thermodynamic parameters that can be varied simultaneously and arbitrarily without affecting one another is called the degrees of freedom, F. For a system in equilibrium, such F can be obtained from the number of compo-

nents (C) and the number of phases (P) by the following relation,[164, 165]

$$F = C - P + 2. \tag{2.2}$$

Our independent variables are temperature (T), pressure (p), and the fractions of the components in each phase. Thus, the total number of independent variables is $CP + 2$. However, there are two sets of constraints. One is that the sum of the mole fraction in each phase must be unity. This constraint can reduce the number of variables by P. Another one is that the chemical potential of each component must be the same in all phases (I). The number of equations for chemical potential is $P - 1$ for each components so the total number becomes $C(P - 1)$. Therefore, the number of degrees of freedom can be calculated by subtracting the number of constraints from the number of variables.

(III) The following expression is used to compute the defect formation energy of a defect X in charge state q.[157, 159, 166]:

$$E^f[X^q] = E_{\text{tot}}[X^q] - E_{\text{tot}}[\text{bulk}] - \sum_i n_i \mu_i + qE_F + E_{\text{corr}}, \tag{2.3}$$

where $E^f[X^q]$ is the total energy of a material containing the defect X in charge state q and $E_{\text{tot}}[\text{bulk}]$ is the total energy of a material in perfect crystal form. n_i denotes the number of atoms of type i that have been added to (positive n_i) or subtracted from (positive n_i) to form the defect X^q. E_F is the chemical potential for electrons or Fermi level and the latter term will be used hereafter. E_{corr} is a correction term for computation, which becomes zero in ideal case. As shown here, the defect formation energy is dependent on atomic chemical potentials and the Fermi level, and phase boundary mapping is a method to experimentally control μ_i. Defects with larger formation energies are less favorable, and if the defect formation energy becomes negative, that defect instantly forms even at 0 K.

2.4 Binary cases

Suppose there are two components, A and B, which can form only a binary compound (semiconductor) with a charge balanced composition of $A_{1-x_\beta}B_{x_\beta}$. Assuming the case where samples are under a constant pressure, the degrees of freedom of the single-phase region such as α become two (divariant system) since $F = C - P + 1$ where $C = 2$ and $P = 1$, meaning the composition and T can independently vary. Similarly, $F = 1$ can be obtained for two-phase regions (*eg.* $\alpha + \beta$) where

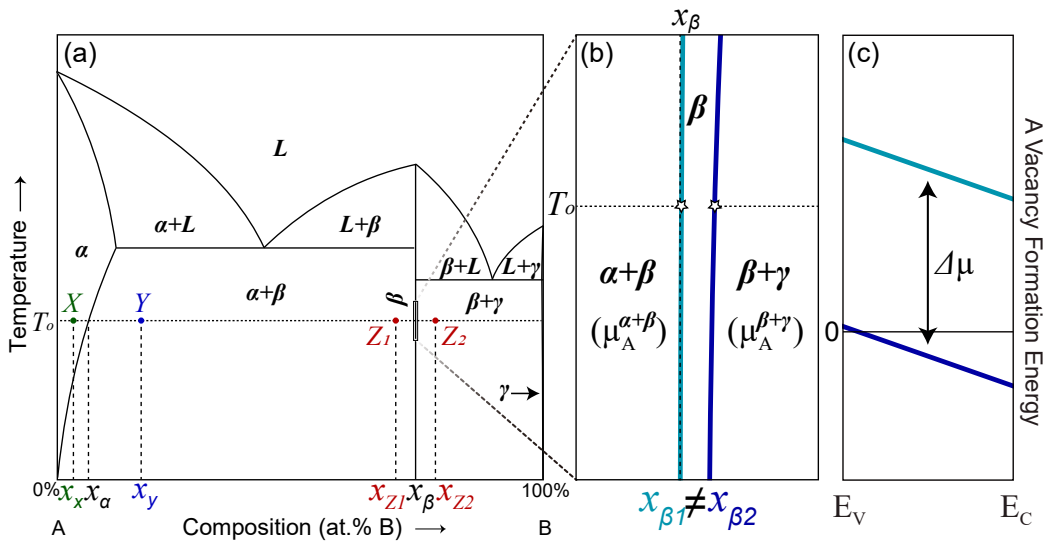

Figure 2.3: Schematic (a) A-B binary phase diagram, (b) magnified binary phase diagram around a single-phase region of the β phase, and (c) defect formation energy diagram of an A vacancy. Distinctly different thermodynamic states arise from the difference in atomic chemical potentials and result in discrete defect formation energies as shown in (c). The higher light-blue line corresponds to $E^f[V_A]$ of β phase in the A-excess region and the dark-blue line is $E^f[V_A]$ of the β phase in the B-excess region. Assuming A vacancy is the only stable vacancy to be considered, calculated B concentration of the β phase in two distinct thermodynamic states are in (b). Therefore, even though the binary line compounds are lines in the scale of (a), they indeed have finite phase widths as shown in (b).

the composition and temperature cannot be arbitrarily chosen independently. For example, the composition of the α phase in the two-phase region of $\alpha + \beta$ can only vary along the boundary between α single-phase region and $\alpha + \beta$ two-phase region as the temperature changes. Namely, when the temperature is determined the composition is also uniquely determined in such $F = 1$ regions in binary cases (univariant system).

Then, we suppose the case where samples are in equilibrium at a given pressure and also a given temperature ($T = T_o$). This case is more relevant for the practical bulk samples for thermoelectrics. Since the temperature is now a constant, the concentration of B component (x) is the only independent variable. Consider a sample X (point X in Fig. 2.3(a)) which is in the single-phase region of α. Since $F = C - P$, $C = 2$ and $P = 1$, the degree of freedom of this α phase is one (univariant system), meaning the composition of α phase can vary as long as x_x is in this single-phase region ($0 \leq x_x \leq x_\alpha$) at a given temperature T_o. On the other hand, samples

with nominal composition of x_y (point Y in Fig. 2.3(a): sample Y) and x_{z1} (sample Z_1) are in a two-phase region where $F = 0$ (invariant system). The phase fractions of α and β phases in samples Y and Z_1 are different (according to the lever rule), but the B concentration of α phase and β phase are fixed at x_α and x_β, respectively, no matter how the sample compositions are changed as long as $x_\alpha \leq x_y, x_{Z1} \leq x_\beta$.

The phase boundary mapping exploits the character of the phase regions with no degrees of freedom (invariant systems) at a given temperature. Here, we suppose β is our target phase for bulk transport characterization. In the case of a research on bulk materials, even if no impurities are observed in XRD, the synthesized bulk samples of line compounds almost always contain certain amount of secondary phase(s). Consider two samples, Z_1 and Z_2, with the "actual" nominal B concentration of x_{Z1} (in $\alpha + \beta$ region) and x_{Z2} (in $\beta + \gamma$ region) at $T = T_o$, respectively. Even when the weighed nominal B concentration (herein this is called the weighed-nominal composition) is exactly x_β (this is the target composition), the slight deviation in composition of elements which can involve the reaction (actual-nominal composition) from x_β can exist for many reasons[1]: impurities contained in raw elements such as surface oxidation, elements reacting with vials, dies and other instruments, evaporation or melting during pressing and annealing, just to list a few. The chemical potentials of an atom spices i (μ_i) for coexisting phases are identical in an invariant system (See I). In other words, the chemical potential of the target phase is determined by the coexisting phase, and thus μ_i can be set as $\mu_A^{\alpha+\beta}$ in $\alpha + \beta$ phase and $\mu_A^{\beta+\gamma}$ in $\beta + \gamma$ phase.

Now, for the sake of simplicity, we consider the case where only A vacancies, which create holes in the valence band, are the stable defects in the material. The formation energy of a defect can be obtained through Eq. 2.3 (See III). Setting the reference of chemical potential of A (μ_A) to elemental A (μ_A^o), the difference between the

[1] Two different types of nominal compositions, *weighed-nominal composition* and *actual-nominal composition*, are defined here to emphasize the systematic loss of starting elements. To make a sample with the target composition, the stoichiometric amount of starting elements are weighed and put into vials or ampules for synthesis. Herein we call the amount of starting element at this stage as the *weighed-nominal composition*. However, there is a systematic loss of starting elements due to the reasons listed above, and the ratio of each element can be varied from the weighed-nominal composition through the synthesis procedures. For example, in the case of $Ca_9Zn_{4+x}Sb_9$, elemental Ca tends to have larger surface oxidation which are too stable to involve the reaction than Zn and Sb, leading to smaller Ca content than weighed-nominal composition, and elemental Zn is likely to sublimate more than Ca and Sb, resulting in loss of Zn from weighed-nominal composition. Therefore, the overall composition of the raw ingredients contributing to the formation of the resulting sample can slightly deviate from the weighed-nominal composition, and to distinctly distinguish it from *weighed-nominal composition*, we herein call it *actual-nominal composition*

chemical potential of species A in sample Z_1 and Z_2 ($\Delta\mu$) can readily be calculated as $\Delta\mu = |\mu_A^{\beta+\gamma} - \mu_A^o|$ since $\mu_A^{\alpha+\beta} = \mu_A^o$. An upper bound on the chemical potential is set by the formation of elemental A, $\mu_A \leq \mu_A^o$, and therefore $\mu_A^{\beta+\gamma} < \mu_A^o$. Consequently, $E^f[V_A]$ of β phase in $\alpha+\beta$ two-phase region is distinctly higher than that of β phase in $\beta+\gamma$ two-phase region by $\Delta\mu$.

The single-phase region of β is just a line on the scale of Fig. 2.3(a), but it actually has a finite width as shown in Fig. 2.3(b) due to the formation of defects. Fig. 2.3(c) shows a schematic defect formation energy diagram describing $E^f[V_A]$ in two different two-phase regions discussed above (they can be refereed to as A-excess and B-excess β phase when the target phase is β). Based on the defect formation energies, the A vacancy concentration (n_{V_A}) can be calculated using

$$n_{V_A} = N_{site}^{V_A} \exp\left(\frac{-E^f[V_A]}{k_B T}\right), \tag{2.4}$$

where N_{site}^A is the site density of A. In the case of Fig. 2.3(c), while $x_{\beta 1}$ is still closer to the charge balanced composition x_β when $\Delta\mu$ is sufficiently large, $x_{\beta 2}$ is noticeably greater than x_β. As a result, the magnified phase diagram around the single-phase region of β becomes as shown in Fig. 2.3(b). As mentioned before, in practice, the sample composition tends to be at one of the two sides of boundaries. Therefore, the properties of the β phase in distinctly different thermodynamic states become substantially different: one is almost an intrinsic semiconductor with low a carrier concentration (A-excess β), but the other becomes a degenerate semiconductor (B-excess β).

2.5 Overcoming killer defects

The amount of impurities that contribute to the increase in the charge carrier density is limited by the increasingly probable formation of compensating defects of the so called "killer defects". In the case of the β phase discussed above, A vacancy is a killer defect for electron donors. Consider the situation of doping B-excess β phase with an extrinsic dopant assuming no interaction between defects. B-excess β phase is a degenerate p-type semiconductor due to the formation of stable A vacancies, thus the Fermi level (E_F) will be in the valence band, $E_F < E_V$, without any doping at finite temperature. The negative slope of $E^f[V_A]$ in Fig. 2.3(c) indicates that the charge state of defect V_A is negative, meaning V_A is an acceptor. As the amount of extrinsic dopant increases, since the Fermi level is pushed toward the conduction band, A vacancy becomes progressively favorable and, once $E^f[V_A]$ becomes negative, A vacancy instantly forms to prevent the Fermi level from moving

further even at 0 K. On the other hand, since A vacancy formation energy of A-excess β phase is much higher than the case of B-excess even with Fermi level at the edge of conduction band, A vacancy doesn't keep the β phase from being *n*-type. As a consequence, even though B-excess condition cannot allow the β phase to be *n*-type semiconductor, switching the thermodynamic states to A-excess β phase makes it possible.

Just as we found in β phase where the killer defect formation can be overcome by utilizing different thermodynamic states, so also do we find the case in a real material, Mg_3Sb_2. In the first report of *n*-type Mg_3Sb_2-based compounds, its *n*-type conduction was attributed to large solubility of Mg as Mg interstitials.[47] However, both our computational and experimental results indicate no sign of a large solubility of Mg (details can be seen in chapter 4), and *p*-to-*n* transition can only occur when the killer Mg vacancy formation is suppressed through tuning its chemical potential. This result was elucidated by phase boundary mapping and this concept is particularly important when the target phase contains elements having high volatility and reactivity, which drastically increases the chance of deviation in "actual" nominal composition from the weighed nominal composition. The difference in nominal Mg contents x giving *p*-to-*n* transition can be explained by this deviation.

2.6 Ternary cases

In this section, we will discuss two merits to apply phase boundary mapping to ternary compounds with a schematic ternary phase diagram: (1) it can access different doping regimes which may be inaccessible with conventional synthesis schemes, and (2) it can enhance the reproducibility of samples.

A schematic of an isothermal section of the A-B-C ternary phase diagram is shown in Fig. 2.4(a). Single-phase regions of line compounds such as the η phase are generally too small to be fully described in the full scale ternary phase diagram. Accordingly, two-phase regions such as $\eta + \alpha$, $\eta + \beta$, and $\eta + \gamma$ formed with tie-lines between single-phase regions become lines with no apparent width. However, as with the β phase in Fig. 2.3(b) discussed in the previous section, both single- and two-phase regions have finite phase width as shown in Fig. 2.4(b). With phase boundary mapping we utilize the wide three-phase regions with $F = 0$ ($C = 3, P = 3$. T and p are constant). The degrees of freedoms in the single-phase and two-phase regions are $F = 2$ and $F = 1$ respectively.

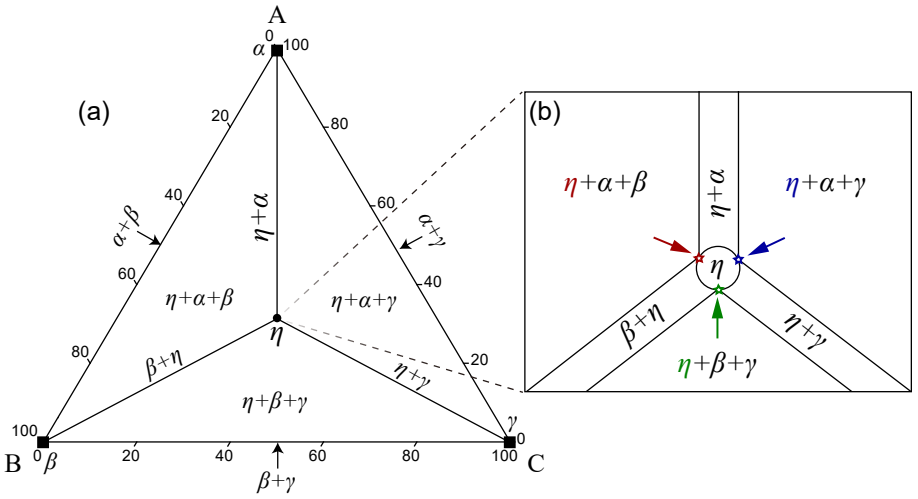

Figure 2.4: A schematic of isothermal section of A-B-C ternary phase diagram and its magnification around the single phase region of η. Although the single- and two-phase regions are small in (a), they have finite size and width as shown in (b). Those finite size and width of single- and two-phase regions lead to the discrete composition of η phase in different three-phase regions.

Consider the case where the η phase in Fig. 2.4 is our target phase, and the "actual" nominal compositions of samples are close to the single-phase region but in one of the three-phase regions. Although the single- and two-phase regions posses finite widths, in practice, synthesized samples indeed most likely fall into one of the three-phase regions around the target phase due to the systematic occurrence of reasons listed in section 2.4. Suppose the sample is now in $\beta + \eta + \gamma$ three-phase region, since the degrees of freedom in three-phase region is zero, all the composition of three phases coexisting in a sample are invariant. Therefore, as well as the compositions of secondary β and γ phases, the composition of the target phase of η is fixed at an apex of the triangle of the three-phase region as shown in Fig.2.4(b) with a green arrow. When actual nominal composition is changed from one three-phase region to another three-phase region, for example from $\eta + \beta + \gamma$ to $\eta + \alpha + \beta$ region, the invariant η phase compositions also moves, accordingly, from a spot pointed by a green arrow to a red arrow. Therefore, the defect density and ultimately the charge carrier concentration can be tuned by changing the three-phase region, namely thermodynamic states, in which the target η phase belongs to.

In the case of this simple example, there are only three different thermodynamic states around η, but the number of thermodynamic states increases following the increase in the number of stable compounds which can coexist with the target phase.

Normally a multitude of thermodynamic states exist and those can be utilized for precise tuning of carrier concentration through the phase boundary mapping as shown in the study of $Ca_9Zn_{4+x}Sb_9$ in chapter 5.[32] By mapping out the phase boundary in the nominal composition space, the systematic change in charge density was achieved without any extrinsic dopants. This work also confirmed that phase boundary mapping is eminently helpful to solve the issue of sample reproducibility. As shown in Fig. 5.16 in chapter 5, once the phase boundaries are mapped out, samples with the desired properties can repeatedly be accessible.

Chapter 3

Methods

3.1 Summary

Although much of current thermoelectric research focuses on single crystals, thin films, and nanomaterials such as nanowires, polycrystalline bulk samples prepared by simple mechanical alloying and consolidation have the immediate potential for mass production and practical use.[167, 168] This chapter discusses the synthesis and characterization of inorganic polycrystalline thermoelectric materials. The first section briefly summarizes the general synthesis methods of bulk polycrystalline samples (mechanical alloying and consolidation) followed by details of the individual procedures taken for synthesizing the various thermoelectric Zintl compounds discussed in this thesis (Mg_3Sb_2-based compounds, $Ca_9Zn_{4+x}Sb_9$, $Yb_9Mn_{4.2-x}Zn_xSb_9$, and $Yb_9Zn_{4+y}Sb_9$). The thermoelectric properties of the bulk samples synthesized in this thesis were primarily characterized by in-house built measurement equipment at Caltech/Northwestern with some results confirmed by measurement at NASA/Jet Propulsion Laboratories (JPL) or Panasonic. The following two sections discuss the characterization techniques: the structure and elemental analysis in section 3.4 and the measurement procedures and principles of electronic and thermal transport properties in section 3.5. Computational methods including band structure calculations, defect formation energy calculations, and phase diagram calculations are discussed briefly in the last section.

Only when systematic synthesis and characterization are performed can experimental results be compared consistently and a deeper understanding of the underlying materials science developed. This is particularly true in thermoelectric materials where relevant transport properties can be dramatically altered during synthesis through changing point defect concentrations. Therefore, all samples in this thesis were synthesized with the procedure maintained as consistent as possible after the most reproducible methods for each material were determined. The accuracies and precisions in results from each measurement system and potential error sources are also discussed in this chapter.

3.2 General sample preparation

Synthesis

Melting

Melting from a mixture of pure elements is one of the most commonly used techniques for the synthesis of inorganic materials. In this method, stoichiometric quantities of raw materials are sealed in an ampoule under vacuum, placed in a furnace, and held at an elevated temperature in order to melt and mix the starting materials, and then slowly cooled or quenched. Although this straightforward method works well for the synthesis of relatively simple and stable compounds such as Bi_2Te_3 or PbTe, it is not as easy for complex multinary compounds such as complex thermoelectric Zintl compounds due to the local off-stoichiometry during the synthesis. For example, consider the synthesis of a ternary Zintl compound composed of Ca, Zn, and Sb. Four different Ca-Zn-Sb ternary have been reported and many more stable binary combinations of these three elements such as $Ca_{11}Sb_{10}$, ZnSb, $CaZn_{11}$ $CaSb_2$, and Zn_4Sb_3, etc. are known to exist.[32] Local off-stoichiometry can easily fall into one of the stable compositions lying close to the target phase on the Ca-Zn-Sb ternary phase diagram, resulting in an inhomogeneous sample with undesired byproducts. The inorganic solid state chemistry has taken the advantage of these inhomogeneities. To discover the new multinary compounds, single crystal XRD was conducted on tiny crystals selected out of many small products of different shapes and colors obtained from the same reaction.[169] Indeed, many thermoelectric Zintl compounds were originally identified by melting with Sn, Pb or other melting fluxes.[108, 117, 170–173] However, when investigating the bulk thermoelectric properties of the materials of interest, small micron-order crystals or inhomogeneous samples with substantial effect from byproducts are not ideal. In addition, increasing the yield is challenging and the loss of volatile or reactive elements such as Mg, Zn, or Ca due to sublimation or undesirable reaction with environment. These add complexity to the analysis of the resulting samples. Therefore, the studies described in this thesis have employed mechanical alloying as a primary synthesis method.

Mechanical alloying

Mechanical alloying via a dry, high-energy ball mill is a type of solid state reactions which can produce homogeneously distributed nanoscale fine powder from a stoichiometric composition of pure elements. This method has great control over

the nominal composition and also significantly reduces the synthesis time compared with melting and normal solid state reaction. Inorganic synthesis via mechanical alloying was first developed by John Benjamin *et al.* in the 1960's as a result of extensive researches on nickel based superalloys for gas turbine applications.[174–176] High-energy ball milling was utilized for particle size reduction before Benjamin *et at.*,[167, 168, 177] but since then, many researches have investigated the applications of mechanical alloying [178] and its background physics.[179, 180] Different types of mills such as vibration mills,[168] planetary mills,[181, 182] attritor mills,[183] and mixer/shaker mills [184] were developed.

In this thesis, one kind of mixer/shaker mill commercialized by SPEX CertPrep was utilized to conduct the mechanical alloying.[185] Twenty minutes of milling in a SPEX mill is equivalent to 20 hours of milling in a low energy mill.[186] The 3-inch tall hardened stainless-steel vial which contains 4 to 10 grams of starting materials with milling media (two half inch stainless steel balls) were shaken back and forth several thousand times a minute.[31, 32, 102] Vials were sealed with o-rings under inert atmosphere to prevent from oxidation during the process.

The process of mechanical alloying is fairly straightforward; the powder particles in the vial are repeatedly collided by the balls, flattened, cold welded, hardened, fractured, and rewelded.[167, 187] At the early stage of milling, the soft ingredients of Zintl compounds are welded together and layered by collisions. The continuous impacts plastically deform the agglomerated powder particles, resulting in hardening. Then the particle size of hardened powder decreases due to fracturing caused by fatigue and fragmentation. After a certain amount of milling, the reduction in the particle size saturates due to balancing of agglomeration due to welding with the fracture rate. At this stage, while the average particle size remains constant, the inter-layer spacing in each particle (diffusion length) continues decreasing with the increasing number of layers within a particle.[188] Accumulated strain leads to the presence of variety of defects such as vacancies, dislocations, stacking faults, and grain boundaries and these defect structures increase the diffusivity of solute into matrix.[189] In addition, the reduced diffusion length due to the reduction of inter-layer spacing and the temperature elevation during milling enhance and accelerate the diffusion, resulting in alloying taking place in between the constituents. Sufficient ball milling leads to the completion of the reaction/alloying.

The raw materials employed for mechanical alloying are often pure powders in the range of 1 $\sim$ 200 μm in size. However, the powders can contain non-negligible

amounts of surface oxidation attributable to their large surface areas. Since the particle sizes of starting elements are not critical in the milling process, we prefer to start from larger-size raw ingredients such as slugs or rods to minimize the effect of oxidation. Starting elements were cut into ~ 1 mm diameter pieces before loading. Resulting powders after ball milling were then extracted from the vials under inert atmosphere to prepare for consolidation as discussed in the following section. The reader may refer to [167] for a comprehensive review of mechanical alloying including history, variations, mechanisms, and applications.

Consolidation

Mechanical alloying can provide a fine powder where elements are homogeneously distributed, but true alloying may not be completed if the milling duration is insufficient. To ensure reaction completion and to obtain measurable bulk samples, the consolidation is conducted at an elevated temperature by a rapid hot press system (RHP). RHP is an in-house built equipment, which is developed to rapidly consolidate thermoelectric materials by induction heating under the controlled atmosphere, pressure, and temperature.[190] The following is the typical procedure of preparing and performing RHP.

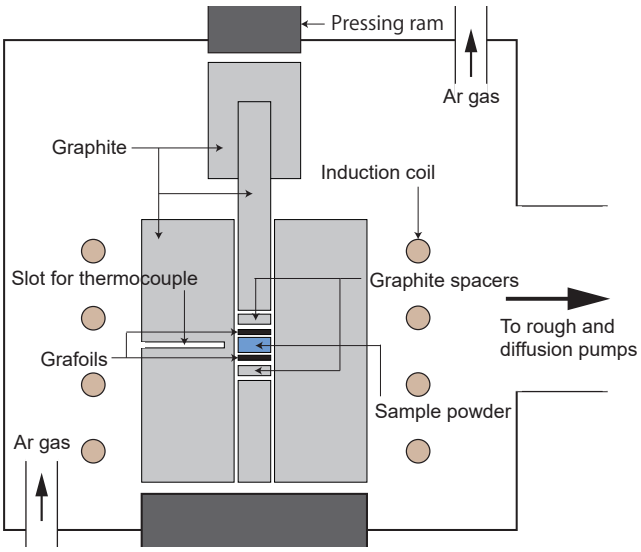

Figure 3.1: Schematic of the graphite die for RHP. Milled powder was loaded into the graphite die with a half-inch hole with grafoil spacers (both sides had two grafoil spacers with the thickness of 0.13 mm). There is a hole on the side of the die near the sample position for a thermocouple to allow measurement and control the temperature during pressing. A type-K thermocouple is utilized for temperature reading.

First, 1 - 2 g of milled powder was loaded into a graphite die with graphite and grafoil spacers as shown in Fig.3.1. It is worthwhile to calculate the predicted thickness of the resulting sample from the amount of powder loaded and the theoretical density of the target material. Next, the die is placed inside the copper induction coil within a vacuum chamber with a thermocouple reading the temperature near the sample position (see Fig3.1). The chamber has roughing and diffusion pumps attached which can evacuate the chamber down to ~ 10^{-5} Torr to protect the powder from oxygen and water during the consolidation. After applying pressure (normally ~ 40 - 45 MPa) and flowing inert gas (argon gas), the RF field was provided through the copper coil to rapidly heat up the die by induction heating (the maximum oscillating power is 15 kW and the normal operating heating current is 300 A). The electrically conductive graphite die plays the role of a susceptor and heats up almost uniformly due to its high thermal conductivity. Here, one should note that it is important to ensure the temperature reading is actually going up. Otherwise, there is a chance of thermocouple breakage or it might not be in the proper position, which can lead to applying maximum power and result in a serious damage to your material, the die, or the system. After applying the desired heat and force for the required duration, the pressure is released and the sample quick cools via the gas and the cooling water within the chamber and copper tubings, respectively (~ 300 K/h). The disk-shaped sample pellet with the diameter of a half-inch and a hight of 1 - 2 mm is then obtained. The dry and wet densities of resulting pellet were attained by measuring the geometric volume and weight and by Archimedes method with pure ethanol to assess the pressing profile. The desired density is over 95% of its material's density. Once a dense pellet was obtained, it was then used for chemical and physical characterization, which are discussed in sections 3.4 and 3.5.

The motivation to utilize this RHP system can be understood when compared with two different widely used consolidation techniques: hot pressing with resistive heaters (HP) and spark plasma sintering (SPS). While HP and SPS are capable of consolidating the powdered materials, they have several disadvantages. The largest disadvantage of utilizing HP is its slow heating and cooling rates. The heater needs to raise the temperature of the entire chamber solely by radiation and the large thermal mass of the resistive heaters themselves slows down the heating and cooling. Slow heating and cooling make the precise tracking of the effect of pressing temperature and duration harder, increase the power required for running, and delay research progress. On the other hand, SPS system can raise the temperature of the die as quickly as RHP through resistive heating of the die body and rods themselves,

and densify the sample even faster than the other two methods due to the pulsed current running through the sample.[191] Thus, SPS is often considered as the better technique to obtain samples with smaller grain size, potentially reducing the lattice thermal conductivity.[192] However, a poor understanding of the effect of the current-assist sintering sometimes leads to a significantly large variation of the physical and chemical properties in the resulting samples. Therefore, for the sake of the consistent research and excluding unknown effects as much as possible, we utilize RHP to consolidate our samples. Interested readers can refer to ref. [190] for a more comprehensive comparison and the detail specifications of the RHP system, or to ref. [191] for the details of the SPS technique.

3.3 Synthesis methods of individual studies

Mg_3Sb_2-based compounds

Magnesium slugs (99.95%, Alfa Aesar), antimony shots (99.9999%, Alfa Aesar), bismuth granules (99.997%, Alfa Aesar), and tellurium lumps (99.999%, Alfa Aesar) were used for the sample set #1 (see below) as starting elements. Note that the purities reported by the manufacturer are "metals basis" meaning that the oxygen content is unknown. Each of the raw materials was cut into small pieces, weighed to be the stoichiometric amount, and loaded into a stainless-steel vial with half-inch stainless-steel balls under argon. Mechanical alloying was conducted by a SPEX high-energy mill (8000D) for two hours. The black powder was extracted from the vial and transferred to a high-density graphite die in a globe box. Subsequently, induction heating RHP was conducted at 873 K with 45 MPa for one hour with flowing argon.[190] Both geometric and wet densities of the pressed disk-shaped pellets were measured and confirmed to be > 95%. Samples of sample set #2 (see below) were prepared with a different method and the details were discussed in Ref [47]. Following planetary ball milling with a process control agent (stearic acid), pressing was done by SPS instead of RHP.

Sample set #1:

$Mg_{3+x}Sb_2$ (x = -0.1, 0, 0.2, 0.3), $Mg_{3+x}Sb_{1.99}Te_{0.01}$ (x = -0.2, -0.1, 0, 0.1, and 0.2), $Mg_{3.2}Sb_{2-y}Te_y$ ($y = 0.005, 0.01, 0.03, 0.06, 0.08, 0.1,$ and 0.15), and $Mg_{3+x}Sb_{1.5}Bi_{0.49}Te_{0.01}$ (x = 0.2) were prepared and measured at Northwestern University.

Sample set #2:

$Mg_{3+x}Sb_{1.5}Bi_{0.49}Te_{0.01}$ ($x = 0.1, 0.16, 0.18, 0.2,$ and 0.3) and $Mg_{3.2}Sb_{1.5}Bi_{0.49-y}Te_y$

(y = 0, 0.005, 0.01, 0.015, 0.02, and 0.04) were synthesized and measured at Panasonic.

$Ca_9Zn_{4+x}Sb_9$

In prior research, $Yb_9Mn_{4+x}Sb_9$ and $Yb_9Zn_{4+x}Sb_9$ (detail shown in following section 3.3) were prepared by placing constituent elements into a stainless steel vial and then ball milled for one hour followed by hot pressing at 800 °C for two hours at a pressure of 40 MPa.[30, 31] When $Ca_9Zn_{4+x}Sb_9$ samples were synthesized by the same procedure, the resulting samples contained significant amounts of impurity phases. Further investigation revealed that the samples were Zn deficient after hot pressing. Knowing this, $Ca_9Zn_{4+x}Sb_9$ (x = 0.2, 0.3, 0.4, 0.5, 0.6, 0.7, and 0.8) samples were prepared through an alternative approach of two-hour ball milling followed by a two-step hot pressing and annealing. In an argon-filled glove box, stoichiometric amounts of Ca dendrites (99.99%, Sigma-Aldrich), Zn shot (99.999%, Alpha Aesar) and Sb shot (99.999%, Alpha Aesar) were loaded into a stainless steel vial with two half-inch stainless steel balls. Samples were then ball-milled for two hours in a SPEX Sample Prep 8000 Series Mixer/Mill. The resulting powders were hot-pressed in a high-density graphite die under argon atmosphere. To ensure that Zn is completely reacted, samples were pressed with a 40 MPa load for two hours at 350 °C, which is slightly lower than the melting temperature of Zn. Then the samples were pressed for two more hours at 800 °C to make dense pellets. At the end, all samples were sealed in silica ampules under vacuum and annealed at 580 °C for six days to obtain homogenous materials. All samples were found to have wet densities of over 97 %. They are relatively stable under ambient conditions as samples exposed to air for about a month had surfaces which were still shiny and metallic in appearance.

$Yb_9Mn_{4.2-x}Zn_xSb_9$ and $Yb_9Zn_{4+y}Sb_9$

$Yb_9Mn_{4.2-x}Zn_xSb_9$ (x = 0, 1, 2, 3 and 4.2) and $Yb_9Zn_{4+y}Sb_9$ (y = 0.2, 0.3, 0.4 and 0.5) samples were prepared by ball milling followed by hot pressing. The elements were loaded into stainless-steel vials with stainless-steel balls inside a glove box filled with argon. The materials were dry ball-milled for an hour using a SPEX Sample Prep 8000 Series mixer/mill. The resulting fine powder was hot-pressed in high-density graphite dies using 40 MPa on a 12.7 mm diameter surface. Samples were hot pressed using a maximum temperature of 1073 K for 2 hours under flowing argon, followed by 2 hour cooling.

3.4 Structural and elemental analysis

The structure, homogeneity, chemical composition, and the presence of any secondary phases in the resulting disk-shaped samples were characterized by X-ray diffraction (XRD), scanning electron microscopy (SEM), energy dispersive spectroscopy (EDS), and wave dispersive spectroscopy (WDS).

XRD on the bulk samples of $Yb_9Mn_{4.2-x}Zn_xSb_9$, $Yb_9Zn_{4+y}Sb_9$ and $Ca_9Zn_{4+x}Sb_9$ were performed using a Philips PANalytical X'pert MPD diffractometer operating at 45 kV and 40 mA with CuKα radiation at Caltech. Rietveld analysis was performed using Philips X'part plus software for $Yb_9Mn_{4.2-x}Zn_xSb_9$ and $Yb_9Zn_{4+y}Sb_9$, and WinCSD program package for $Ca_9Zn_{4+x}Sb_9$, respectively. ZEISS 1550VP field emission SEM with Oxford EDS was utilized to conduct SEM and EDS on $Yb_9Mn_{4.2-x}Zn_xSb_9$, $Yb_9Zn_{4+y}Sb_9$ and $Ca_9Zn_{4+x}Sb_9$ at Caltech. The WDS on $Ca_9Zn_{4+x}Sb_9$ was performed by JEOL JXA-8200 with Probe for electron probe micro-analyzer (EPMA) for EPMA software which provides full digital-control for more reliable and automated WDS microanalysis and digital imaging.[193] On the other hand, XRD on Mg_3Sb_2-based compounds were performed by STOE's STADI MP at Integrated Molecular Structure Education and Research Center (IMSERC) located at Northwestern University. STADI MP was operated at 45 kV and 20 mA with pure Kα1 radiation. The software used for refinement was GSASII. SEM, EDS and WDS on Mg_3Sb_2-based compounds were performed with Hitachi S-3400N-II with Oxford INCAx-act SDD EDS, and wave WDS system for elemental analysis at the EPIC facility of Northwestern University's NUANCE center.

It should be noted that these structural and elemental analysis were used only for determining the matrix phase and the identity of secondary phases equilibrated with the target matrix phase in this thesis. Although the relative trend in the elemental analysis is often reliable (typical precision of WDS is ~ 0.X% [194]), the determination of exact chemical composition is not always straightforward and reliable enough (typical accuracy of WDS is ~ 2% [194]) to be compared with the transport properties such as resistivity and Hall carrier concentration. For example, the range of the chemical carrier concentration can differ from 0 cm^{-3} to ~10^{21} cm^{-3} when the composition is varied from $Mg_{3.00}Sb_2$ to $Mg_{3.06}Sb_2$ (by 2 at.% of Mg). Therefore, careful treatment is required for comprehensive analysis, combining the transport properties with elemental analysis.

3.5 Measurement methods and principles

Seebeck measurement

The Seebeck coefficient was measured under dynamic vacuum with a home-built system described in ref.[195] constructed by former group members. The disk-shaped sample is placed between two machinable boron nitride (BN) substrates with cartridge heaters embedded. The Chromel/Nb thermocouple placed through the BN substrates are pressed on the sample disk as shown in Fig. 3.2. The entire measurement system is placed inside the vacuum chamber to conduct the measurement without oxygen and moisture, which can affect the sample properties. The top and bottom temperatures of substrates (T_{top} and T_{bottom}) are controlled by the external program (PID control) to reach the desired average temperature. Once the T_{top} and T_{bottom} reaches the target temperatures, the temperature gradient applied to the sample ΔT (= $T_{top} - T_{bottom}$) is oscillated about a fixed average temperature ($T_{average}$). The voltage response to the temperature osculation (ΔV) is continuously measured during the oscillation. Fig.3.2(b) shows an example data of T_{top}, T_{bottom}, and $T_{average}$ (= $(T_{top} - T_{bottom})/2$) as a function of time and Fig.3.2(c) shows the resulting ΔV response to the oscillated ΔT. Here, ΔT was set to oscillate ± 7 K within 55 minutes. Since $\alpha = -\Delta V/\Delta T$ as explained in the Chapter 1, the slope of the linear fit of $\Delta V vs. \Delta T$ is a Seebeck coefficient at the temperature of the average of $T_{average}$.

The uniaxial geometry of Seebeck system shown in Fig3.2(a) was originally developed at NASA-JPL in the 1980's and has several advantages compared to the widely used configuration in old instruments or commercial systems.[195, 196] In the past era, the thermocouples measuring temperature and voltage were embedded within metal substrates and those metals were in contact with the top and bottom side of the bar-shaped sample to play the roles of heat source and sink. However, such a system can inherently include thermal and electrical resistances of the substrate metals. Later, the error caused by the internal thermal and electrical resistances of substrate were eliminated by contacting the thermocouples directly on the side of the bar-shaped sample. This sample and probe configuration is widely applied in commercial systems. However, this configuration still possesses some major issues. One is a contact issue. Since the thermocouples are pushed on the side with spring force, soft materials may deform at high temperature, and lose good thermal and electrical contact. Furthermore, a non-negligible temperature gradient can exist within the beads at the tip of thermocouple leading to the temperature difference between the points measuring temperature and voltage. This is called

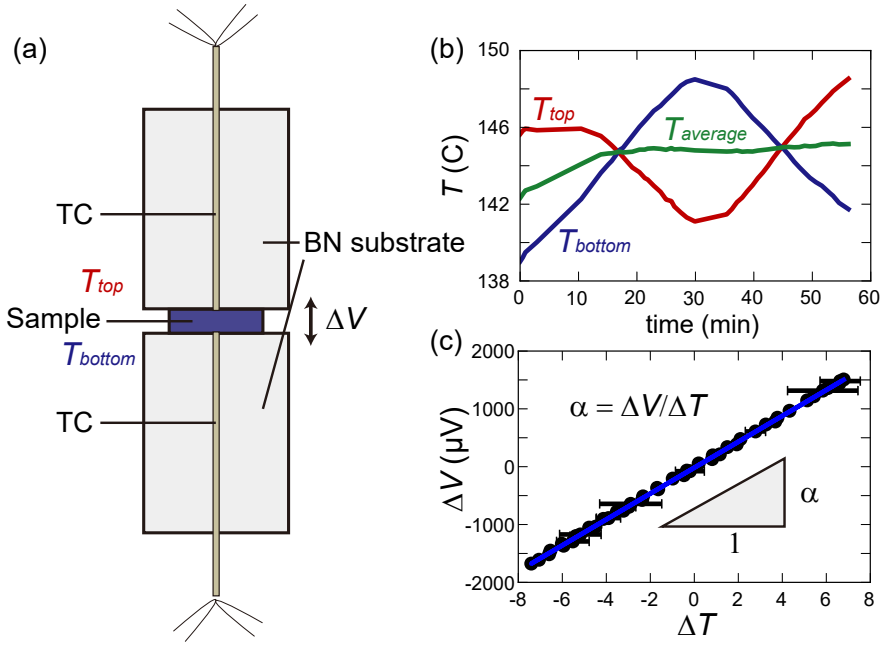

Figure 3.2: (a) Schematic figure of the Seebeck measurement system and (b) example osculation data and (c) $\Delta V vs \Delta T$. The oscillation is for excluding any voltage offset in the measurement. The slope of the linear fit shown in (c) is a Seebeck coefficient at the average of $T_{average}$. The range of ΔT and the oscillation time are set to be ± 7 K and 55 min, respectively.

the "cold-finger effect" and leads to an error in measurement. The interested reader can refer to ref.[195] and [197] for more details. The high temperature Seebeck measurement is often considered as an erroneous measurement compared to the techniques for assessing thermal and electrical transport properties due to the reasons listed above and in the following Refs. [11, 198, 199]. However, both accuracy and precision can be improved by redesigning the sample and probe configuration as shown in Fig.3.2(a). The thermocouples are directly in contact with the disk-shaped sample with uniaxial pressure from top and bottom. This provides good thermal and electrical contact over a wide temperature range and allows a variety of sample geometries to be measured including disk-shaped to be measured. Grafoil spacers are placed between thermocouple and sample to prevent contamination but they are electrically and thermally negligible. The cold finger effect can also be suppressed by maintaining the sample and thermocouple tip temperature uniform. Furthermore, the disk-shaped samples can be loaded to the thermal transport measurement system and Hall measurement system described in the following sections so that all the characterizations can be performed on a single sample, whereas bar-shaped

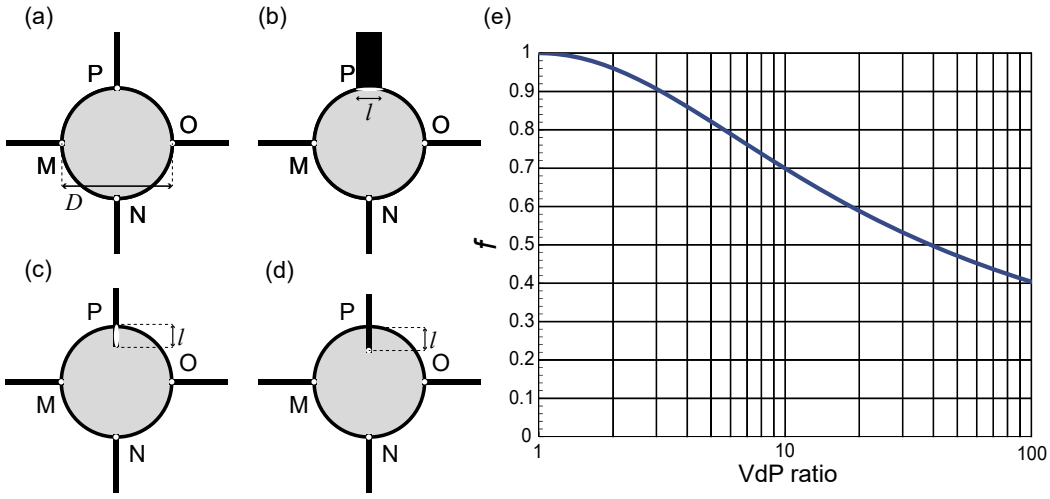

Figure 3.3: Schematic figures of the different lead configurations for the Hall measurement. Gray circles are disk-shaped samples with the diameter of D. (a) Ideal configuration. (b) One of the contacts has a length l along the edge. (c) One of the contacts has a length l perpendicular to the edge. (d) One of the point contacts is located at a distance l from the edge. (e) Numerical solution of the factor f as a function of the VdP ratio. The correction factor f < 95% when VdP ratio is smaller than 2.

samples are not suitable for this purpose. The precision of the Seebeck results with the uniaxial geometry is normally within ± 5 μV/K and we estimate the typical accuracy of the measurement to be ~ 10% for reproducible data.[195]

Resistivity and Hall effect measurement

Hall effect measurements combined with simultaneously measured resistivity can provide important insights when researching semiconductors and metals such as charge carrier density and carrier mobility. These values can be used to estimate the effective mass of the charge carriers and the possible scattering mechanism when they are measured as a function of temperature. The high temperature resistivity and Hall effect measurement were conducted under dynamic vacuum using a home-built Hall system using four point Van der Pauw (VdP) method at Caltech/Northwestern and NASA-JPL with a maximum magnetic field of 2 T and 0.8 T, respectively.[200, 201]

A disk-shaped sample with a thickness of around 1 mm and the diameter of D (typically a half-inch) is placed on an alumina substrate with embedded cartridge heaters. Molybdenum probes are placed on the sample as shown in Fig. 3.1(a) and

the lead-sample contacts are ascertained by pressing the probes with screws followed by testing the contact resistances. Once good contacts are established, the substrate and sample are covered by a radiation shield and placed within a vacuum chamber with roughing and turbo pumps attached. The angle of the sample holder is adjusted so that the external magnetic field is applied at a right angle to the flat surface of the sample. The chamber is then evacuated down to lower 10^{-5} Torr within 10 - 15 min to minimize the oxidation and reaction with moisture during the measurement. The temperature of the sample stage is linearly ramped (typical ramp rate is 1.5 K/min) once the measurement sequence started. The temperature is measured by C-type thermocouple within the substrate. The resistivity and Hall effect measurement are conducted for both heating and cooling to examine the stability of the sample, potential hysteresis in the electronic properties, and measurement reproducibility.

The VdP method is applied for both resistivity and Hall effect measurements.[200–203] In practice, the brittle samples sometimes suffer from cracking or fracturing during synthesis and it might be difficult to obtain a disk-shaped sample. The largest merit using VdP method is that samples with an arbitrary shape can be measured by four probes located around edge of the sample. When the four point contacts *M, N, O,* and *P* are at the edge of the sample as shown in Fig.3.3(a), the potential difference between *P* and *O* can be measured with flowing current i_{MN} from contact *M* to *N*, and then the resistance between *O* and *P* can be obtained as in Eq.3.1.

$$R_{MN,OP} = \frac{V_P - V_O}{i_{MN}} \tag{3.1}$$

$$R_{NO,PM} = \frac{V_M - V_P}{i_{NO}} \tag{3.2}$$

Analogously the resistance between contact *P* and *M* with the current from *N* to *O* (i_{NO}) can be described by Eq.3.2. These resistances are known to fulfill the following VdP relationship obtained through conformal mapping as far as the samples are isotopic, homogeneous, flat, and free from holes.

$$\exp\left(-\frac{\pi t}{\rho} R_{MN,OP}\right) + \exp\left(-\frac{\pi t}{\rho} R_{NO,PM}\right) = 1, \tag{3.3}$$

where t is a sample thickness. This can be solved analytically when the ratio between $R_{MN,OP}$ and $R_{NO,PM}$ is unity but it is not usually the case. The ratio of two resistances is called VdP ratio (set to be ≥ 1) and the factor f appeared in Eq.3.5 can be numerically obtained by solving the following expression for given VdP ratio,

$$\cosh\left[\frac{R_{MN,OP}/R_{NO,PM}-1}{R_{MN,OP}/R_{NO,PM}+1}\frac{\ln 2}{f}\right]=\frac{1}{2}\exp\frac{\ln 2}{f}. \tag{3.4}$$

The solutions f as a function of VdP ratio is shown in Fig.3.3(e). This factor f is a correction factor to obtain the resistivity from the measured "resistances" as shown in the following equation (detailed mathematical derivation can be found in ref.[200]):

$$\rho=\frac{\pi t}{\ln 2}\frac{R_{MN,OP}+R_{NO,PM}}{2}f. \tag{3.5}$$

The correction by f is less than 5% when the VdP ratio is less than 2. If the measured VdP ratio is unexpectedly large, one might need to suspect the anisotropy, inhomogeneity, bad contact resistance, or void (hole) within the sample of interest.

The Hall carrier concentration (n_H) and Hall mobility (μ_H) can also be measured on a sample with an arbitrary shape. The magnetic field B_H applied at a right angle to the sample surface induces a magnetic force on the charge carriers flowing within the sample ($F = evB_H$ where F, e, and v are the magnitude of force induced by B_H, an electron charge, and velocity of charge carrier, respectively), resulting in the electric potential within the bulk material(E_H). With the current density J ($= n_H ev$), the induced potential can be described as $E_H = \frac{JB_H}{n_H q}$ and measured in the perpendicular direction to the current; for example, if current is flown from M to O (i_{MO}), the change in the potential difference between P and N becomes

$$\Delta(V_P - V_N) = \int_N^P E_H \mathrm{d}s = \frac{B_H}{n_H e}\int_N^P J\mathrm{d}s = \frac{B_H}{n_H e}\frac{i_{MO}}{t}. \tag{3.6}$$

Therefore, we obtain the typical expression of V_H as shown in Eq.3.7 and Hall

carrier concentration can be calculated through this relationship. The Hall coefficient R_H is defined as $1/n_H e$ and its sign indicates the sign of the majority charge carrier. Combined with simultaneously measured conductivity, the Hall mobility μ_H can also be acquired ($\sigma = n_H e \mu_H$).

$$V_H = -\frac{iB_H}{ten_H}. \tag{3.7}$$

Normally we use 1 - 100 mA for i to perform Hall measurement. As can be seen in Eq.3.6, the larger B_H, i and thinner d lead to larger signal (V_H). However, the volt meter has its own limit and measuring samples with low carrier density sometimes saturates the voltage and the proper value cannot be read. In this case, one can reduce the current so that the instrument can be capable. Analogously, reducing the sample thickness, increasing the current or magnetic field are sometimes helpful to obtain better signal to noise ratio to measure metallic samples which generate only small Hall voltage. Lastly, the magnitudes of the estimated errors caused by the non-ideal probe configurations are listed up in Table 3.1. The non-ideal probe configurations are illustrated in Fig.3.3. The error and variation of resistivity and Hall measurements are heavily dependent on the measurement condition and sample quality. The data of Hall effect measurements can become noisy for samples with low mobility or high carrier concentration. Bad contacts certainly affect the accuracy and precision. Obtaining an accurate temperature reading is not always straightforward due to the effects of radiation, the heat drawn by cold supporting rods or the chamber, an inhomogeneously heated substrate, and the time delay in the measurement sequence. A report of a round robin test on the electrical resistivity measurement with four-probe bar method concludes the variation can be as much as 10%.[199]

Thermal transport measurement

Thermal diffusivity and conductivity

Although many principles and methods of thermal conductivity measurements work well at low temperature such as the thermal VdP method,[204] various steady-state methods,[205, 206] frequency-domain transient methods,[207, 208] and the direct transient method with physical property measurement system (PPMS),[209] the heat

Probe configurations	$\Delta\rho/\rho$	$\Delta R_H/R_H$
(a)	0%	0%
(b)	$\approx \frac{-l^2}{16D^2\ln 2}$ (0.056%)	$\approx \frac{-2l}{\pi^2 D}$ (1.6%)
(c)	$\approx \frac{-l^2}{4D^2\ln 2}$ (0.22%)	$\approx \frac{-4l}{\pi^2 D}$ (3.2%)
(d)	$\approx \frac{-l^2}{2D^2\ln 2}$ (0.45%)	$\approx \frac{-2l}{\pi D}$ (5.0%)

Table 3.1: The relative errors in the resistivity and Hall measurement results caused by different probe configurations.(see Fig.3.3 for schematic images) The estimated values in brackets are calculated assuming l = 1 mm and D = 12.7 mm. It should be noted that these are not the only potential sources of error in the measurements.[200]

loss due to the radiation limits the accuracy of high-temperature measurement.[210] The heat loss (q) due to the radiation can be estimated to be

$$q = \epsilon A \Delta T T^3, \tag{3.8}$$

where ϵ, A, and ΔT are the emissivity, the surface area, and the temperature difference between sample and surrounding (here ΔT is assumed to be small).[211] Therefore, it is important to apply the proper radiation correction principle to obtain more accurate high temperature measurement results.

The laser flash method, which was first developed by Parker *et al.* in 1961,[212] was utilized to measure high-temperature thermal diffusivity (D_T) with the commercial NETZSCH Laser Flash Apparatus (LFA) 457 Micro Flash under argon flow in this thesis. Thermal conductivity (κ) was then determined by $\kappa = D_T C_p d$, where C_p is the heat capacity, and d is the geometric density. The disk-shaped samples with the thickness of 1 - 2 mm were loaded into graphite of SiC holders and placed on the sample carrier inside the furnace. The entire furnace is within a vacuum chamber with roughing and turbo pumps attached. After removing the air and moisture inside with those pumps, inert gas (argon gas) is flown at a rate of 50 ml/min to maintain the temperature read by thermocouple around the sample position as close to the samples as possible. Once the measurement sequence is started, the furnace temperature is controlled to be the set temperature with ramp rate of < 5 K/min and stabilized within a certain threshold set in the program. Subsequently, a short laser pulse is shot from the bottom and the time-domain transient of the temperature of the top sample surface was monitored by an InSb detector placed at the top and cooled by a liquid nitrogen dewar. This response to the flashed laser as a function of time is used to calculate the thermal diffusivity with sample thickness. Measurements were

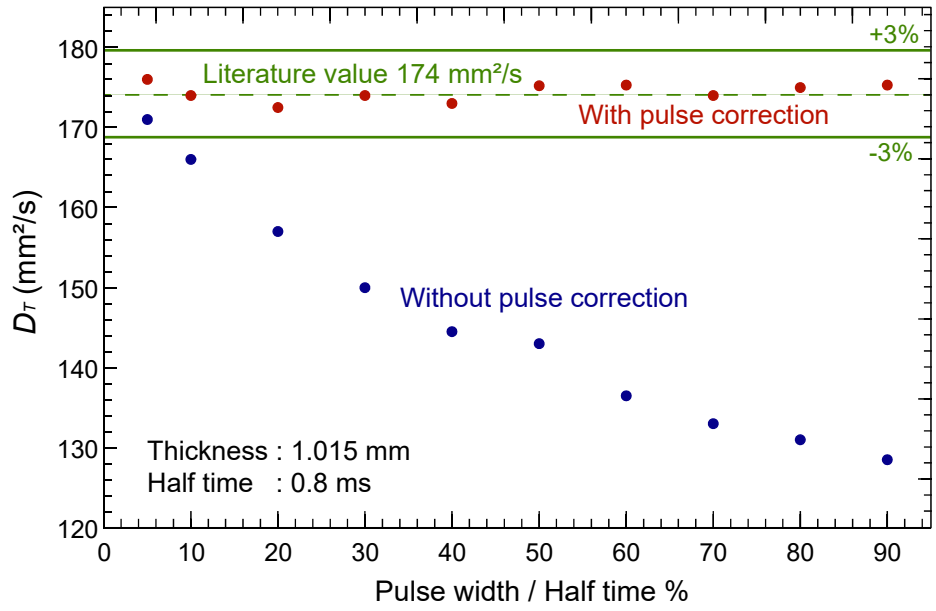

Figure 3.4: The influence of pulse correction with the measurement results of a silver plate with the thickness of 1.015 mm. The half time of this material is 0.8 ms. The data is obtained from the manual of LFA 457.[216]

repeated at least three times at the same temperature to ascertain the results. The instrument can measure from room temperature up to 1100 °C, but implementing another detector (Mercury Cadmium Tellurium) allows the instrument to measure at lower temperature (down to - 125 °C). Thinner or thicker samples than 1 - 2 mm can be measured, but samples with a thickness close to the standard material (around 2 mm for PyroCeram) is ideal.[197]

Following the original report, where Parker *et al.* assumed no heat loss to calculate the diffusivity, many radiation correction methods were proposed for more accurate estimation of thermal diffusivity.[213–215] In the LFA 457 system, we applied the Cowan + Pulse collection which implements the correction terms for the finite pulse width and the heat loss due to radiation. The influence of pulse correction is shown in Fig.3.4. The error can be non-negligibly high when the ratio between pulse width to the halftime (the response time for the temperature to increase to half-maximum) is large without pulse correction (*e.g.* When the pulse width / half time is 0.1, the error in thermal diffusivity can as large as 10%).

Although the typical measurement accuracy and precision of thermal diffusivity measurement for most of the materials are ± 2% and ± 3%, respectively, according

to the manufacturer, these values can not be estimated easily in practice due to the various potential sources of errors. The variation in the geometric thickness of measured samples is a common source when the sample surfaces are not perfectly parallel to each other. Bad adhesion of the sample coating which enhances the absorption of the laser shot, and an excess amount of coating could cause a systematic error especially for thin samples. Thermal expansion of the sample and bad temperature reading and stability can also result in error. The variation in thermal diffusivity measured at different labs can be as high as 5% at room temperature according to the ref [199]. A comprehensive and thorough review of thermal conductivity measurement of bulk and thin-film materials can be found in ref.[217]

Heat capacity

The heat capacity value is necessary to calculate thermal conductivity from thermal diffusivity as shown in the previous section. However, the high temperature heat capacity measurement is known to be very erroneous (error could be more than 15%).[197] Therefore, the Dulong-Petit heat capacity is normally used for better comparison of thermal conductivities from various samples. In this thesis, the heat capacity of $Ca_9Zn_{4+x}Sb_9$ was measured by Jan-Hendrik Póhls at Dalhousie University in Canada with following method to confirm the Dulong-Petit heat capacity is a good approximation.[32] zT could be higher with experimental C_p but it was not used in the final zT report to exclude the large measurement error from C_p measurement. The heat capacity of $Ca_9Zn_{4+x}Sb_9$ was measured by the enthalpic method using a DSC.[218] Thermograms of the background (Al_2O_3 as a standard sample) and $Ca_9Zn_{4.6}Sb_9$ were recorded with 10 K intervals from 350 K to 630 K and a scanning rate of 2 K min^{-1}. Details about the enthalpic method are given in Ref [219]. The heat capacity was confirmed by a Physical Property Measurement System (PPMS, from Quantum Design) in the temperature range from 270 K to 390 K under high vacuum ($< 10^{-4}$ Torr). The relaxation technique is described in Ref [220]. The average of experimental heat capacities was used to calculate zT of Mg_3Sb_2-based compounds since the deviation from Dulong-Petit C_p and experimental C_p is large mainly due to the dilation term in C_p. Fortunately, there is plenty of literature that contain the measured heat capacity values of Mg_3Sb_2-based compounds.

Speed of sound measurement

Ultrasonic measurements have been valuable for the study of condensed matter physics and materials science.[221] Room temperature ultrasonic measurements were performed to obtain the longitudinal (v_L) and transverse (v_t) sound velocities with honey as a coupling agent using a Panametrics NDT 5800 pulser/receiver and 5 MHz and 25 MHz shear and longitudinal transducers from Ultran and a Tektronix TDS 1012 digital oscilloscope. The Pulse-echo method is utilized here, and which is based upon the principle of backscattered acoustic pulses. The process is basically the same as sonar. The acoustic energy applied to one side of the sample travels through the bulk and gets reflected from the backside surface. While the pulse is bounced back and forth, the reflections are monitored as a function of time. The observed interval of the signals is the time that the pulse takes to travel twice the sample thickness. The glassy limit lattice thermal conductivities described in the introduction and the bulk and sheer moduli can be estimated from values of speed of sound (see following equations). There are other techniques such as resonant ultrasonic spectroscopy with a continuous wave. The interested reader can refer to the following references [222, 223]:

$$v_T = \sqrt{\frac{G}{d}} \tag{3.9}$$

$$v_L = \sqrt{\frac{K + \frac{4}{3}G}{d}}. \tag{3.10}$$

3.6 Computational methods

Electronic band structure calculation

Density-functional-theory (DFT) calculations of $Ca_9Zn_{4+x}Sb_9$ were carried out by Maximilian Amsler in Chris Wolverton's lab at Northwestern University within the projector augmented wave formalism as implemented in the Vienna Ab Initio Simulation Package (VASP)[224] using the Perdew-Burke-Ernzerhof (PBE)[225] exchange-correlation functional.[32] A plane-wave cutoff energy of 500 eV was used together with a sufficiently dense k-point mesh of $5 \times 5 \times 4$, for $Ca_9Zn_4Sb_9$, resulting in total energies converged to less than 1 meV/atom. Both atomic and cell variables were relaxed simultaneously until the forces on the atoms were less than 3 meV/Å, and the stresses were less than 0.1 eV/Å^3. The resulting cell parameters

are a = 21.855 Å, b = 12.518 Å, and c = 4.560 Å, which are in good agreement with experimental values (see Fig. 5.3 in section 5). The relaxed atomic positions occupy the Wyckoff sites according to the table 5.1. Since semilocal exchange-correlation functionals in DFT are well known to systematically underestimate band gaps, the Kohn-Sham band structure with the more accurate hybrid HSE06 functional was calculated.[226–228]

Phase diagram calculation

The temperature dependent dilute-limit solvus boundaries for Mg_3Sb_2 in the Mg-Sb-Te ternary phase space were constructed using defect formation energies calculated from DFT in conjunction with a statistical mechanics model. This calculation was performed by a member of Northwestern Thermoelectric group, Shashwat Anand. The formation energy ΔE^j_{def} for defect j was calculated as a function of Fermi level measured from E_V ($\epsilon_F = E_F - E_V$) and atomic chemical potential due to a set of N-phase equilibrium ($\mu^o_i + \Delta\mu_i$), using:

$$\Delta E^j_{def}(\Delta\mu, \epsilon_F) = E^j - E^o - \sum_{i=1}^{3} \Delta N^j_i (\mu^o_i + \Delta\mu_i) - \Delta N^j_e (E_V + \epsilon_F), \tag{3.11}$$

where ΔN^j_i is the number of atoms of the species i added ($\Delta N^j_i > 0$) or removed ($\Delta N^j_i < 0$) from the pure supercell to construct the defect supercell. μ^o_i is the atomic chemical potential of the species i in the standard elemental state at T = 0 K and $\Delta\mu_i$ is the atomic chemical potential relative to μ^o_i in a particular set of phase equilibria. ΔN^j_e and E_V are the number of electrons added ($\Delta N^j_e > 0$) or removed ($\Delta N^j_e < 0$) from the defect containing supercell and the valence band maximum, respectively. As μ^o_i is a constant, the dependence of ΔE^j_{def} on atomic chemical potential in a set of phase equilibria can essentially be captured through $\Delta\mu_i$. We determine $\Delta\mu^{3,m}_i$ for three-phase region m (described by the notation in the superscript), using:

$$\Delta H_k = \sum_{i=1}^{3} c_{ik} \Delta\mu^{3,m}_i, \tag{3.12}$$

where ΔH_k and c_{ik} are the formation energies of the phase k and the composition of the atomic species i in this phase. The set of $\Delta\mu^{2,l}_i$ for a two-phase regions l common to adjacent three-phase regions m and q were calculated as a weighted sum of $\Delta\mu^{3,m}_i$ and $\Delta\mu^{3,q}_i$, using:

$$\Delta\mu_i^2 = (1-\lambda)\Delta\mu_i^{3,m} + \lambda\Delta\mu_i^{3,q}, \tag{3.13}$$

where λ ($0 < \lambda < 1$) is the weighting fraction.

The temperature dependence of ϵ_F in Eq. 3.11 was determined through reduced Fermi level ($\eta = \epsilon_F / k_B T$) by numerically solving for the charge neutrality condition given by

$$n - p + \sum_j \Delta N_e^j n_j = 0, \tag{3.14}$$

where the number of electrons (n) and holes (p) in the system are calculated using the effective band model equations:

$$n, p = 4\pi \left(\frac{2m_{c,v}^* k_B T}{h^2} \right)^{3/2} F_{1/2}(\eta) \tag{3.15}$$

$$F_n(\eta) = \int_0^\infty \frac{e^n d\epsilon}{e^{\epsilon-\eta} + 1}. \tag{3.16}$$

The sum in Eq. 3.14 is the charge due to point defects in the system where the concentration of the defect j (n_j) is calculated using

$$n_j = N_{site}^j \exp\left(\frac{-\Delta E_{def}^j}{k_B T} \right), \tag{3.17}$$

where N_{site}^j is the site density of defect the j. The change in the number of atoms of species i (per formula unit) relative to the stoichiometric 0 K phase due to equilibrium concentration of defects is given by

$$\Delta N_i(T, \Delta\mu) = \sum_j \Delta N_i^j n_j. \tag{3.18}$$

Using Eq. 3.18, the temperature dependence of composition for element i at the phase boundary is calculated by

$$x_i(T, \Delta\mu) = \frac{N_i^o + \Delta N_i}{\sum_i \left(N_i^o + \Delta N_i\right)}. \tag{3.19}$$

For constructing the phase boundary around Mg_3Sb_2 single-phase region we consider the most stable charged states across the band-gap of Mg_3Sb_2 such as V_{Mg}^{2+}. (See ref [229]). The slight underestimation of predicted dopant solubility is what is expected from the dilute limit approximation, which does not take into account defect interactions and changes in vibrational entropy.[230]

Defect formation energy calculation

The defect formation energies of intrinsic and extrinsic defects were calculated by our collaborator Hiromasa Tamaki at Panasonic, Japan. E^j and E^o in Eq.3.11 are the DFT total energy of the defect containing Mg_3Sb_2 supercell and the pristine Mg_3Sb_2 supercell, respectively. E^j and E^o were computed in $2 \times 2 \times 2$ supercell using the Vienna ab initio simulation package with the plane-wave-basis projector-augmented-wave method.[231] The generalized gradient approximation of Perdew, Burk, and Ernzerhof was used.[225] Reciprocal spaces of the supercells were sampled by $6 \times 6 \times 3$ Γ-centered meshes. The plane-wave-energy cut-off was 500 eV. The internal structure of each defect supercell was optimized until all components of the Hellman-Feynman force were less than 0.02 eV/Å.

Chapter 4

Phase boundary mapping to obtain *n*-type Mg_3Sb_2-based thermoelectrics

This chapter contains contents that have been submitted to a journal. Once it is accepted, permission will be asked.

4.1 Summary of research

Zintl compounds make excellent thermoelectrics with many opportunities for chemically tuning their electronic and thermal transport properties. However, the majority of Zintl compounds are persistently *p*-type even though computation predicts superior properties when *n*-type. Surprisingly *n*-type Mg_3Sb_2-based thermoelectrics have been recently found with exceptionally high figure-of-merit (zT). Excess Mg is required to make the material *n*-type prompting the suspicion that interstitial Mg is responsible. Here we explore the defect chemistry of Mg_3Sb_2 both theoretically and experimentally to explain why there are two distinct thermodynamic states for Mg_3Sb_2 (Mg-excess and Sb-excess) and only one can become *n*-type. We find that it is the suppression of Mg vacancies with excess Mg and not the formation of Mg interstitials that is key to enable the preparation of these extraordinary *n*-type thermoelectrics. This work emphasizes the importance of exploring all of the multiple thermodynamic states in a nominally single-phase (line compound) semiconductor. This understanding of the existence of multiple inherently distinctly different thermodynamic states of the same nominal compound will vastly multiply the number of new complex semiconductors to be discovered for high zT thermoelectrics or other applications.

4.2 Introduction/background

Introductory textbooks often wish to tabulate materials properties such as electrical and thermal conductivity of pure materials, including semiconductors, such as Si, Sulfur, GaAs, ZnS, thinking of them as "line compounds" where all samples of the same nominal composition will have the same properties. However, it has been known[157, 158] from growing binary semiconductors that at least two different *AB* semiconductors can be produced (at a given temperature) depending on whether the growth is *A*-excess or *B*-excess (usually as vapor phase, where vapor

pressure adds an additional variable). These two different semiconductors, *AB* with *A*-excess or *AB* with *B*-excess, have distinctly different properties: one possibly being *n*-type and the other could be *p*-type. In complex systems, especially containing more elements, there are multiple, generally more than two, distinctly defined thermodynamic states.[32] For the discovery of new functional semiconductors, these multiple, distinct states of the same nominal composition expand the space of materials to investigate. In thermoelectrics for example, researchers have been examining thousands of nominally single phase materials for decades in search of, for example, *n*-type Zintl compounds with predicted high thermoelectric efficiency. The discovery of high performance *n*-type Mg_3Sb_2,[47] only recently, highlights the importance of examining all the distinct thermodynamic states by identifying the phase boundaries (Mg-excess as well as Sb-excess in this case) and that perhaps we have been looking at less than half the available new semiconductors that we could have in these past decades.

4.3 Thermoelectric semiconductor

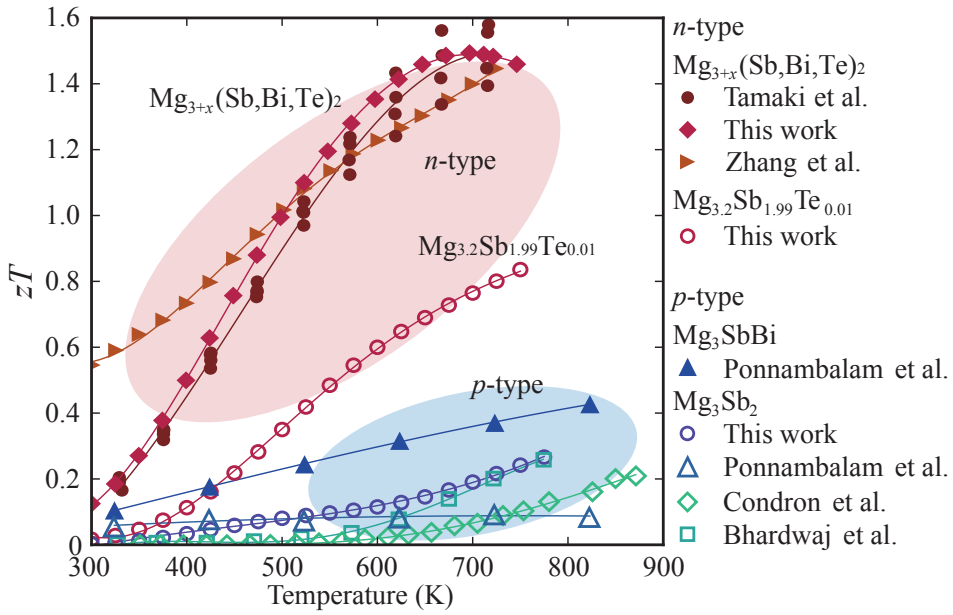

Figure 4.1: Comparison of zT from *n*- and *p*-type Mg_3Sb_2-based compounds, showing the superior properties of *n*-type materials. The given compositions are nominal compositions. The zT curve from Zhang *et al.*[48] was scaled using the measured heat capacity rather than the Dulong-Petit value used in the original report.

Thermoelectric devices can directly convert waste heat into useful electricity, attracting considerable attention as a means to harvest the energy that is currently

lost by dissipation. The efficiency of a thermoelectric device is largely dependent on the figure-of-merit of the thermoelectric materials, which is $zT = \frac{\alpha^2\sigma}{\kappa}T$ where α is the Seebeck coefficient, σ is the electrical conductivity, κ is the total thermal conductivity, and T is the absolute temperature.[22, 232] Typical $zT < 1$ values of known materials are insufficient for many proposed applications, making it of interest to explore new materials with beneficial characteristics.

Zintl compounds[89] are a promising class of materials where good thermoelectrics continue to be discovered. A covalently bonded anionic framework forms the basis of the crystal structure in Zintl compounds,[87, 115] while the electropositive cations donate electrons satisfying the valence requirement to make it semiconducting. With the net count of the valence electrons being zero,[85] the undoped Zintl compound is, in principle, a semiconductor that can be doped to have an optimum carrier concentration for thermoelectrics. Several Zintl compounds show excellent zT at high temperatures: $Yb_{14}MnSb_{11}$,[106] $Ca_9Zn_{4+x}Sb_9$,[32] Sr_3GaSb_3,[101] $Ca_5Al_2Sb_6$,[29] and $YbCd_2Sb_2$,[112] just to name a few.

Almost all Zintl thermoelectric materials are found to be *p*-type, while computed electronic structures suggest that some of these persistently *p*-type materials would also make good, or even better, *n*-type materials because of the band structure.[50, 233] For instance, a high throughput computational search (using DFT and Boltz-TraP) predicted LiZnSb to be an excellent *n*-type thermoelectric, expected to be more than 10 times better than its *p*-type performance which reached $zT \sim 0.1$.[234, 235] This persistent *p*-type behavior is also observed in the AZn_2Sb_2 (A= Ca, Yb, Eu, Sr) system (member of the so-called 1-2-2 phases), where the *A* cation vacancy acts as an "electron killer",[77] preventing *n*-type samples to form. Studies on this system have revealed how a prudent choice of the *A* atom could impact the formation energy of the electron killer defects, suggesting that selecting the appropriate *A* cation is key to overcoming the persistent *p*-type behavior.

Mg_3Sb_2 is a special case of the 1-2-2 family (Mg occupies both the *A* and Zn site in AZn_2Sb_2) where, after a long history since it's first discovery in 1933,[82] the compound has recently been synthesized as *n*-type by Tamaki *et al.* using excess Mg.[47] This achievement is quite remarkable considering how often this structure type has been considered for thermoelectrics. Previous studies have only found good *p*-type thermoelectrics, starting from AZn_2Sb_2,[111] and then, including Cd for Zn[112] and Bi for Sb,[81] $zT \sim 1$ has been achieved. Nearly all previous attempts with Mg_3Sb_2 [162, 163], including Mn, Zn, Cd, Na substitution on the Mg

site[236–239] and Pb, Bi substitution on the Sb site[240–244], have all produced *p*-type materials. A Mn substituted single crystal was found to be *n*-type, but with low carrier concentration (10^{18} cm^{-3}).

Outstanding *n*-type Mg_3Sb_2-based thermoelectrics had been anticipated based on the conduction band complexity that includes a high degeneracy Fermi surface with 6 carrier pockets.[47, 245] High valley degeneracy is known to lead to high thermoelectric quality factor and is found in most good thermoelectric materials such as Bi_2Te_3,[42, 246] PbTe,[40, 247] Mg_2(Si,Sn),[44] $CoSb_3$ skutterudites,[45] and some Half Heusler thermoelectrics.[46]

Tamaki *et al.* reported *n*-type $Mg_{3.2}Sb1.5Bi_{0.49}Te_{0.01}$ with zT of 1.5 at 715 K followed by similar results by Zhang *et al.* and Shuai *et al.*[47, 48, 248] Fig. 4.1 compares the experimental zT of *p*- and *n*-type Mg_3Sb_2-based compounds including newly synthesized samples that successfully reproduce the optimum *n*-type composition. A clear contrast in the maximum zT is seen, and which is mainly due to the advantage of having larger valley degeneracy (N_v) in the conduction band (N_v = 6) than in the valence band (N_v = 1). (See Fig. 4.2 and 4.3)

Due to the substantial excess of Mg in nominal composition needed ($Mg_{3.2}$(Sb,Bi,Te)$_2$) to make the material *n*-type, it has been previously proposed that Mg interstitials are responsible for the *n*-type carriers.[47] Indeed, defect calculations showed that the Mg interstitial defect energy was sufficiently low to enable $Mg_{3+x}Sb_2$ to become somewhat *n*-type. Here we find, however, that Mg interstitials are not essential in obtaining *n*-type Mg_3Sb_2 compounds. In the optimally doped composition, Mg interstitials are eventually so far outnumbered by vacancies that the equilibrium composition is actually Mg-deficient, $x < 0$ in Mg_{3+x}(Sb,Bi,Te)$_2$, rather than Mg-excess. This result underscores the significance of the cation vacancies and essential experimental procedures to access the thermodynamic state where vacancy formation is most suppressed.

4.4 Defect Chemistry in Mg_3Sb_2

In many previous experimental attempts, Mg_3Sb_2 would largely remain *p*-type despite the addition of extra Mg (ref. [163, 240]). Even doping with a substituent that would normally provide *n*-type carriers has until recently not been successful. Such persistent behavior is characteristic of an intrinsic "killer" defect [249] present even in the undoped system that prevents or pins the Fermi level (E_F) from moving into or near to the conduction band (*i.e.* limits of concentration of free electrons).

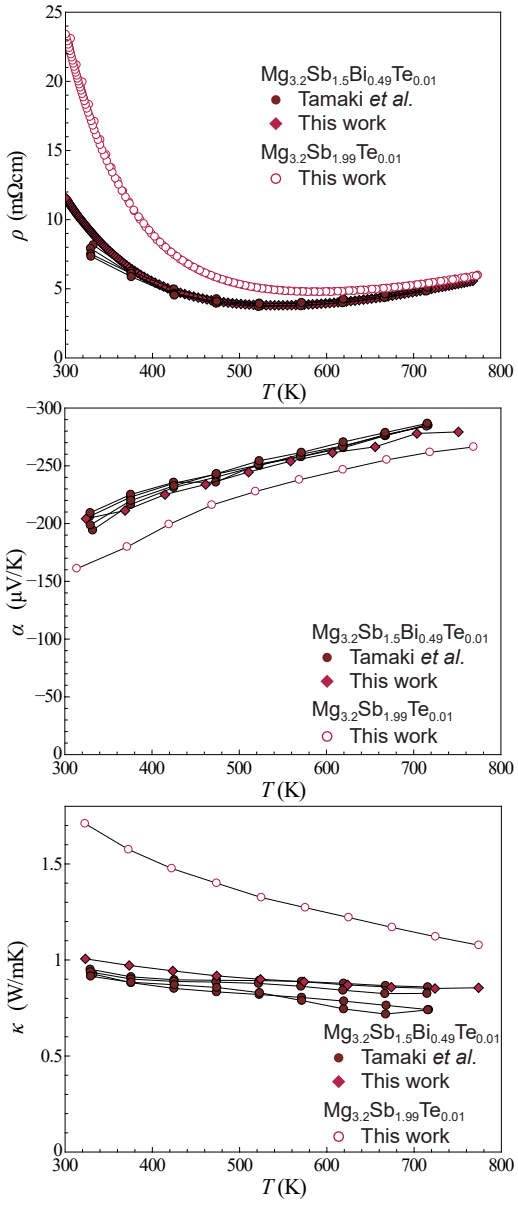

Figure 4.2: Transport properties of $Mg_{3.2}Sb_{1.5}Bi_{0.49}Te_{0.01}$ and $Mg_{3.2}Sb_{1.99}Te_{0.01}$ synthesized in this work with the data of $Mg_{3.2}Sb_{1.5}Bi_{0.49}Te_{0.01}$ reported in ref [47]. Thermal conductivity of $Mg_{3.2}Sb_{1.5}Bi_{0.49}Te_{0.01}$ and $Mg_{3.2}Sb_{1.99}Te_{0.01}$ are calculated with the experimentally determined heat capacity reported in ref [47, 48]. Reproduced $Mg_{3.2}Sb_{1.5}Bi_{0.49}Te_{0.01}$ shows almost identical properties to the reported values of $Mg_{3.2}Sb_{1.5}Bi_{0.49}Te_{0.01}$.

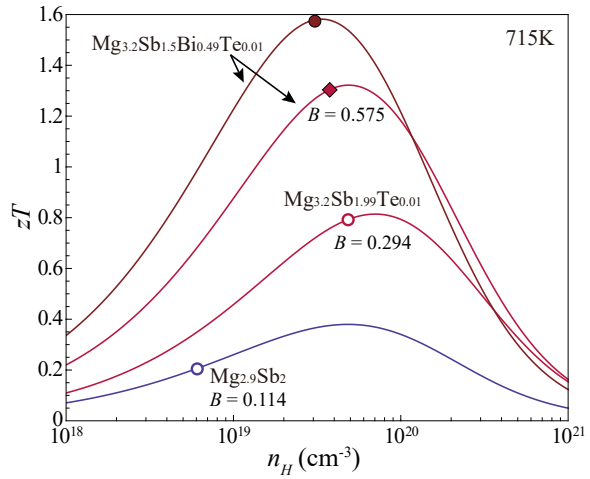

Figure 4.3: The predicted zT of Mg_3Sb_2-based materials as a function of Hall carrier concentration. Solid curves are obtained from experimental data (symbols) based on single-parabolic band model. At 715 K, it is safe to assume the acoustic phonon scattering. The n-type Mg_3Sb_2 is predicted to be a superior thermoelectric material to p-type due to the multiband effect. 0.2 at.% of Te doping realizes the almost optimum doping level for all of the n-type samples. B is a dimensionless material quality factor, which shows the potential of the material to be thermoelectric. Mg_3Sb_2 can possess about 2.5 times higher B just by being n-type conduction and it becomes even higher by alloying.

The p-type pinning behavior can be readily explained by the presence of a low-energy electron acceptor defect V_{Mg}^{2-} ($Mg_{Mg} \rightarrow V_{Mg}^{2-} + 2h^+$) producing excess holes h^+ (or absorbing excess electrons). The formation energy of negatively charged defects such as V_{Mg}^{2-} becomes lower with increasing Fermi level (which indicates having more excess electrons in the system) because it absorbs excess electrons. This makes the slope of the formation energy for V_{Mg}^{2-} vs. E_F in Fig 4.4a negative (the slope is positive for donor defects). Once a defect formation energy is no longer positive, it will spontaneously form even at T = 0 K. Forming V_{Mg}^{2-} produces holes and reduces E_F, enabling the system to reach an equilibrium E_F and vacancy concentration. Alternatively, if one tries to increase E_F (by adding impurity donor dopants for example) to reach the conduction band (*i.e.* move towards n-type behavior) the formation of Mg vacancies will become more favorable and E_F will change less than anticipated. If an intrinsic acceptor defect energy reduces to zero by increasing E_F, then E_F can never be greater than this value as the intrinsic acceptor defects will always form reducing the E_F. In this way intrinsic acceptor defects can pin the E_F of a material to always be p-type (similarly, intrinsic donor defects can pin the E_F of a material to always be n-type). For example in Mg_3Sb_2, even when we try

to introduce a foreign n-type dopant, the E_F can never go closer to the conduction band than the pinning E_F of the cation vacancies (Fig. 4.4a).

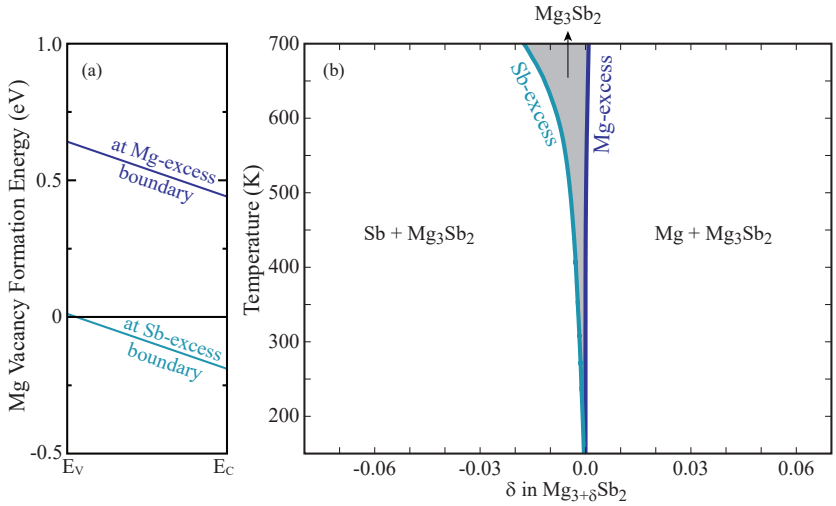

Figure 4.4: The Mg-Sb phase diagram near Mg_3Sb_2 and its influence on the dominant defects. (a) The Mg vacancy formation energy in Mg_3Sb_2 as a function of Fermi level (E_F) showing the pinning of E_F (when formation energy is zero) at the valence band edge (E_V) for Sb-excess Mg_3Sb_2. Mg-excess Mg_3Sb_2 has high vacancy formation energy even for E_F inside the conduction band (above E_C). (b) The calculated Mg-Sb phase diagram near Mg_3Sb_2. The phase boundary on the left (light blue) is the Sb-excess solubility limit determined by the chemical potential of elemental Sb and the boundary on the right side (dark blue) is the Mg-excess limit determined by the chemical potential of elemental Mg.

In general, it is reasonable to suspect cation vacancies (Mg vacancies in this case) as the majority defect in Zintl compounds even before resorting to defect energy calculations. Cations have much smaller ionic radii than anions, making cation vacancies the likely species for defect formation. Although interstials are also common for small cations such as Mg^{2+}, the persistent p-type behavior observed in Mg_3Sb_2 suggests that the acceptor Mg vacancies ($Mg_{Mg} \rightarrow V_{Mg}^{2-} + 2h^+$) rather than the electron donor Mg interstitials ($Mg_{Mg} \rightarrow Mg_i^{2+} + 2e^-$) explain the behavior. Persistent p-type behavior has been long observed and recently explained in AZn_2Sb_2 (A = Ca, Yb, Eu, Sr), which has the same crystal structure as Mg_3Sb_2. Formation of a sufficient number of stable A site vacancies actually leads to their suitability as p-type thermoelectric semiconductors without impurity p-type doping.[77, 250]

The concentration of intrinsic defects such as V_{Mg}^{2-} and its temperature dependency can be seen in the equilibrium phase diagram (Fig. 4.4b). Like most valence balanced semiconductors (Zintl compounds), Mg_3Sb_2 could be described as a line

compound because the range of single phase compositions is very narrow. However, because defects provide entropy, no real compound is exactly a line compound. In Fig 4.4b the narrow compositional range for Mg_3Sb_2 is expanded where the significant concentration of the V_{Mg}^{2-} vacancies is manifested in the extension of the Mg_3Sb_2 single-phase composition range at the Sb-excess side of the single-phase region. The extension of the phase width at the Mg-excess side is much less due to the higher defect energy of Mg-interstitials. For a nominal composition (*i.e.* overall starting composition) that is Mg-excess (700 K), *e.g.* $Mg_{3.2}Sb_2$, the actual composition of the matrix-phase (Mg_3Sb_2 phase) would be fixed at the Mg-excess side phase boundary, yielding an intrinsic composition of $Mg_{3.0009}Sb_2$. We note that the large Mg solubility in Mg_3Sb_2 (up to $Mg_{3.2}Sb_2$) shown in a previous binary phase diagram[251] is not consistent with our experimental (see Fig. 4.5 and table 4.1) or computational results; the original report on which the phase diagram is based showed the Mg solubility line as uncertain.[252]

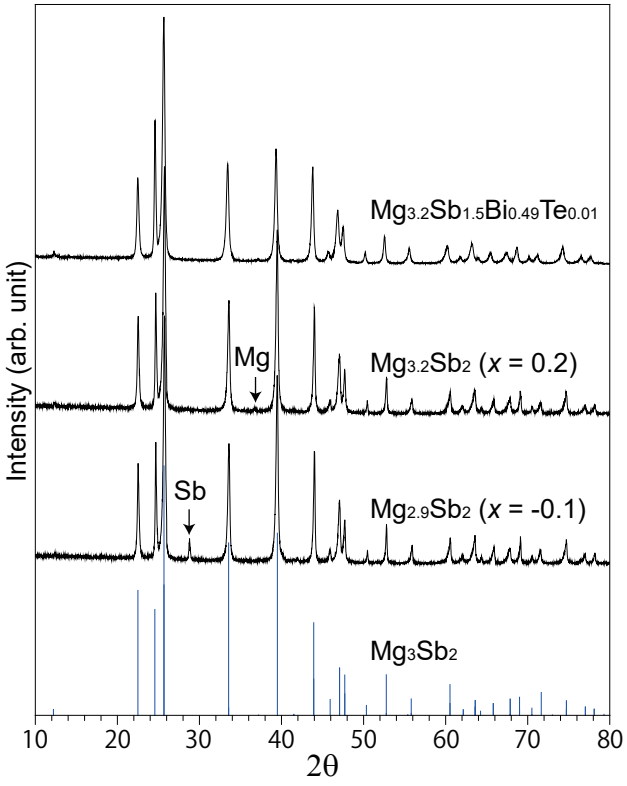

Figure 4.5: XRD patterns of Mg_3Sb_2-based compounds. The elemental Mg and Sb peaks are clearly observed in $Mg_{3+x}Sb_2$ samples with $x = 0.2$ and -0.1, respectively. Therefore, the range of Mg content (-0.1 < x < 0.2) explored in this study is sufficiently large to investigate the two distinct thermodynamic states: Mg-excess and Sb-excess.

	$Mg_{3.2}Sb_2$	$Mg_{2.9}Sb_2$
EDS	$Mg_{2.93\pm0.06}Sb_{2.06\pm0.04}$	$Mg_{2.92\pm0.06}Sb_{2.08\pm0.04}$
WDS	$Mg_{3.070\pm0.06}Sb_{1.930\pm0.04}$	$Mg_{3.049\pm0.06}Sb_{1.951\pm0.04}$

Table 4.1: Elemental analysis by Energy dispersive spectroscopy (EDS) and wave dispersive spectroscopy (WDS) implies that the difference in the actual Mg content of Mg-excess and Sb-excess samples be drastically smaller than reported Mg solubility in ref [251], showing over 9% of Mg solubility in Mg_3Sb_2. Due to the finite detection area, the small difference in Mg contents detected in EDS and WDS could simply arise from the elemental Mg which exists in the $Mg_{3.2}Sb_2$ as shown in Fig. 4.5. ± shows the typical accuracy (2%) of the measurement.

These phase boundaries are determined by atomic chemical potentials. The Mg-excess boundary is defined by the Mg-chemical potential in the Mg_3Sb_2 phase being the same as elemental Mg, while the Sb-excess boundary is defined by the Sb-chemical potential in the Mg_3Sb_2 phase being the same as elemental Sb. The large chemical potential difference between Mg-excess and Sb-excess in Mg_3Sb_2 - across a narrow phase width - leads to a step function change in the thermodynamic potentials (manifested in Fig. 4.6). For practical purposes, this composition range is so narrow that real samples are better thermodynamically defined when their nominal compositions are safely on one side or the other with the desired matrix phase in equilibrium with a small amount ($< \sim 2\%$) of impurity phase, otherwise the sample is likely to have small but significant compositional variations and result in transport properties indicative of inhomogeneous samples. Therefore, reliable samples of Mg_3Sb_2 should be in one of two distinct thermodynamic states of accessible samples: Mg-excess and Sb-excess.

The difference in atomic chemical potentials for Mg-excess and Sb-excess Mg_3Sb_2 leads to the distinctly different defect formation energies for V_{Mg}^{2-}. When the formation of a defect involves the decrease (increase) in the number of atoms, the chemical potential of that atom adds to (subtracts from) the defect formation energy (see Methods); the added (subtracted) chemical potential of that atom is identical to that of the other coexisting phase(s) in equilibrium. In Mg-excess Mg_3Sb_2, having the Mg-chemical potential of elemental Mg leads to the distinctly higher defect formation energy for V_{Mg}^{2-} (by 0.63 eV) than for V_{Mg}^{2-} in Sb-excess Mg_3Sb_2. In this sense, Mg-excess and Sb-excess Mg_3Sb_2 are thermodynamically different "states". Thus an effective way to suppress the formation of V_{Mg}^{2-} killer defects is to maintain the Mg_3Sb_2 in the Mg-excess state. Thermodynamically, it is much harder to accommodate Mg vacancies in a system with excess Mg - according to

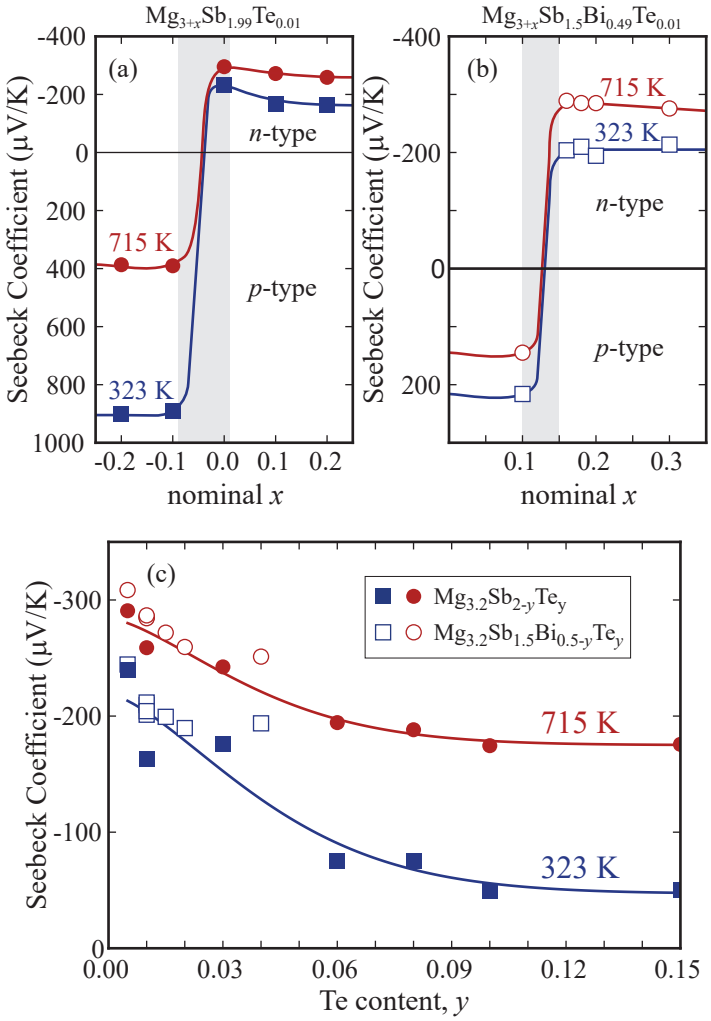

Figure 4.6: Seebeck coefficient dependence on nominal composition. (a) The step change of Seebeck coefficient with increasing nominal Mg content in $Mg_{3+x}Sb_{1.99}Te_{0.01}$ (synthesized using Mg-slug) indicates the abrupt transition in thermodynamic state from Sb-excess to Mg-excess. (b) The step change of Seebeck coefficient with increasing nominal Mg content in $Mg_{3+x}Sb_{1.5}Bi_{0.49}Te_{0.01}$ (synthesized using Mg-powder). (c) The continuous decrease in the thermopower (|S|) up to high Te content for the Mg-excess compositions as expected from an electron donor dopant. Lines are guides for the eye.

Le Ch*â*telier's principle - and thus a sample nominally Mg-rich would promote filling Mg vacancies. Having a positive formation energy of V_{Mg}^{2-} at the conduction band edge (E_C in Fig 4.4a) allows Mg-excess Mg_3Sb_2 to become *n*-type, whereas in Sb-excess Mg_3Sb_2, the negative V_{Mg}^{2-} formation energy throughout the band gap will always make it *p*-type. This difference also determines whether an extrinsic (impurity) *n*-type dopant can actually make Mg_3Sb_2 *n*-type, as we explain in the following section.

4.5 Extrinsic doping with Te in $Mg_3Sb_{2-y}Te_y$

The high concentration ($\sim 10^{20}/\mathrm{cm}^3$) of excess electrons needed to make a good thermoelectric is typically supplied by extrinsic or impurity dopants such as Te atoms (with 6 valence electrons) replacing a Sb (with only 5 valence electrons). These electrons in the conduction band are accounted for by increasing E_F toward the conduction band edge (E_C).

With Te-doping, E_F can be moved higher in $Mg_3Sb_{2-y}Te_y$ but the effect may be almost entirely compensated by the formation of other defects, most notably V_{Mg}^{2-} killer defects. To calculate these contributing effects (at the typical processing temperature of 700K) we use standard DFT methods described previously.[47] The important low-energy defects (Fig.4.7(a)-(c)) that determine E_F are Mg vacancies on both Mg sites ($V_{\mathrm{Mg(1)}}^{2-}$, $V_{\mathrm{Mg(2)}}^{2-}$), Te substitution on the Sb site ($\mathrm{Te}_{\mathrm{Sb}}^{1+}$), Mg interstitials ($\mathrm{Mg}_i^{2+}$), and Sb on Mg(1) anti-site defects ($\mathrm{Sb}_{\mathrm{Mg(1)}}^{1+}$). For Sb-excess $Mg_3Sb_{2-y}Te_y$, E_F is pinned (Fig.4.7b), keeping the material *p*-type up to the solubility limit of Te (0.5 at.% or $y \approx 0.025$. See Fig.4.8b).

The dramatic increase in V_{Mg}^{2-} defect energy going from Sb-excess to Mg-excess due to the step change in Mg-chemical potential enables a step change in *n*-type dopability. Once the vacancies are suppressed, gradually increasing the Te concentration gradually increases the *n*-type carrier concentration (Fig4.6c and 4.9) and ultimately good *n*-type thermoelectric properties of $Mg_3Sb_{2-y}Te_y$ with Mg-excess (Fig.4.1). The predicted *n*-type carrier concentration (Fig. 4.9) is in good agreement with experimental measurements from Te-doping, showing a small reduction in doping effectiveness due to compensating defects.[148]

4.6 Role of interstitial Mg

The requirement of excess Mg to produce *n*-type Mg_3Sb_2 has led to the suspicion that Mg_i^{2+} interstitials are perhaps responsible. Unlike other 1-2-2 compounds examined previously, Mg_3Sb_2 will accommodate a small extent of excess of Mg and

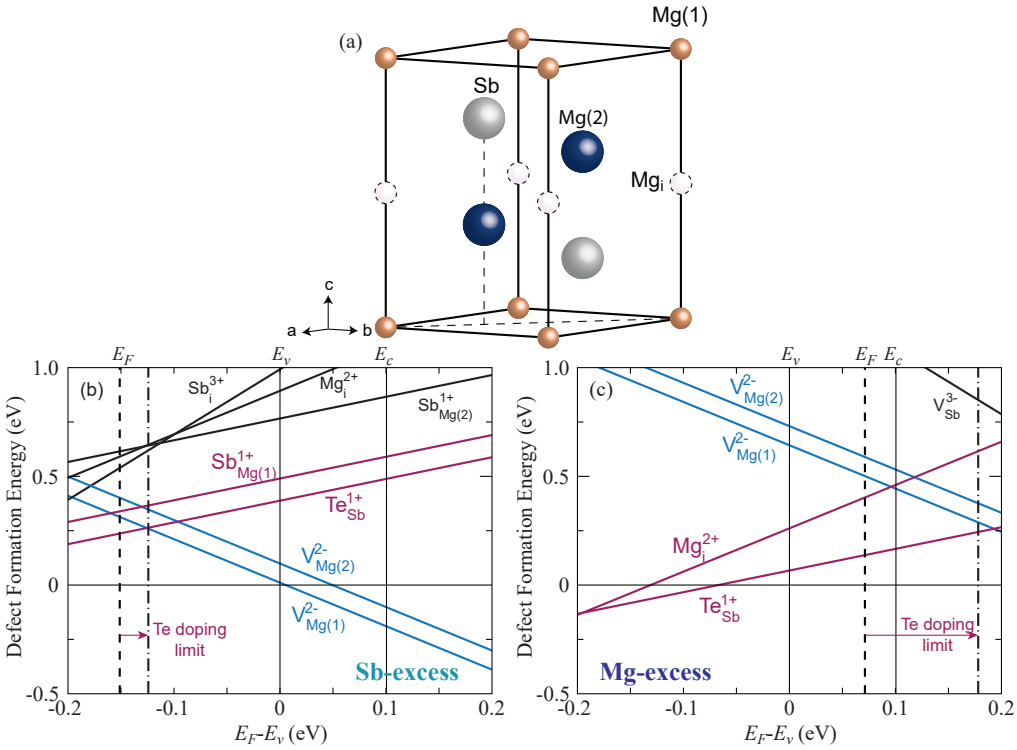

Figure 4.7: Defect chemistry in the Te-doped Mg_3Sb_2 system. (a) The crystal structure of Mg_3Sb_2 indicating atomic and interstitial positions. (b) Defect formation energy for Sb-excess Mg_3Sb_2 showing the Fermi level at 700 K (E_F) in the valence band ($E_F < E_V$) even with the addition of Te donor dopants. (c) Defect formation energy for Mg-excess Mg_3Sb_2. The undoped Fermi level (E_F) at 700 K (dashed line) moving deep into the conduction band ($E_C < E_F$) at the maximum Te-doping limit ($\approx$ 0.7 at.%) (dash-dotted line) shows the extrinsic n-type doping capability for Mg-excess Mg_3Sb_2. The defect energies were calculated by considering the equilibria of three phases (Mg_3Sb_2-Sb-MgTe for (b); Mg_3Sb_2-Mg-MgTe for (c). See Fig 4.8a.)

become slightly n-type; however, at the high n-type doping levels needed for high zT the concentration of Mg_i^{2+}, interstitials becomes insignificant and less than the concentration of V_{Mg}^{2-} vacancies as shown in Fig. 4.9.

The ternary Mg-Sb-Te phase diagram (700 K) in the vicinity of the Mg_3Sb_2 phase (Fig.4.8b-c) illustrates this point. The red-dashed line in Fig.4.8 delineates the compositions when acceptor and donor defects exactly charge-balance, separating compositions that give n- and p-type behavior. The gold-dashed line delineates the stoichiometric composition ($\delta = 0$) in $Mg_{3+\delta}Sb_{2-y}Te_y$, separating $\delta < 0$ compositions from $\delta > 0$ compositions. To avoid confusion, here we explicitly distinguish $Mg_{3+\delta}Sb_{2-y}Te_y$, where "$\delta$" refers to the actual composition of the matrix phase from

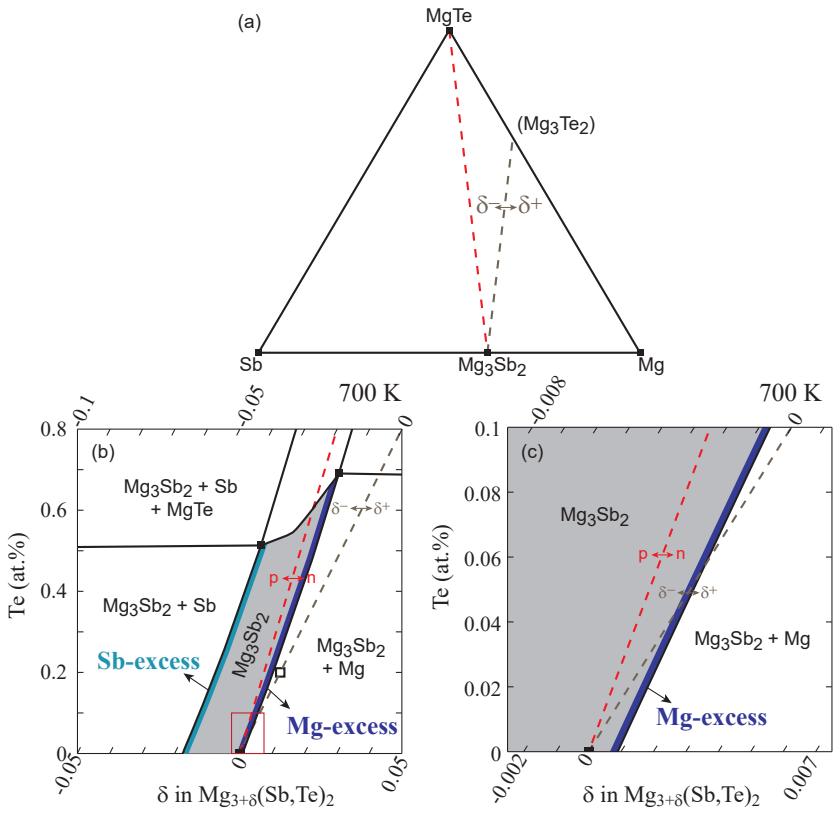

Figure 4.8: The ternary phase diagram of Mg-Sb-Te (a) The ternary diagram showing the position of $\delta = 0$ in $Mg_{3+\delta}(Sb,Te)_2$ (gold dashed line) and the line that distinguishes *p*- and *n*-type materials in the Mg_3Sb_2 single phase region (red dashed line). (b,c) Successively enlarged sections of the 700 K ternary phase diagram near the Mg_3Sb_2 single-phase region. The Sb-excess Mg_3Sb_2 phase boundary (light blue) always remains *p*-type and deficient in Mg ($\delta < 0$) while the Mg-excess Mg_3Sb_2 phase boundary (dark blue) is *n*-type even though it also is deficient in Mg ($\delta < 0$) when sufficiently doped to make a good thermoelectric (0.2 at.% of Te). The open square on the $\delta = 0$ line denotes the composition $Mg_3Sb_{1.99}Te_{0.01}$.

$Mg_{3+x}Sb_{2-y}Te_y$, where "x" is for a nominal composition. The actual composition of Sb-excess $Mg_{3+\delta}Sb_{2-y}Te_y$ shown as the light blue line in Fig.4.8b (Sb-solubility limit) is always $\delta < 0$ and always *p*-type. Mg-excess $Mg_{3+\delta}Sb_{2-y}Te_y$ shown as the dark blue line (Mg-solubility limit), is always *n*-type but crosses from $\delta > 0$ to $\delta < 0$ as the Te content increases (Fig.4.8c). Because this $\delta = 0$ line crosses the Mg-excess Mg_3Sb_2 phase boundary at Te $\approx 0.06\%$ ($Mg_3Sb_{1.997}Te_{0.003}$), which is much lower than the Te-doping concentration needed (around 0.2 at.% of Te) for high zT in Mg_3Sb_2 thermoelectric materials (similarly expected for $Mg_3(Sb,Bi)_2$), the optimum composition samples are always Mg deficient ($\delta < 0$) with Mg vacancies outnumbering interstitials.

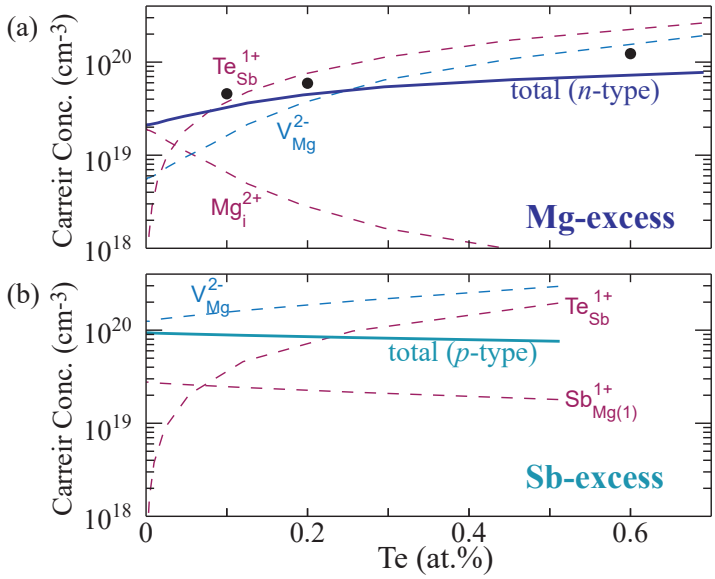

Figure 4.9: Calculated net charge carrier concentration (solid lines) and the contribution from individual defects (dashed lines) in Mg_3Sb_2 at 700 K with increasing Te content. (a) Mg-excess Mg_3Sb_2. The *n*-type carrier concentration follows the Te content (Te_{Sb}^{1+}) with some reduction due to Mg-vacancies (V_{Mg}^{2-}) at the doping concentration needed to make an efficient thermoelectric (0.2 at.% of Te). (b) Sb-excess Mg_3Sb_2. The net carrier concentration is always *p*-type despite the addition of Te donor dopants because of the excessive compensation from Mg vacancies. Data points (black circles) are converted from Hall measurements (see Methods) on samples with nominal compositions of $Mg_{3.2}Sb_{2-y}Te_y$ where y = 0.005, 0.01, and 0.03 in increasing order of Te content.

4.7 Phase Boundary Mapping to explore all equilibrium states of new phases

Mg_3Sb_2 demonstrates the dramatic difference in electronic properties from two types of samples with a matrix phase composition that is essentially the same. Only Mg-excess Mg_3Sb_2-based compounds can make efficient *n*-type thermoelectrics. The nominal composition at which the Mg-excess phase boundary is reached turns out to heavily depend on the synthesis route taken. For example, oxidation during preparation or pressing, oxides in any of the starting elements or even SiO_2 or Al_2O_3 reaction containers, easily becomes a source of MgO which effectively removes Mg from the Mg-Sb equilibria. With relatively high vapor pressure and reactivity, Mg loss can also happen from vaporization during hot-pressing, SPS, or annealing.

Because some Mg loss always exists, the only way to ensure that the Mg-excess phase boundary composition is reached is by detecting Mg impurities in the final material to be measured. Even for reproducible routes of syntheses, there will be

a critical nominal composition where the *p*-to-*n* transition happens that may not be at a nominal Mg:Sb ratio of 3:2 and also quite different depending on synthesis conditions (compare the threshold composition within the light gray regime in Fig.4.6a and b made by Mg powder or slugs). Only by detecting a small amount of elemental Mg or Sb can one be sure which chemical potential defines the properties of the matrix phase.

In general, we call this method phase boundary mapping, which is to purposely make materials in equilibrium with small amounts of impurity phases that exactly define the chemical potentials.[32] Since most semiconductors are valence balanced (*e.g.* Zintl compounds[89]), they are typically considered line compounds with narrow phase widths particularly regarding the cation to anion ratio. Therefore, practical samples will generally tend to be on one side or the other, making observation of equilibrium impurity phases the best way to define the thermodynamic state. Compound semiconductors will have at least two (most likely more than two) distinct thermodynamic states with distinctly different dopability and transport properties. To explore all synthetically accessible thermodynamic states of the same new semiconductor one should map all the thermodynamic phase boundaries and continue to change composition (as we added Mg in Mg_3Sb_2) until the equilibrium impurity phase changes (as excess Mg was observed instead of Sb). When vacancies are the dominant defects excess metal should promote *n*-type dopability while excess non-metal should promote *p*-type dopability.[158]

A systematic implementation of the phase boundary mapping procedure will lead to a better understanding of the doping capability of new semiconductors for a variety of applications. In thermoelectrics, related approaches have been used to ascertain that cation vacancies are killer defects that lead to persistent *p*-type materials in $Ca_9Zn_{4+x}Sb_9$,[31] $YCuTe_2$,[253] Cu_2Se,[254] ZnSb,[255] Zn_4Sb_3,[94] $YbZn_2Sb_2$.[250] We find, in general, several recent cases where significant findings result from a systematic investigation of the phase boundaries: filling capabilities in Skutterudites[256–258] and finding low-defect photovoltaic compounds.[259–261] All these cases highlight the general significance of phase boundary mapping.

Chapter 5

Achieving $zT > 1$ in inexpensive Zintl phase $Ca_9Zn_{4+x}Sb_9$ by phase boundary mapping

This chapter contains contents reproduced with permission from *Advanced Functional Materials*, DOI: 10.1002/adfm.201606361.

5.1 Summary of research

Complex multinary compounds (ternary, quaternary, and higher) offer countless opportunities for discovering new semiconductors for applications such as photovoltaics and thermoelectrics. However, controlling doping has been a major challenge in complex semiconductors as there are many possibilities for charged intrinsic defects (*e.g.* vacancies, interstitials, anti-site defects) whose energy depends on competing impurity phases. Even in compounds with no apparent deviation from a stoichiometric nominal composition, such defects commonly lead to free carrier concentrations in excess of $10^{20}/cm^3$. Nevertheless, by slightly altering the nominal composition, these defect concentrations can be tuned with small variation of the chemical potentials (composition) of each element. While the variation of chemical composition is undetectable, we show the changes can be inferred by mapping (in nominal composition space) the boundaries where different competing impurity phases form. In the inexpensive Zintl compound $Ca_9Zn_{4+x}Sb_9$, the carrier concentrations can be finely tuned within three different three-phase regions by altering the nominal composition (x = 0.2 - 0.8), enabling the doubling of thermoelectric performance (zT). Because of the low thermal conductivity, the zT can reach as high as 1.1 at 875 K, which is one of the highest among the earth abundant p-type thermoelectrics with no ion conducting.

5.2 Introduction

While today most semiconductor applications use simple elemental (*e.g.* Si) or binary (*e.g.* GaN) semiconductors, many new complex semiconductors are being discovered and developed containing three or more elements. This greatly increases the possibilities for finding new functionalities (such as photovoltaics, solid-state lighting and thermoelectrics) and that utilize earth abundant elements. Solid-state thermoelectric generators, for example, are reliable, scalable, and robust devices

to convert waste heat into useful energy, which have substantial potential in contributing to a sustainable solution for the world's growing energy needs. However, the cost of constituent elements in the current state of the art materials (*i.e.* PbTe) can limit widespread use of thermoelectric materials. To overcome this problem, new materials consisting of earth abundant and environmentally friendly materials are essential. Achieving a competitive efficiency for such thermoelectric materials, determined by the thermoelectric figure of merit, ($zT = \alpha^2 T/\kappa\rho$, of approximately one is the critical challenge to reach cost targets.[232]

A good thermoelectric material must strike a balance between a large Seebeck coefficient (α), low electrical resistivity (ρ), and low total thermal conductivity (κ). The total thermal conductivity is a combination of electronic thermal conductivity (κ_e) and lattice thermal conductivity (κ_L).[22] Except for κ_L, all transport coefficients are interdependent *via* the majority carrier concentration, often measured by the Hall effect (n_H). Normally, crystalline materials have a higher electrical mobility (μ_H), leading to a higher electrical conductivity, ($\sigma = 1/\rho = n_H e \mu_H$ where e is the electronic charge), than amorphous materials. On the other hand, amorphous materials have shorter phonon mean free paths, and display lower κ_L. Therefore, an ideal thermoelectric material should have a glass-like heat conduction of phonons and crystal-like electrical conduction of charge carriers, referred to as the "phonon-glass electron-crystal" (PGEC) concept, first introduced by Slack.[262]

Complex Zintl phases represent a large class of compounds in which many new thermoelectric materials have been found, thanks to their versatile chemistry and inherently low thermal conductivity like glasses.[28, 47, 97, 102, 112, 146, 248, 257, 263, 264] Zintl compounds are made up of electropositive cations (alkali, alkaline-earth or rare earth metals) that donate their valence electrons to anions, which in turn form covalently bonded anionic structures to satisfy the valence requirement.[83, 85, 265] One important aspect of these compounds is their inherently low lattice thermal conductivity due to their complex crystal structures.[29, 53, 89, 115]

$A_9M_{4+x}Pn_9$ (A = Yb, Eu, Ca, Sr; M = Mn, Zn, Cd; Pn = Sb, Bi), often referred to as the 9-4-9 system, are Zintl phases recently identified with promising thermoelectric performance.[108, 117, 118, 143, 144, 266–268] The crystal structure was originally reported in 1970s, but the existence of partially occupied interstitial sites, whose occupancy is indicated by x in the formula, was not recognized until the work of Bobev *et al.* in 2004 (Fig. 5.1a).[144] These partially occupied sites enable carrier concentration tuning and also contribute to a lower lattice thermal conductivity by

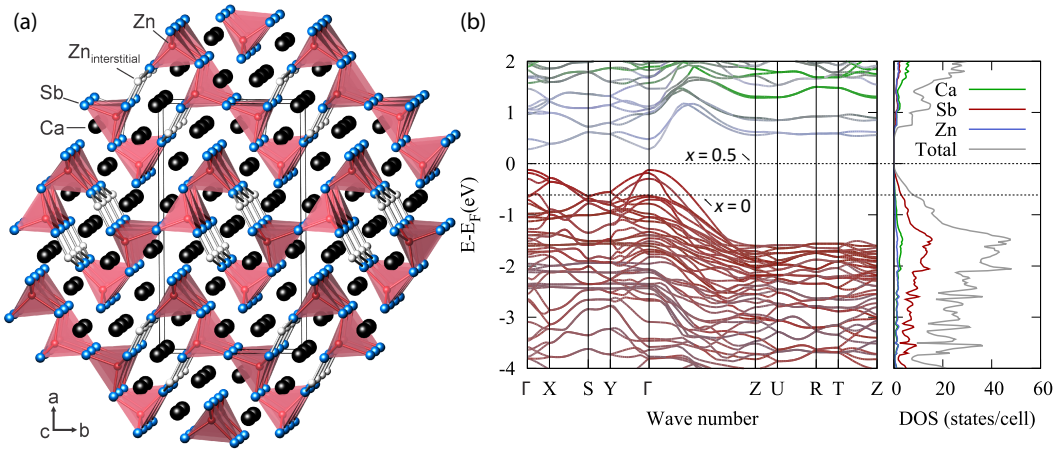

Figure 5.1: (a) The crystal structure of $A_9M_{4+x}Pn_9$ where A: Ca, M: Zn, and Pn: Sb showing ribbon-like chains of $[Zn_4Sb_9]^{19-}$ along the c-axis. Interstitial Zn atoms are located between the chains (when present). (b) Electronic band structure and density of states of $Ca_9Zn_{4+x}Sb_9$. Two black dashed lines indicate Fermi levels of the charge balanced $Ca_9Zn_{4.5}Sb_9$ composition (x = 0.5) and the structure with no interstitial Zn atom ($Ca_9Zn_4Sb_9$; $x = 0$). The band structure is color coded according to the atomic character of the states, where gray indicates an equal contribution from all atom types.

adding more complexity and disorder in the structure. In the Yb-Mn-Sb system, $Yb_9Mn_{4+x}Sb_9$ easily forms with a nearly optimal carrier concentration, displaying a zT of around 0.7 at 950 K without doping. $Yb_9Zn_{4+x}Sb_9$ has even higher mobility than $Yb_9Mn_{4+x}Sb_9$ and so would have even higher zT if it could be optimally doped.[24, 30, 37, 41] The higher mobility is achieved through the reduction of the effective mass as shown in the study on solid solution $Yb_9Mn_{4.2-x}Zn_xSb_9$.[31] Although $Yb_9Zn_{4+x}Sb_9$ has a favourable high carrier mobility and low lattice thermal conductivity, its carrier density is much larger than the optimum value.[31]

In principle, the carrier density can be tuned by changing the composition with the total charge determined by the net valence.[89] The partially occupied M site in $A_9M_{4+x}Pn_9$ is seen as a convenient site for doping. In practice, however, even though all reported samples are p-type (the actual Zn contents clearly less than 4.5: See section 5.3), the allowed range of carrier concentration is very small (narrow phase width).[30, 31] The actual composition of $A_9M_{4+x}Pn_9$ phase, and thus the actual phase width in the crystalline material is difficult to conclusively measure.

Despite the complexity of multiple defect types and uncertain defect concentrations, the full range of thermodynamically accessible defects can be explored using phase

boundary mapping within an isothermal section of the Ca-Zn-Sb ternary phase diagram. Such an equilibrium phase diagram provides the synthesis conditions required to achieve the full range of thermodynamically possible intrinsic defect concentrations to achieve appropriate doping as shown in Yb-doped $CoSb_3$ skutterudites.[256] Demonstrating this principle, we successfully synthesized samples of $Ca_9Zn_{4+x}Sb_9$ having different *p*-type carrier concentrations depending on the phase-region of the nominal composition (x = 0.2, 0.3, 0.4, 0.5, 0.6, 0.7 and 0.8). Optimally doped $Ca_9Zn_{4+x}Sb_9$ containing inexpensive elements can now be produced with a high zT of 1.1 at 875 K, which is one of the highest values among inexpensive *p*-type thermoelectric without ion conducting.

5.3 Crystal and electronic structure

$Ca_9Zn_{4+x}Sb_9$ is a complex Zintl phase whose semiconducting electronic properties, defect chemistry and low lattice thermal conductivity can be explained by its crystal structure and valence electron counting. $Ca_9Zn_{4+x}Sb_9$, $Yb_9Mn_{4+x}Sb_9$, and $Yb_9Zn_{4+x}Sb_9$ have the same $A_9M_{4+x}Pn_9$ crystal structure shown in Fig. 5.1a.[117, 118, 143] The structure contains ribbon-like chains of corner shared tetrahedra $[M_4Sb_9]^{19-}$ (M: Zn, Mn) extending infinitely along the c direction. These "ribbons" are connected to one another by partially occupied "interstitial" M sites creating a quasi-two dimensional anionic structure. For $Ca_9Zn_{4+x}Sb_9$ with x = 0.5, 25% of the interstitial sites are occupied by Zn atoms, yielding a charge balanced composition of $Ca_9Zn_{4.5}Sb_9$ with the simple valence counting, $[Ca^{2+}]_9[Zn^{2+}]_{4.5}[Sb^{3-}]_9$. The valence balanced composition suggests a simple band gap may exist between anion and cation electronic states at this composition as found in many Zintl phases.[89, 147] With no interstitial Zn atoms (x = 0), the hypothetical compound $Ca_9Zn_4Sb_9$ is a *p*-type metal being one electron short of valence balance.[170] Having no disorder, the band structure of $Ca_9Zn_4Sb_9$, shown in Fig. 5.1b, can be readily calculated, and indeed shows the Fermi level deep in the valence band. The band structure for $Ca_9Zn_{4.5}Sb_9$, including the one additional electron per formula unit from the interstitial Zn atom, would yield (assuming rigid bands) a small band gap semiconductor by moving the Fermi level to the band gap (x = 0.5 in Fig. 5.1b). The calculated valence band is dominated by antimony *p*-states, as would be expected considering Sb as an anion even though the close electronegativity between Sb and Zn suggests significant covalent mixing of those states is possible. Zn-*d* states are well below the Fermi level and are fully occupied. (See Fig. 5.2) The calculated band gap (E_g) is direct (E_g = 0.35 eV).

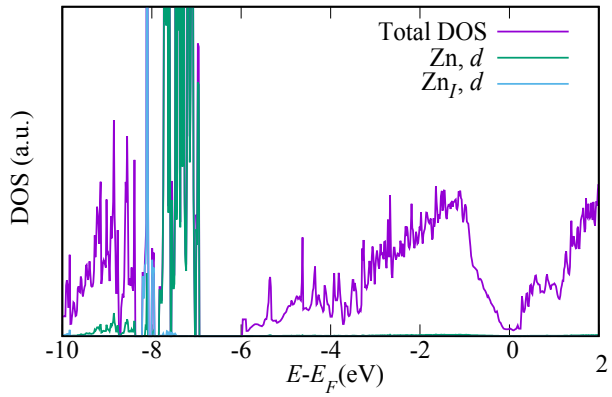

Figure 5.2: The calculated DOS plot of the relaxed $Ca_{18}Zn_9Sb_{18}$-cell, showing that the *d*-states of the interstitial Zn atom (Zn_I) is far below the Fermi level (about -7 eV). The green line is the sum of all *d*-character states of all 8 "non-interstitial" Zn atoms, and the blue line is the *d*-state of Zn_I.

5.4 Defects

From the above connection between interstitial concentration and Fermi level in the electronic band structure, we can explain why $Ca_9Zn_{4+x}Sb_9$ phase with x less than 0.5 should behave as a degenerate *p*-type semiconductor and, in theory, why the *p*-type carrier concentration decreases as its stoichiometry approaches $x = 0.5$. Specifically, one can investigate the hole concentration n [holes/formula unit] = $2\ \delta$, where δ is the number of missing Zn from the charge balanced composition, $Ca_9Zn_{4.5}Sb_9$. Thus, in principle, tuning the carrier concentration should simply be a matter of adjusting the amount of partially occupied interstitial Zn content of the actual sample composition, which can be referred to as $Ca_9Zn_{4.5-\delta}Sb_9$. To avoid confusion, we will henceforth explicitly distinguish $Ca_9Zn_{4+x}Sb_9$ using the nominal composition x (the overall starting composition for synthesis) from $Ca_9Zn_{4.5-\delta}Sb_9$, the actual sample composition of resulting sample using δ. While we will show that we have sufficient control over carrier concentration by changing the nominal amount of Zn, we do this without exact knowledge and precise control over δ.

The results of the direct compositional analysis is consistent with the composition $Ca_9Zn_{4.5-\delta}Sb_9$ with $\delta < 0.1$ but the precise determination of δ by these means is not possible. For example, EDS and WDS for the sample with nominal composition $Ca_9Zn_{4.3}Sb_9$ show a composition of the $Ca_9Zn_{4.5-\delta}Sb_9$ phase to be $Ca_{8.9\pm0.2}Zn_{4.4\pm0.1}Sb_{9.1\pm0.2}$ and $Ca_{9.3\pm0.2}Zn_{4.5\pm0.1}Sb_{8.7\pm0.2}$, where the typical accuracy is beyond the minute changes in the stoichiometry due to defects. The composition reported from XRD refinement of a single crystal ($Ca_9Zn_{4.478(8)}Sb_9$)

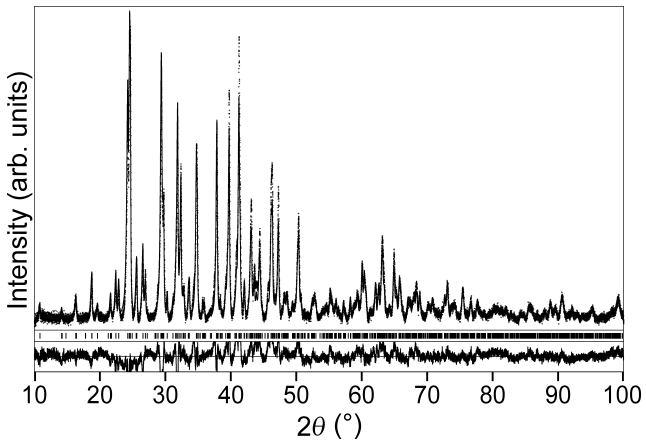

Figure 5.3: Rietveld fit of $Ca_9Zn_{4.3}Sb_9$ (Cu-$K_{\alpha 1}$ radiation). Ticks mark the calculated reflection positions of the target phase while the baseline corresponds to the residuals of a Rietveld refinement (R_i = 0.09, R_p = 0.20, R_{wp} = 0.20) based on the reported crystal structure. In the crystal structure of $Ca_9Zn_{4+x}Sb_9$ (space group: *Pbam*), there are five Ca (1×2b, 3×4g, 1×4h) and Sb (1×2d, 2×4g, 2×4h), and three Zn (2×4h, 1×4g) Wyckoff sites. Based on the reported single crystal data, apart from the Zn3 position at the 4g site, which is partially occupied (23.9(4)%), all other sites are fully occupied. We identified the partial occupancy at the Zn3 site to be close to 24.5(5)%, corresponding to the composition of $Ca_9Zn_{4.49(1)}Sb_9$, which is reasonable considering δ calculated in this work (Table 5.1). The lattice parameters of this sample were found to be a = 21.8525(5) Å, b = 12.5305(3) Å, c = 4.5427(1) Å.

as well as our Rietveld refinement ($Ca_9Zn_{4.49(1)}Sb_9$) on the XRD (Fig. 5.3) of the same $Ca_9Zn_{4.3}Sb_9$ sample is also found within this region.[144]

Due to this uncertainty in the actual sample composition, we shall for the present discussion simply consider δ values in $Ca_9Zn_{4.5-\delta}Sb_9$ to be determined by the experimental Hall carrier concentration, n_H. Since each interstitial Zn deficiency from the charge balanced structure (δ) creates two additional holes in the valence band and one unit cell contains two formula units,

$$\delta = \frac{n_H V}{4}, \tag{5.1}$$

where V is the unit cell volume. Each interstitial Zn also adds d-electrons and d-states to the electronic structure, but as they are fully filled and well below the Fermi level they do not influence the Fermi level. Other defects, such as A-site cation vacancies or defects with different charge states, may also be present. The Hall factor, relating the Hall carrier concentration to the actual number of holes in

Atom	Site	x	y	z
Ca1	2b	0.00000	0.00000	0.50000
Ca2	4g	0.13668	0.13106	0.00000
Ca3	4g	0.09049	0.43244	0.00000
Ca4	4g	0.26378	0.37404	0.00000
Ca5	4h	0.39771	0.20844	0.50000
Sb1	2d	0.00000	0.50000	0.50000
Sb2	4g	0.49299	0.30683	0.00000
Sb3	4g	0.30490	0.11584	0.00000
Sb4	4h	0.35391	0.45580	0.50000
Sb5	4h	0.16831	0.30594	0.50000
Zn1	4h	0.04581	0.27471	0.50000
Zn2	4h	0.23671	0.11227	0.50000

Table 5.1: The relaxed atomic positions, used for electronic structure calculations of $Ca_9Zn_4Sb_9$.

the valence band, is not exactly known but is expected to be around 1. Despite these uncertainties, the important principle here is that the actual defect concentration, represented by δ calculated from the measured Hall carrier concentration n_H, is distinctly different from the nominal composition represented by x. Although δ is not exactly known, it is clearly influenced by the nominal Zn content x in a qualitative manner that can be explained with the understanding of the defect chemistry and equilibrium phase diagram.

Previously, within a given $A_9M_{4+x}Pn_9$ system, no change of carrier concentration was observed by changing x, corresponding to a change in δ values of almost 0. Bux *et al.* attempted to synthesize $Yb_9Mn_{4+x}Sb_9$ with different Mn contents (x) but resulting samples contained a significant amount of impurities and no change in hole concentration was observed. They concluded that no carrier concentration tuning was possible due to its narrow phase width[30] consistent with the observations of Xia *et al.*[117] Similarly, samples with a nominal composition of $Yb_9Zn_{4+x}Sb_9$ (x = 0.2, 0.3, 0.4 and 0.5) were synthesized to tune δ and thermoelectric properties, but all of the investigated samples displayed identical transport properties.[31]

The phase width (range of allowed value of δ) in $Ca_9Zn_{4.5-\delta}Sb_9$ is so narrow that it is safest to assume that all samples with nominal composition $Ca_9Zn_{4+x}Sb_9$ contain one or two impurity phases determined from the nominal composition in the equilibrium phase diagram. Experimentally, the impurity phases can be identified with XRD or SEM analysis (Fig. 5.3 - 5.5). Based on XRD analysis, the samples

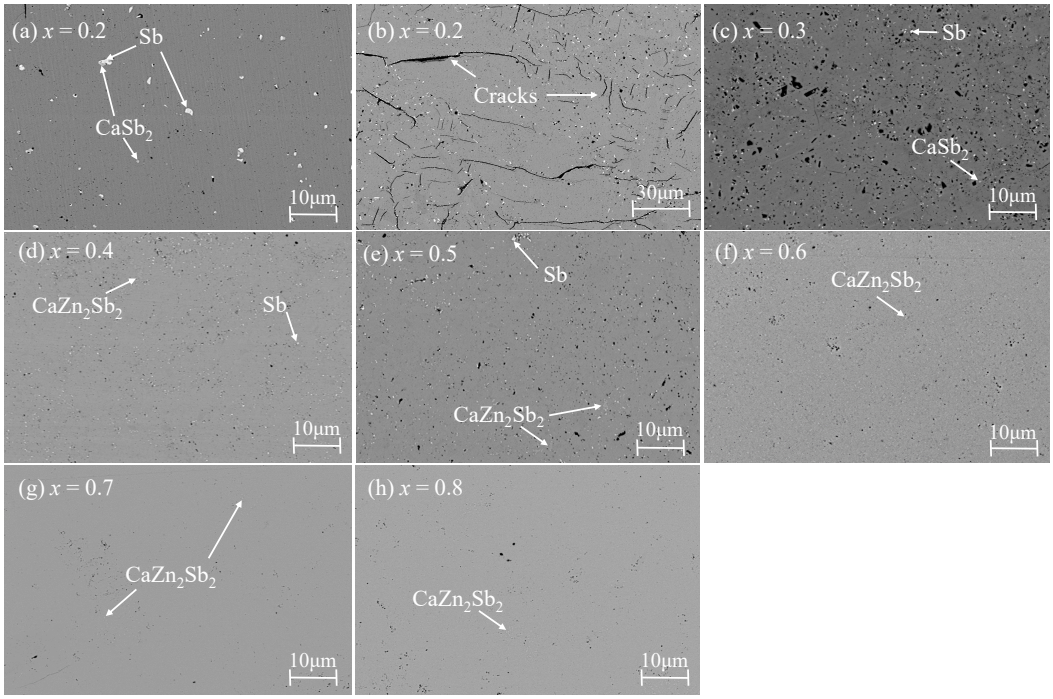

Figure 5.4: SEM results of $Ca_9Zn_{4+x}Sb_9$ (x = 0.2-0.8) samples. (b) Lower magnification of x = 0.2 microstructure to visualize micro cracks on the sample surface.

with low Zn content (x = 0.2 and 0.3) contain Sb and $CaSb_2$ as secondary phases (≤ 2 vol%). For the samples with higher Zn contents of x = 0.4 and 0.5, small amounts of $CaZn_2Sb_2$ and Sb were observed as the main impurity phases (≤ 1-2 vol%). At an even higher Zn content of x = 0.6, only a small amount of $CaZn_2Sb_2$ was identified as the minority phase. Samples of x = 0.7, 0.8 and 23.0 (Ca:Zn:Sb = 1:3:1) were also investigated to characterize the three-phase region of $Ca_9Zn_{4.5-\delta}Sb_9$, $CaZn_2Sb_2$, and a Zn rich phase (Details in section 5.6 and table 1). Thus, it is imperative to make the distinction between nominal composition with x and presumed composition of the phase with δ.

Between different systems ($Yb_9Mn_{4+x}Sb_9$, $Yb_9Zn_{4+x}Sb_9$ and $Ca_9Zn_{4+x}Sb_9$) some variation in δ (Hall carrier concentration) is observed with similar nominal composition, x = 0.2. This is presumably due to a slight change in defect chemistry leading to a small variation in δ, which again is too small to be observed directly by XRD, EDS or WDS but can be detected by the Hall effect. Even though Ca and Yb are isovalent (both +2) in the crystal structure, $Ca_9Zn_{4+x}Sb_9$ samples have lower n_H than those of $Yb_9Mn_{4.2}Sb_9$ and $Yb_9Zn_{4.2}Sb_9$ (Fig. 5.6a). An analogous trend in n_H was reported in AZn_2Sb_2 compounds (A = Sr, Eu, Ca, Yb),[77] in which more

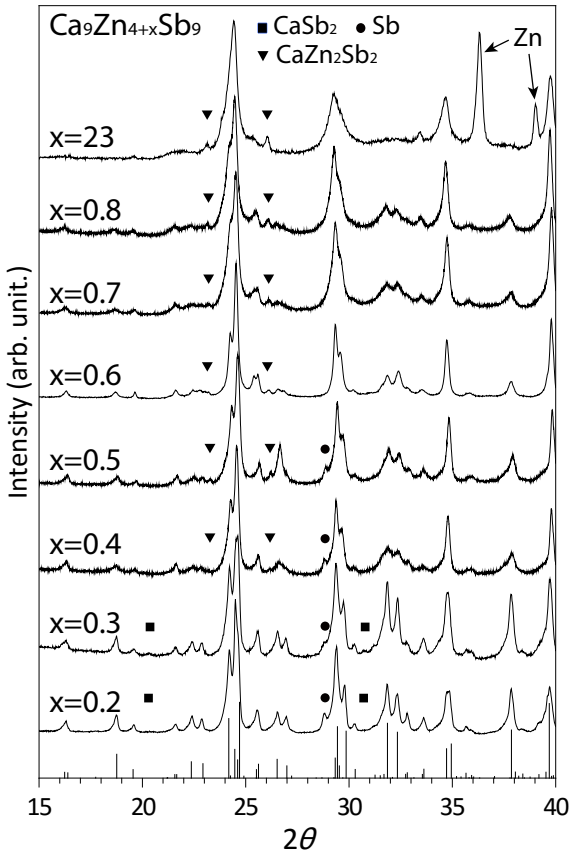

Figure 5.5: XRD results of $Ca_9Zn_{4+x}Sb_9$ ($0.2 \leq x \leq 0.8$,$x = 23$). Bottom bars indicate the peak positions of $Ca_9Zn_{4.478}Sb_9$ acquired by single crystal XRD. Different secondary phases were observed for different samples, which were used to determine the phase regions of each sample.

electropositive atoms on the cation sites decrease the *p*-type carrier concentration of the material. The amount of stable cation vacancies is larger in Yb compounds than in Ca compounds because of the higher electronegativity of Yb. This is due to the electronegativity altering the vacancy defect energy that leads to a higher *p*-type carrier concentration for $YbZn_2Sb_2$. In $A_9M_{4+x}Pn_9$, using Ca instead of Yb also leads to a lower n_H, which may indicate the existence of a smaller amount of cation site vacancies. Compensating defects such as interstitial Zn atoms acting as electron donors while Ca site vacancies forming electron acceptor defects are also possible. Such compensating defects of the form $Ca_{9+\delta}Zn_{4.5-\delta}Sb_9$ could increase the range of *M* atom concentration at the expense of *A* atom concentration or vice versa and extend the $A_9M_{4+x}Pn_9$ phase solubility in the direction of AZn_2Sb_2.

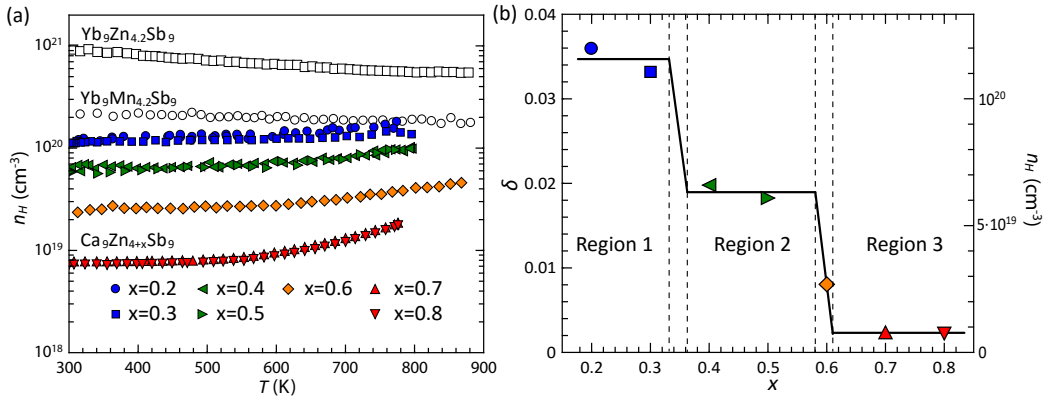

Figure 5.6: (a) Hall carrier concentration (n_H) as a function of temperature and (b) the deficiency of Zn (compared to the ideal semiconductor) in one formula unit (δ) as a function of nominal composition (x) at 400 K. δ is calculated from the Hall carrier concentration, assuming that only Zn partial occupancy contributes to n_H. The right side vertical axis of (b) shows the corresponding Hall carrier concentration. The colors of the data points and the enumerated regions correspond to the phase region where the possible sample compositions are located in Fig. 4a and b.

5.5 Electronic transport properties

The experimental electronic properties of $Ca_9Zn_{4+x}Sb_9$ exhibit decreasing hole concentration with increasing nominal Zn content, x, as shown in Fig. 5.6a. Although the Hall carrier concentration of $Ca_9Zn_{4+x}Sb_9$ qualitatively follows the trend with nominal composition x, a closer inspection shows a step-wise rather than linear decrease (Fig. 5.6b). Assuming that n_H is determined solely by the deviation δ of the amount of Zn in $Ca_9Zn_{4.5-\delta}Sb_9$, we can calculate δ required to yield a given value of n_H. For example, $Ca_9Zn_{4.47}Sb_9$ (δ = 0.03) corresponds to 0.06 holes per formula unit or $n_H = 1.0\times10^{20}\text{cm}^{-3}$. The phase width of $Ca_9Zn_{4.5-\delta}Sb_9$ based on the experimental nH is found to be $0.002 < \delta < 0.036$, as illustrated in Fig. 5.6b. Samples with $x > 0.5$ are still found to be a p-type semiconductor based on their Hall effect measurement, indicating δ is always greater than zero ($\delta < 0$ would be result in n-type samples). Given the presumed range of actual Zn content per formula unit, between 4.464 and 4.498 (given by 4.5 - δ), the nominal range of Zn used to synthesize the samples of 4.2 to 4.8 (represented by 4 + x) is much larger. This shows that controlling the nominal value of x is important, but has a much smaller influence on the actual Zn content (δ) than expected, and the dependence is non-linear.

The resistivity and Seebeck coefficient of the samples increase with increasing

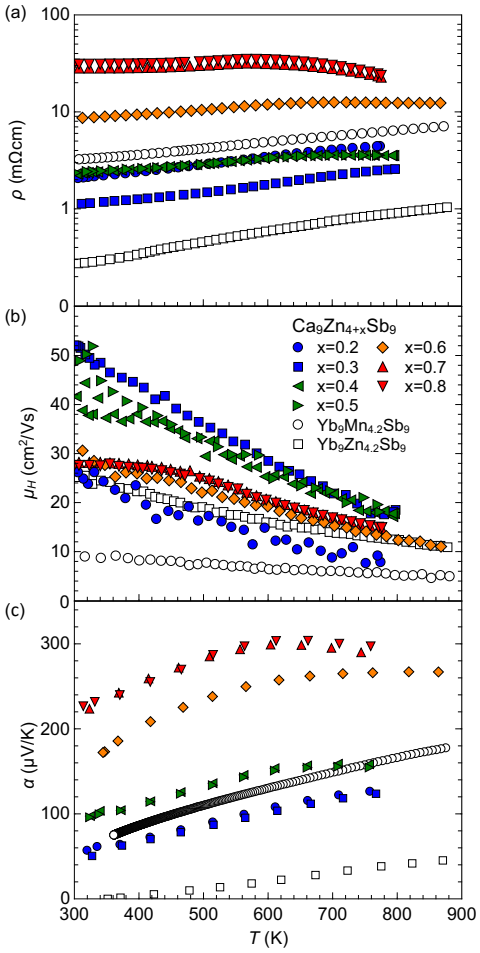

Figure 5.7: (a) Resistivity, (b) mobility, and (c) Seebeck coefficient of $Ca_9Zn_{4+x}Sb_9$ samples as a function of temperature. The trend in resistivity and Seebeck coefficient follows the trend in the carrier concentration except for the resistivity of the $x = 0.2$ sample, which has a lower mobility because of the microstructures in the sample (see Fig. 5.4).

temperature, indicating the expected degenerate semiconducting behaviour (Fig. 5.7). The resistivity of the compounds increases together with Zn content, which is proportional to the decrease in carrier concentration. The resistivity starts decreasing at around 650 K for $x = 0.4$ - 0.8 samples because of minority carrier activation. The trend between $x = 0.2$ and 0.3 is an exception since the $x = 0.2$ sample has a much lower Hall mobility (μ_H) than for $x = 0.3$ due to the cracks found in the sample, as shown in Fig. 5.4. These cracks always appear in samples with $x \leq 0.2$. $Ca_9Zn_{4+x}Sb_9$, like in $Yb_9Zn_{4.2}Sb_9$, has a higher μ_H than $Yb_9Zn_{4.2}Sb_9$ because of its lower effective mass.[31] $Ca_9Zn_{4+x}Sb_9$ has even a higher μ_H than $Yb_9Zn_{4.2}Sb_9$, mainly due to its much lower carrier concentration. The μ_H of the $x = 0.6$, 0.7,

and 0.8 samples are slightly lower than other investigated samples, possibly due to secondary phases. As shown in Fig. 5.5, the amount of $CaZn_2Sb_2$ impurity in the sample slightly increases with increasing Zn content, which may lead to stronger charge carrier scattering. The increasing Seebeck coefficient with Zn content is consistent with the trend in the Hall carrier concentration. Based on the maximum Seebeck coefficient of the $x = 0.6$ sample ($\alpha_{max} = 260\ \mu$V/K) and the corresponding temperature ($T_{max} = 650$ K), the band gap is estimated by

$$E_g = 2e\alpha_{max}T_{max} \tag{5.2}$$

to be $E_g = 0.34$ eV, which is in very good agreement with the calculated band gap of 0.35 eV.[269] The effective mass, m_S^*, of the $x = 0.3$ sample is found to be ~ 0.56 m_e at 400 K.

5.6 Phase diagram approach for optimization of thermoelectric performance

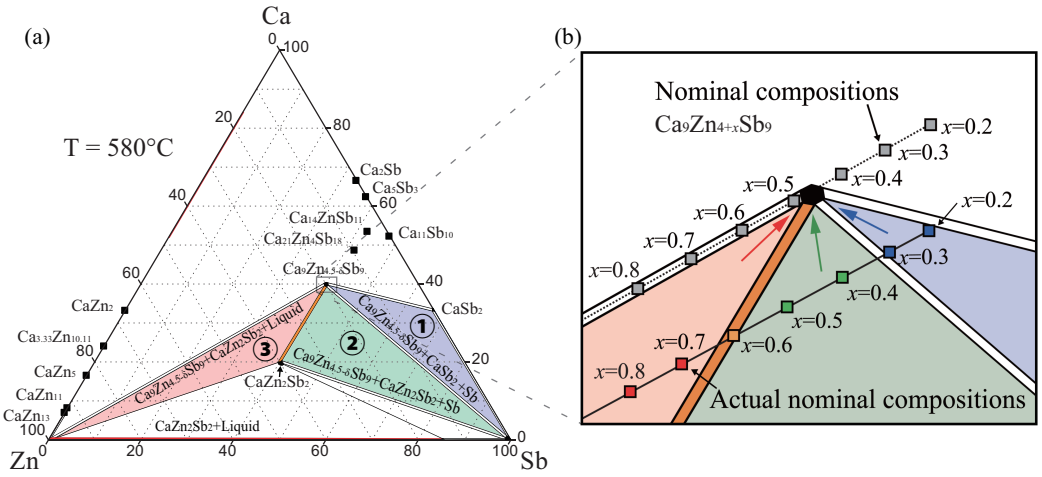

Figure 5.8: (a) Isothermal section at 580 °C of the Ca-Zn-Sb ternary phase diagram and (b) magnified region around $Ca_9Zn_{4.5-\delta}Sb_9$ in (a). In (a) the widths of the single and two phase regions are schematic and enlarged for clarity. Although nominal compositions $Ca_9Zn_{4+x}Sb_9$ are not located within the three-phase regions, XRD and SEM results indicate that resulting samples are in equilibrium with the three-phase regions shown most likely because of Ca deficiency. Moving from one three-phase region to another leads to different fixed compositions of the $Ca_9Zn_{4.5-\delta}Sb_9$ phase as shown by the coloured arrows in (b).

The complicated step-wise behavior of the carrier concentration in Fig. 5.6b can be explained using the equilibrium isothermal section (at 580 °C) of the Ca-Zn-Sb

Nominal composition (x)	Region	Secondary phases	P	δ
0.2	1	Sb, $CaSb_2$	3	0.036
0.3	1	Sb, $CaSb_2$	3	0.033
0.4	2	Sb, $CaZn_2Sb_2$	3	0.020
0.5	2	Sb, $CaZn_2Sb_2$	3	0.018
0.6	Between 2 and 3	$CaZn_2Sb_2$	2	0.008
0.7	3	$CaZn_2Sb_2$, (Zn)	3	0.002
0.8	3	$CaZn_2Sb_2$, (Zn)	3	0.002
23.0 (Ca:Zn:Sb=1:3:1)	3	$CaZn_2Sb_2$, Zn	3	-

Table 5.2: The relaxed atomic positions, used for electronic structure calculations of $Ca_9Zn_4Sb_9$.

ternary phase diagram. The phases shown in Fig. 5.8 and the compositional triangles enclosed by tie-lines are not necessarily complete, as they are based on scarce experimental results, binary phase diagrams in ASM Alloy Phase Diagram Database, and formation energies calculated by the Materials Project and the Open Quantum Materials Database.[270, 271] According to the secondary phases identified by XRD and SEM analysis (see Fig. 5.4 and 5.5, Table 5.2), the samples with x = 0.2 and 0.3 are in the three-phase region of $Ca_9Zn_{4.5-\delta}Sb_9$, $CaSb_2$, and Sb (blue Region 1, in Fig. 5.8). Samples with x = 0.4 and 0.5 are within the three-phase region containing $Ca_9Zn_{4.5-\delta}Sb_9$, $CaZn_2Sb_2$, and Sb (green region 2). Only $CaZn_2Sb_2$ and $Ca_9Zn_{4.5-\delta}Sb_9$ are found in the sample with x = 0.6. Therefore, this sample is presumably formed in the two-phase region between $CaZn_2Sb_2$ and $Ca_9Zn_{4.5-\delta}Sb_9$ (orange region). The samples with nominal Zn contents of x = 0.7 and 0.8 were synthesized to characterize the three-phase region of $Ca_9Zn_{4.5-\delta}Sb_9$, $CaZn_2Sb_2$, and a Zn rich phase (red region 3). XRD analysis on these samples showed only the formation of $Ca_9Zn_{4.5-\delta}Sb_9$ and $CaZn_2Sb_2$, but no Zn rich phase was detected. When a large excess of Zn is used (nominal compositions Ca:Zn:Sb = 1:3:1, x = 23.0), elemental Zn can be identified as the third phase in the XRD data (Fig. 5.5), and visible segregation of melted Zn (melting point 420 °C) is observed when annealed at 580 °C.

Overall, this analysis suggests that the actual nominal compositions are shifted slightly to the Ca deficient side (compared to the nominal compositions of $Ca_9Zn_{4+x}Sb_9$) and across the phase boundaries as shown by the solid line in Fig. 5.8b. This shift may stem from a loss of Ca during the synthesis process which is not unexpected considering the reactivity of Ca with oxygen. Similarly, isotypic $Yb_9Zn_{4+x}Sb_9$ also has cation poor impurities in the reported samples.[31]

According to the Gibbs phase rule under constant temperature and pressure ($F = C - P$ where F, C, and P are the number of degrees of freedom, number of components, and number of phases, respectively), the degrees of freedom F in a three-phase triangle is zero ($C = 3$, $P = 3$), which indicates that the compositions of the phases at the vertex of the triangle are invariant. Therefore, assuming equilibrium, all the samples found in the same three-phase region should have a fixed composition with the same defect concentration, here denoted by δ. This explains why samples found in the three-phase region 1 ($x = 0.2$ and 0.3), region 2 ($x = 0.4$ and 0.5), and region 3 ($x = 0.7$ and 0.8) have very similar n_H, respectively. As expected, samples in the same phase region also have almost the same Seebeck coefficient (Fig. 5.7c). Furthermore, when the homogeneous range of phases (black regions) and two-phase regions are not infinitesimally small and narrow, each $Ca_9Zn_{4.5-\delta}Sb_9$ in the different phase regions have different fixed composition determined by the apexes of the compositional three-phase triangle as shown by the three arrows in Fig. 5.8b. Thus, samples in three different three-phase regions have the three different fixed compositions of the $Ca_9Zn_{4.5-\delta}Sb_9$ phase with three different values of δ. As the nominal Zn content x increases for samples prepared as $Ca_9Zn_{4+x}Sb_9$, the chemical potential of Zn atoms should increase as well, leading to a higher number of interstitial Zn, and therefore decreasing δ in $Ca_9Zn_{4.5-\delta}Sb_9$. On the other hand, small changes to the nominal Zn content x while within the same three-phase region will alter the relative amounts of the three phases seen, but not their chemical composition of the matrix $Ca_9Zn_{4.5-\delta}Sb_9$ phase or δ.

The sample with $x = 0.6$ has only $CaZn_2Sb_2$ as a secondary phase according to SEM and XRD, and the n_H and α of this sample is in between the values of the samples in region 2 and 3. Thus, the sample with $x = 0.6$ is in a two-phase region whose degrees of freedom is one ($C = 3$, $P = 2$: monovariant). In the two-phase region, the composition of the $Ca_9Zn_{4.5-\delta}Sb_9$ phase can vary along the phase boundary between the $Ca_9Zn_{4.5-\delta}Sb_9$ single phase (black region in Fig. 5.8b) and $Ca_9Zn_{4.5-\delta}Sb_9$ + $CaZn_2Sb_2$ two-phase (Orange region in Fig. 5.8b), which can lead to δ in a range between that of region 2 and 3. Thus, any small local change in Zn content while remaining in the two-phase region of the phase diagram will alter the compositions of the resulting two phases, adding to the possibility of local variations of thermoelectric properties in a macroscopic sample.[272]

The change in δ associated with a change in x from 0.2 to 0.8 explains the step-wise behaviour of the carrier concentration. Although the total composition range

allowed is still small, equivalent to $0.002 < \delta < 0.036$, this is sufficient to optimize the thermoelectric properties. In principle, other fixed compositions with different defect concentrations would be found in the three-phase regions on the Ca-rich side of $Ca_9Zn_{4.5-\delta}Sb_9$. This phase boundary mapping analysis also indicates that the range of x previously studied in $Yb_9Mn_{4+x}Sb_9$ and $Yb_9Zn_{4+x}Sb_9$ was not sufficiently large to move into a different phase regions (because of the absence of the tie line between 9-4-9 system and elemental Sb) and that other compositions could be attempted that will be in a different phase region and likely to improve the material.[30, 31]

5.7 Thermal transport properties

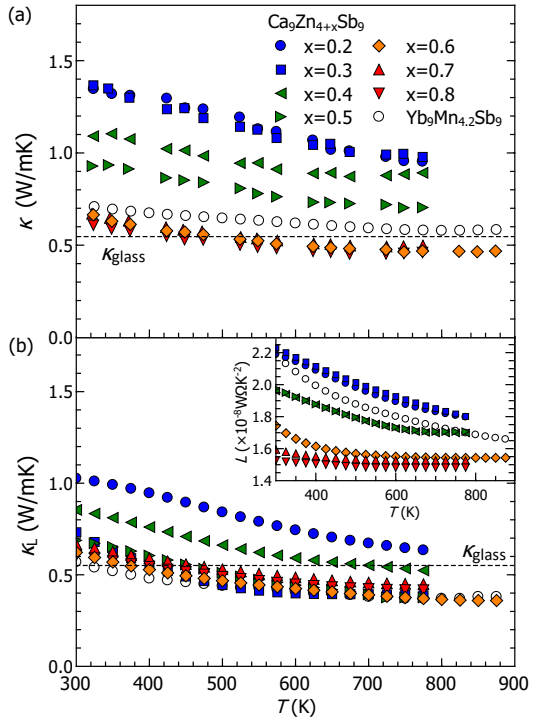

Figure 5.9: (a) Total thermal conductivity of $Ca_9Zn_{4+x}Sb_9$ samples and $Yb_9Mn_{4.2}Sb_9$. All κ values are calculated from thermal diffusivity using Dulong-Petit heat capacity. (b) Lattice thermal conductivity of the same samples is calculated based on the SPB model. Inset shows the Lorenz number for each sample.

Compounds	v_L (m/s)	v_T (m/s)	K (GPa)	G (GPa)	Θ (K)	$\kappa_L glass$
$Yb_9Mn_{4.2}Sb_9$	3070	1730	43.1	23.8	189	0.39
$Yb_9Zn_{4.2}Sb_9$	3228	1920	44.4	29.7	211	0.43
$Ca_9Zn_{4.3}Sb_9$	4170	2450	43.1	27.5	267	0.55

Table 5.3: Speed of sound, bulk and sheer modulus, Debye temperature (Θ), and glassy-limit thermal conductivity values.

The total thermal conductivity, *kappa*, shown in Fig. 5.9, was calculated from

$$\kappa = DdC_p, \tag{5.3}$$

where D is the measured thermal diffusivity, d is the sample's density and C_p is the Dulong-Petit heat capacity. κ has two components; a phonon contribution (κ_L) and electronic contribution (κ_e). κ_e is estimated by the Wiedemann-Flanz law with the Lorentz number (L) calculated within the SPB model.[34, 273] κ_L is calculated by subtracting κ_e from κ. Both the calculated κ_L and L are shown in Fig. 5.9b. κ decreases as the Zn content increases mainly due to the reduction of κ_e.

The dashed line in Fig. 5.9b indicates the estimated amorphous limit to the lattice thermal conductivity (κ_{glass}) calculated from Cahill's method assuming that the phonon mean free path is a half of the phonon wave length [152]:

$$\kappa_{glass} = \frac{1}{2}\left(\frac{\pi}{6}\right)^{1/3} k_B V^{-2/3}(2v_t + v_l). \tag{5.4}$$

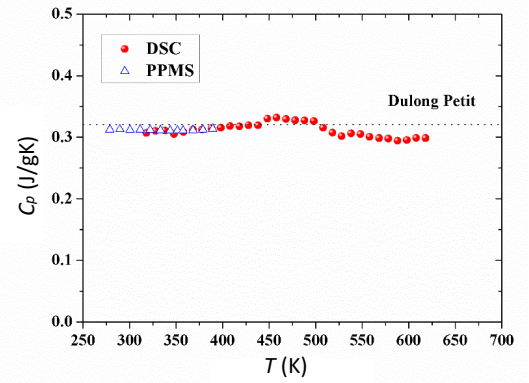

Figure 5.10: Heat Capacity (C_p) measurement result as a function of temperature by PPMS and DSC. Both data sets overlap at around room temperature and measured values are very similar to the Dulong Petit value.

Here v_T, v_L and V are transverse and longitudinal speed of sound (both measured at room temperature), and average volume per atom, respectively. The calculated κ_{glass} of $Yb_9Mn_{4.2}Sb_9$, $Yb_9Zn_{4.2}Sb_9$, and $Ca_9Zn_{4.3}Sb_9$ are shown in Table 5.3. Similar values of the bulk (K) and shear (G) modulus are observed for all three compounds, indicating that the higher speed of sound of $Ca_9Zn_{4+x}Sb_9$ arises mainly from its lower sample density leading to the different κ_{glass}. In general, the κ_L of Zintl phases decreases with increasing temperature due to Umklapp scattering and

approaches κ_{glass}. However, the κ_L of the $Ca_9Zn_{4+x}Sb_9$ sample and also the κ of the samples with $x \geq 0.6$ are found to be even below the estimated κ_{glass}. In fact, almost all phases isotypic to the $Ca_9Zn_{4+x}Sb_9$ structure have extremely low κ_L.[30, 31, 108] To rule out the possibility that the calculated Dulong-Petit heat capacity ($\sim$ 0.32 J/gK) underestimates the real value of C_p, we measured C_p up to 623 K (shown in Fig. 5.10). Our results indicate that the C_p of this material is almost the same as the Dulong-Petit value, similar to reports for other Zintl phases.[274] Similarly, low thermal conductivities have been previously observed in various systems *e.g.*, in disordered layered materials, copper chalcogenides, and other complex Zintl phases.[18, 55, 56, 153, 154, 275] Pöhls *et al.* described the possible overestimation of the κ_{glass} due to the overestimation of the Debye temperature from ultrasound measurements.[156] Possible temperature dependency of the speed of sound could also lead to an overestimation of κ_{glass} at high temperature. Although further investigation is required to determine the origin of such an ultralow thermal conductivity, most notably in other $A_9M_{4+x}Pn_9$ phases, extremely low κ_L could be due to anomalously low Lorenz factors or electron-phonon interactions as demonstrated in $Eu_9Cd_{4-x}CM_{2+x-y}\square_ySb_9$ compounds (where *CM* is a coinage metal *e.g.* Au, Ag, and Cu).[30, 31, 108]

5.8 Thermoelectric Figure of Merit

Combining all the transport properties, the figure of merit (zT) was calculated as a function of temperature as shown in Fig. 6a. The maximum zT increases with increasing nominal Zn content and reaches $\sim$ 1.1 at 875 K for x = 0.6, and then decreases for samples with x = 0.7 and 0.8. Isotropic electronic transport was observed in the polycrystalline samples as shown in Fig. 5.13. The repeated measurements indicate good thermal stability of this Zintl phase (See Fig. 5.14). A large-scale batch of material prepared at NASA/Jet Propulsion Laboratory (JPL) shows good reproducibility (See Fig. 5.15). Reproducibility of the samples in the three-phase regions (Region 1 and 2) was also confirmed with the Seebeck measurements on the reproduced samples (See Fig. 5.16). The figure of merit of various state-of-the-art *p*-type Zintl phases are shown in Fig. 5.12a as a function of temperature, illustrating that $Ca_9Zn_{4+x}Sb_9$ is one of the best *p*-type thermoelectric Zintl phases especially in the intermediate temperature region.[28, 93, 94, 97, 99, 101, 106, 112, 276, 277]

Single parabolic band model (SPB) analysis was carried out to estimate the optimum carrier concentration of $Ca_9Zn_{4+x}Sb_9$ at 400 K, 600 K, and 775 K (Fig. 5.11b).

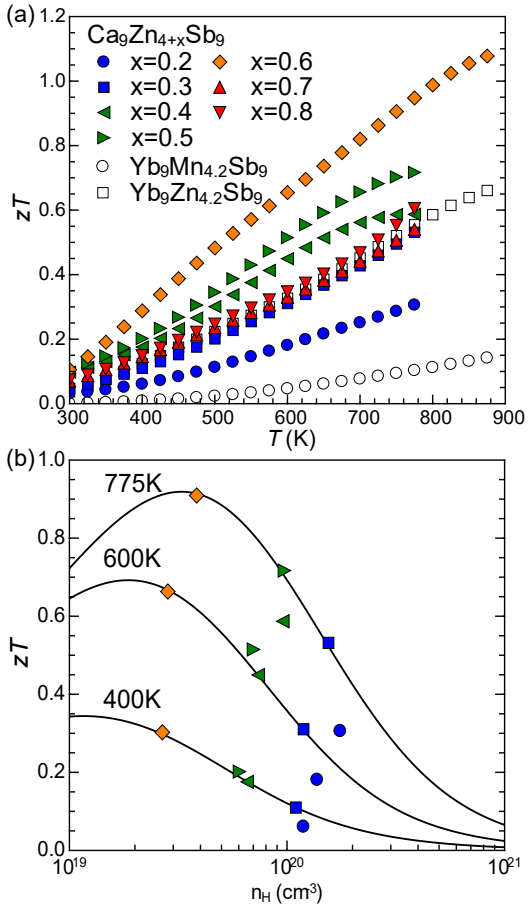

Figure 5.11: (a) zT vs. temperature of investigated samples together with Yb-Mn-Sb and Yb-Zn-Sb analogues. The x = 0.6 sample achieves a zT value of around 1.1 at 875 K. (b) zT vs n_H at 400 K, 600 K and 775 K for x = 0.2 - 0.6 samples. Three solid curves depict estimated zT values calculated within the SPB model based on the experimental data of $Ca_9Zn_{4.3}Sb_9$.

For $Ca_9Zn_{4+x}Sb_9$, experimental data from x = 0.3 was used to avoid error induced by activated minority carriers. According to this analysis, the n_H of $Ca_9Zn_{4+x}Sb_9$ decreases as Zn content increases and reaches close to its optimum, when x = 0.6 (3×10^{19} cm^{-3} at 775 K). Due to even lower n_H and a stronger bipolar effect, samples with x = 0.7 and x = 0.8 have a lower peak in zT and do not agree well with the predicted zT.

The Hall mobility *vs.* lattice thermal conductivity of different p-type Zintl phases is plotted in Fig. 5.12b to uncover possible mechanisms that can rationalize the superior transport properties of $Ca_9Zn_{4+x}Sb_9$.[28, 30, 94, 97, 99, 101, 106, 276–278] Interestingly, this analysis suggests some similarities between $Ca_9Zn_{4+x}Sb_9$ and Zn_4Sb_3, both of which have outstandingly high-μ_H and low-κ_L features.

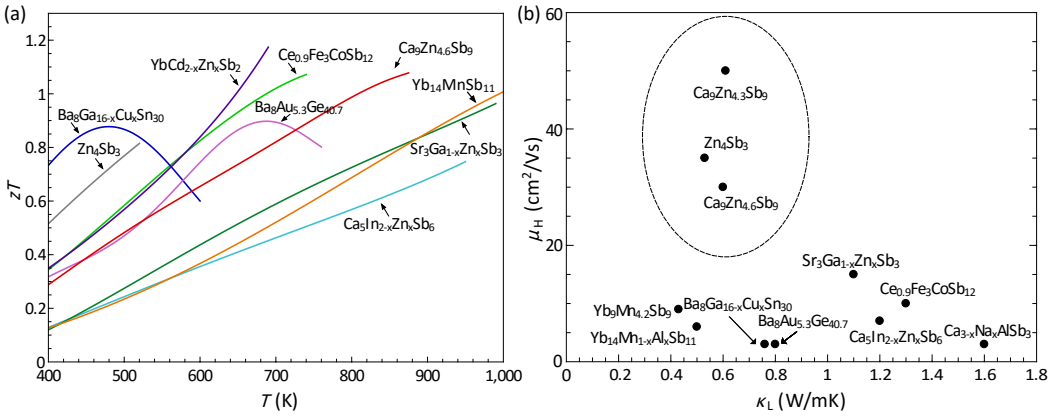

Figure 5.12: (a) zT as a function of temperature for various state-of-the-art p-type Zintl phases up to 1000 K.[28, 93, 94, 97, 99, 101, 106, 112, 276, 277] $Ca_9Zn_{4.6}Sb_9$ shows a high zT in the intermediate temperature region (700 - 900 K). zT of High temperature Zintl thermoelectric, $Yb_{14}MnSb_{11}$, approaches 1.4 at 1275 K. (b) Hall mobility vs lattice thermal conductivity of various Zintl phases calculated within the SPB model at room temperature. High mobility and low lattice thermal conductivity is preferred for thermoelectric materials as observed for both $Ca_9Zn_{4+x}Sb_9$ and Zn_4Sb_3.

Among the compounds shown in Fig. 5.12b, there are several possible mechanisms which are detrimental to the high Hall mobility: I) Alloy/point defect scattering by introducing an additional element in the anionic structure,[62, 65, 67] II) A larger electronegativity difference in the anionic framework, which increases the effective mass of p-type conduction due to a smaller dispersion of the band,[147] III) Mobility activation associated with a potential barrier such as grain boundary,[101, 276] IV) Spin disorder scattering, which is a consequences of an exchange interaction between free charge carriers and localized magnetic moments.[89, 279] High-μ_H compounds, $Ca_9Zn_{4+x}Sb_9$ and Zn_4Sb_3, do not have any of these detrimental mechanisms for the mobility.

In the crystal structure of Zn_4Sb_3, there are contiguous channels of interstitial Zn sites along the c axis with high Zn atomic displacement parameters leading to larger anharmonicity.[93] As shown in Fig. 5.1a, the partially occupied Zn sites in $Ca_9Zn_{4+x}Sb_9$ also form a channel-like structure, which might add some additional anharmonicity such as static or dynamic disorder of partially occupied Zn atoms leading to extremely low thermal conductivity. Partially occupied sites are commonly observed in intercalation compounds and ion-conducting solids, which often exhibit ultralow lattice thermal conductivity.[280, 281]

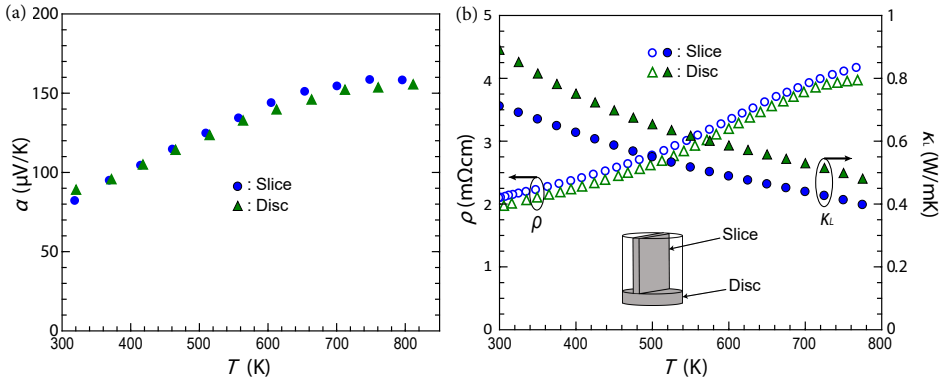

Figure 5.13: Isotropic electronic properties of $Ca_9Zn_{4.5}Sb_9$. Temperature dependent Seebeck coefficient (a), resistivity, and lattice thermal conductivity (b) in the directions parallel (blue/circle) and perpendicular (green/triangle) to that of the pressure applied during the hot press. Thermal conductivity indicates some anisotropy, in which the difference is almost the same as the values between $x = 0.4$ and 0.5 samples in Fig.5.9. Thus further investigation is required to identify the origin of small difference in thermal conductivity.

5.9 Conclusion

The thermoelectric properties of the Zintl phase $Ca_9Zn_{4+x}Sb_9$ composed of inexpensive elements were studied by phase boundary mapping. Electronic transport measurements reveal that the carrier concentration of $Ca_9Zn_{4+x}Sb_9$ can be tuned by changing the Zn content. Depending on the nominal Zn content represented by x, the Zintl phase $Ca_9Zn_{4+x}Sb_9$ is found to have distinctly different actual defect concentration, represented by δ. Although δ is not exactly known, it is clearly influenced by x in a qualitative manner and overall the phase boundary mapping of the isothermal section of the ternary phase diagram applied here sheds light on the electronic transport behavior of the investigated samples. With the phase boundary mapping, the Zintl phase $Ca_9Zn_{4+x}Sb_9$ having high mobility and low thermal conductivity attains a maximum zT value of 1.1 at 875 K for the $x = 0.6$ sample. This is one of the highest values among all characterized p-type Zintls in the intermediate temperature range, indicating great potential for use in thermoelectric applications. The unique approach to control the doping concentrations of ternary compounds demonstrated how using phase boundary mapping here can be used in other complex semiconductors for photovoltaic and thermoelectric applications.

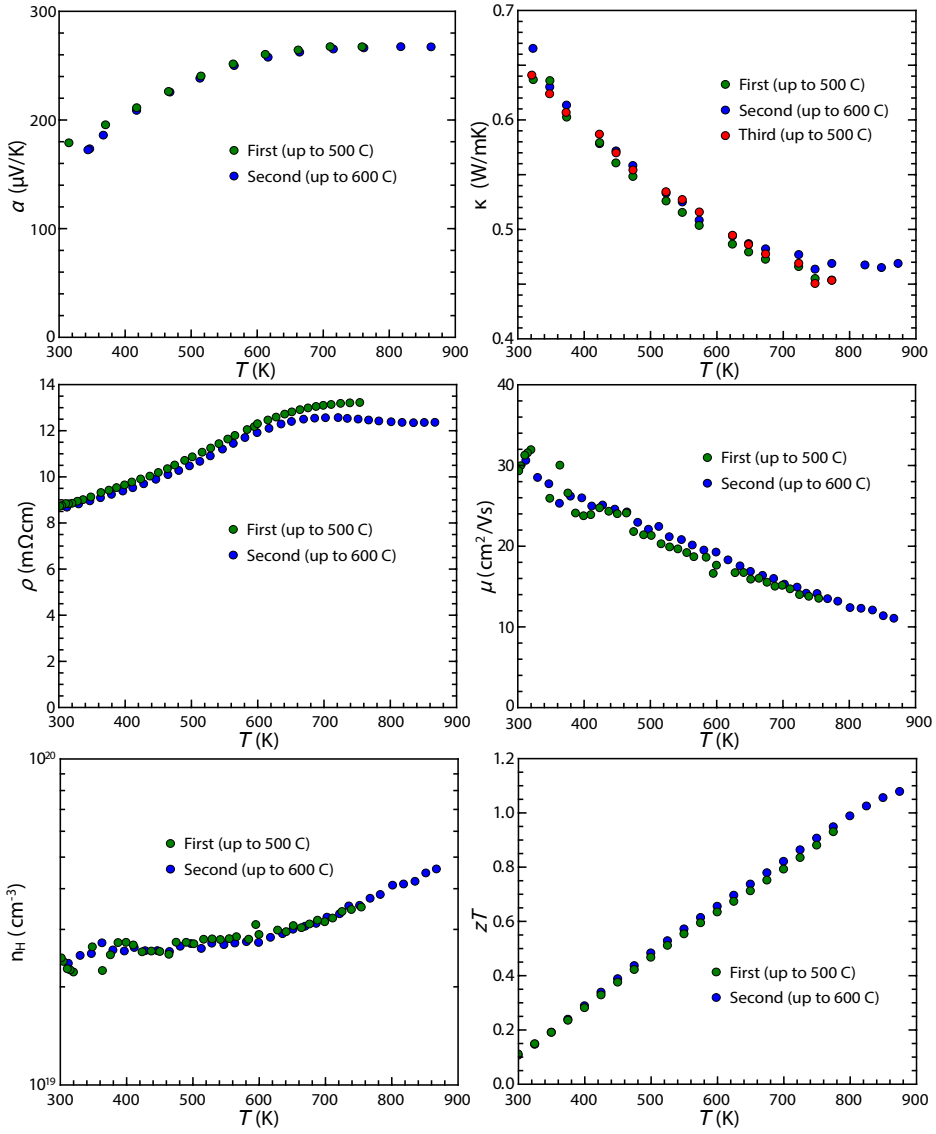

Figure 5.14: Reproducibility of thermoelectric properties of $Ca_9Zn_{4.6}Sb_9$. Transport properties were measured at least twice to verify the results. First and second measurement were carried out up to 500 °C and 600 °C, respectively. All of the measurement results show almost identical properties.

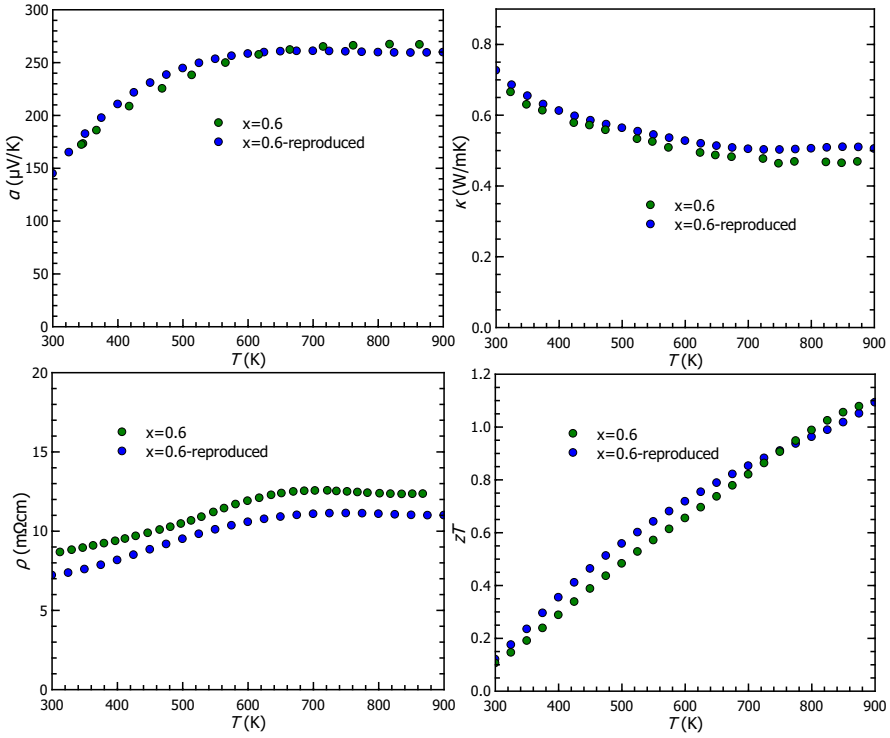

Figure 5.15: Sample reproducibility of $Ca_9Zn_{4.6}Sb_9$ (x = 0.6). The reproduced sample was synthesized at NASA/JPL for testing this material to be used in a future thermoelectric generator. 50 g of powder was pressed to acquire sample pellet with a diameter of three inches. The reproduced sample displays almost identical transport behaviour with very similar zT up to 875 K.

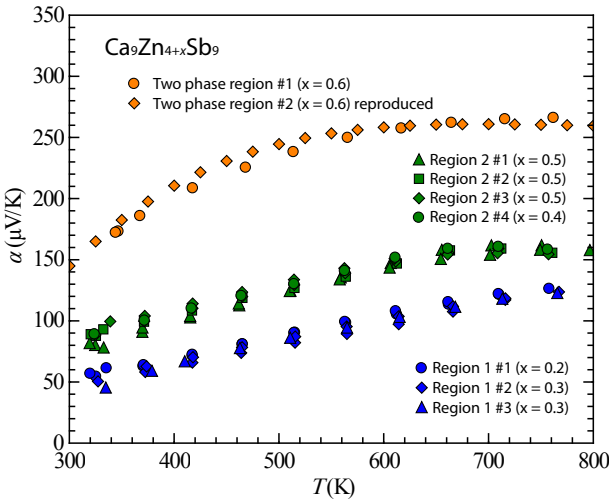

Figure 5.16: Reproducibility of the samples in different phase regions. The samples of $x = 0.3$ and 0.5 are reproduced and their Seebeck coefficients are measured. The symbols with the same color show the data from the samples in the same three-phase regions. The result shows that we can acquire almost identical samples repeatedly from the same phase region. The three-phase region numbers are shown in Fig. 5.8 in the main text with the same colors: $x = 0.2$ and 0.3 belong to region 1 (blue), $x = 0.4$ and 0.5 are in region 2 (green), and $x = 0.6$ sample exists in the two phase region between region 2 and 3 (orange).

Chapter 6

Thermoelectric properties of the $Yb_9Mn_{4.2-x}Zn_xSb_9$ solid solutions

This chapter contains contents reproduced with permission from *Journal of Materials Chemistry A* **2**, 7478-7483 (2014).

6.1 Summary of research

$Yb_9Mn_4.2Sb_9$ has been shown to have extremely low thermal conductivity and a high thermoelectric figure of merit attributed to its complex crystal structure and disordered interstitial sites. Motivated by previous work showing that isoelectronic substitution of Mn by Zn leads to higher mobility by reducing spin disorder scattering, this study investigates the thermoelectric properties of the solid solution $Yb_9Mn_{4.2-x}Zn_xSb_9$ (x = 0, 1, 2, 3, and 4.2). Measurements of the Hall mobility at high temperature (up to 1000 K) show that the mobility can be increased by more than a factor of 3 by substituting Zn into Mn sites. This increase is explained by the reduction of the valence band effective mass with increasing Zn, leading to a slightly improved thermoelectric quality factor relative to $Yb_9Mn_{4.2}Sb_9$. However, increasing the Zn-content also increases the *p*-type carrier concentration, leading to metallic behavior with low Seebeck coefficients and high electrical conductivity. Varying the filling of the interstitial site in $Yb_9Zn_{4+y}Sb_9$ (y = 0.2, 0.3, 0.4, and 0.5) was attempted, but the carrier concentration ($\sim 10^{21}$ cm^{-3} at 300 K) and Seebeck coefficients remained constant, suggesting that the phase width of $Yb_9Zn_{4+y}Sb_9$ is quite narrow. Although varying Zn content was not effective, further exploration of accessible thermodynamic states of 9-4-9 phase with phase boundary mapping revealed there are multi-phase equilibria which can reduce the carrier concentration, resulting in increasing zT by a factor of five.

6.2 Introduction

Solid-state thermoelectric generators would be an ideal clean and reliable source of energy harvesting system due to their ability to generate electricity directly from waste heat. For the purpose of widespread applications, it is necessary to improve the efficiency of thermoelectric materials, quantified by the thermoelectric figure of merit ($zT = \alpha^2 T/\kappa\rho$).[232] A good thermoelectric material must strike a balance between a large Seebeck coefficient (α), low electrical resistivity (ρ), and

low total thermal conductivity (κ), all of which are related *via* the free majority carrier concentration (n).[22] Here, the total thermal conductivity is combination of electronic thermal conductivity (κ_e) and lattice thermal conductivity (κ_L).

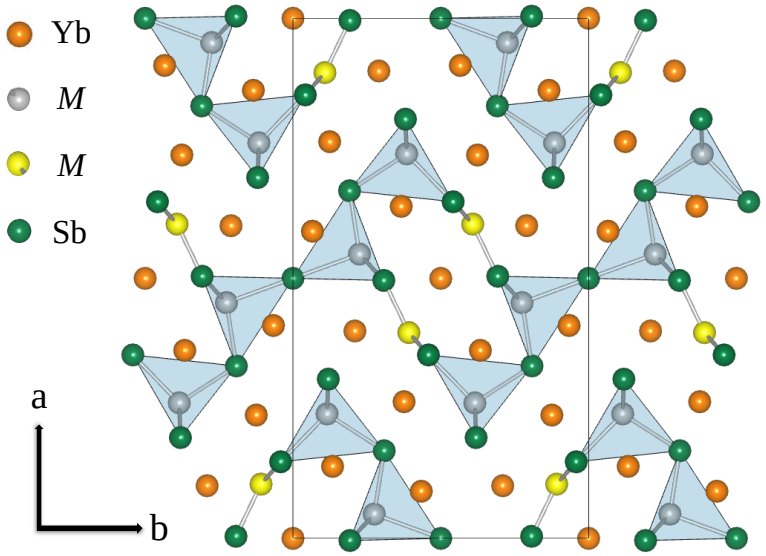

Figure 6.1: The $Yb_9M_{4+x}Sb_9$ structure contains infinite M_4Sb_9 "ribbons" made up of corner sharing MSb_4 tetrahedra, where M is a 2+ transition metal that can be either Mn, Cd or Zn.[118, 144] Partially occupied M-interstitial sites (yellow spheres) link neighboring M_4Sb_9 ribbons into a pseudo two-dimensional framework.

Zintl compounds provide many of the characteristics required for good thermoelectric materials.[89, 282] Zintl phases are made up of electropositive cations that donate their electrons to anions, which in turn must form covalent bonds to satisfy valence.[87, 265] They often have very low lattice thermal conductivity due to their large unit cells, and it is possible to finely tune their electronic properties by doping, providing a route to improved zT. High thermoelectric efficiency has been demonstrated in a number of different Zintl compounds[28, 30, 79, 104, 105, 111, 123, 126, 138, 146, 148, 283] including $Yb_{14}MnSb_{11}$ and $YbCd_{2-x}Zn_xSb_2$, both of which have zT values above unity at high temperatures.[80, 101, 103, 112, 138, 149, 284–294]

Recently, $Yb_9Mn_{4.2}Sb_9$ was shown by Bux *et al.* to have promising thermoelectric performance (zT = 0.7 at 950 K)[30]. The structure of $Yb_9M_{4+x}Sb_9$ is shown in Fig. 6.1, where M can be either Mn^{2+}, Cd^{2+} or Zn^{2+}.[118, 144] Although this structure type was originally discovered in 1970's,[267] the interstitial site was not recognized until 2004 by Bobev *et al.*[144] The structure contains ribbons

of MSb_4 tetrahedra that are connected by partially occupied interstitial M sites. The $Yb_9M_{4+x}Sb_9$ structure would be charge balanced based on a simple electron counting rules if the interstitial M sites were 25% occupied, corresponding to x = 0.5. In practice, the Mn analogue, $Yb_9Mn_{4+x}Sb_9$, was found to behave as a line compound with approximately 10% occupation of the interstitial sites (x = 0.2).[30, 118] In the Zn-containing analogue, the exact composition is unclear, as the literature reports four different stoichiometries ($Yb_9Zn_{4.18}Sb_9$, $Yb_9Zn_{4.23}Sb_9$, $Yb_9Zn_{4.380}Sb_9$ and $Yb_9Zn_{4.384}Sb_9$) determined from refinement of single crystal X-ray diffraction data.[118, 144]

The high zT reported for $Yb_9Mn_{4.2}Sb_9$ stems from its low, glass-like lattice thermal conductivity ($\kappa_L \approx 0.5$ W/mK at room temperature) and optimized electronic properties.[30] To improve zT further, it is thus necessary to improve the inherent electronic properties of this system by tuning either the band structure or carrier scattering. One potential route is to increase the carrier mobility by substituting Zn on the Mn site, as demonstrated in the $YbZn_{2-x}Mn_xSb_2$ and $Yb_{14}Mn_{1-x}Zn_xSb_9$ solid solutions.[123, 146] In $YbZn_{2-x}Mn_xSb_2$, the mobility of the Zn end-member is much higher than that of the Mn end-member, even though the effective mass remains unchanged. Similarly, in $Yb_{14}Mn_{1-x}Zn_xSb_9$, increased Zn content leads to improved mobility. In both cases, the substitution of Zn leads to improved thermoelectric performance. These results motivate the current investigation of the thermoelectric properties of the $Yb_9Mn_{4.2-x}Zn_xSb_9$ solid solution (x = 0, 1, 2, 3 and 4.2).

6.3 Synthesis and Characterization

Synthesis and Characterization. $Yb_9Mn_{4.2-x}Zn_xSb_9$ (x = 0, 1, 2, 3 and 4.2) and $Yb_9Zn_{4+y}Sb_9$ (y = 2, 3, 4 and 5) samples were prepared by ball milling followed by hot pressing (details are described in the Experimental section). To characterize these samples, X-ray diffraction (XRD) was performed on the polycrystalline slices at room temperature. Fig. 6.2 shows the XRD results for all of the $Yb_9Mn_{4.2-x}Zn_xSb_9$ samples (x = 0, 1, 2, 3 and 4.2). For the x = 4.2 sample, the Rietveld fit and residual are shown as red curves and blue curves respectively. Table 6.1 shows lattice parameters for solid solutions. As the amount of Zn increases, each parameter follows the same trend as reported results.[118, 144] Scanning electron microscopy confirmed that the phase purity of the Zn-containing samples is approximately 95% and revealed YbM_2Sb_2 (M = Zn or Mn) as a secondary phase.

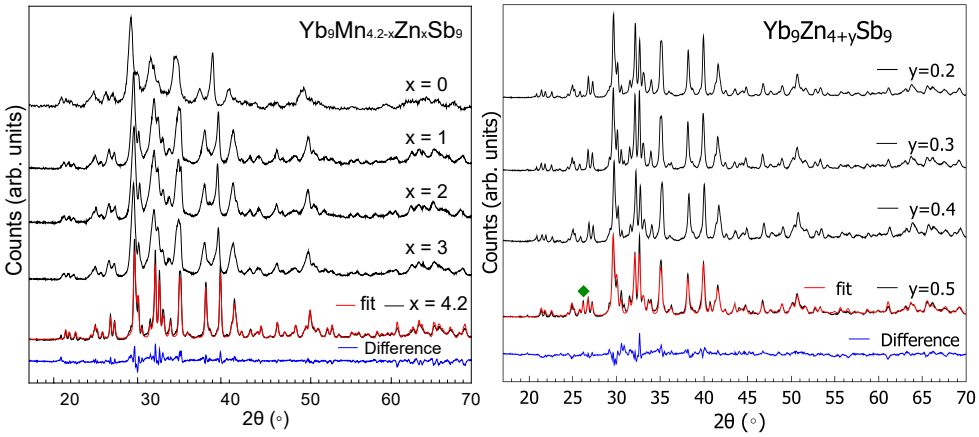

Figure 6.2: X-ray diffraction patterns for $Yb_9Mn_{4.2-x}Zn_xSb_9$ (x = 0, 1, 2, 3 and 4.2) samples exhibit no significant impurity phases. The Rietveld fit and difference profile are shown for the Zn end-member.

Composition	a (Å)	b (Å)	c (Å)
$x = 1$	21.834	12.327	4.5841
$x = 2$	21.764	12.334	4.5664
$x = 3$	21.711	12.343	4.5451
$x = 4.2$	21.692	12.409	4.5278

Table 6.1: Lattice parameters for $Yb_9Mn_{4.2-x}Zn_xSb_9$ are calculated form XRD results with Rietveld fit. As the amount of Zn increases, each parameter changes from Mn end member side to Zn end member and this follows the reported trend.[118, 144]

6.4 Electronic transport properties

The electronic transport properties of $Yb_9Mn_{4.2-x}Zn_xSb_9$ (x = 0, 1, 2, 3 and 4.2) samples are shown in Fig. 6.3 and 6.4. The Mn analogue, $Yb_9Mn_{4.2}Sb_9$, is a line compound with an electron deficient composition, resulting in a carrier concentration of 4×10^{20} h^+/cm^3 and degenerate semiconducting behavior. Surprisingly, considering that Zn and Mn both have the same valence state in this structure, substituting Zn on the Mn site increases the carrier concentration (n_H) sharply, as shown in Fig. 6.3a. Using simple electron counting rules, a carrier concentration of $n_H = 0$ h^+/cm^3 corresponds to 25% occupation of the interstitial sites ($Yb_9M_{4.5}Sb_9$), while completely empty interstitial sites ($Yb_9M_{4.0}Sb_9$) yield $n_H = 1.66 \times 10^{21}$ h^+/cm^3. Thus, the higher n_H in Zn-containing samples may indicate that the solubility of Zn on the intersistial sites is lower than that of Mn. Additionally, in the Zn containing samples, n_H decreases by nearly an order of magnitude as the temperature increases.

Both of these effects may be because introducing Zn changes the defect chemistry by lowering the energy to form accepter defects.[80]

The Hall mobility (n_H) of $Yb_9Mn_{4.2-x}Zn_xSb_9$ samples (Fig. 6.3c) decreases with temperature as expected when acoustic phonons are the primary scattering source. The change in n_H as a function of Zn content at 300 K is shown in Fig. 6.3d. The mobility of the Zn end-member is increased by a factor of three relative to the Mn analogue. The slight reduction at intermediate values of x is due to the disorder on the transition metal site.[67]

Increased mobility can arise from either increased carrier relaxation time (τ) or decreased effective mass (m^*). When acoustic phonon scattering controls the mobility, the scattering rate $1/(\tau(k))$ is determined by the acoustic deformation potential (Ξ), acoustic phonon velocity (v_s), density (d), and the density of states ($g(E)$).[295]

$$\frac{1}{\tau(k)} = \frac{k_B T \Xi^2 \pi}{\hbar} \frac{g(E)}{v_s^2 d} \tag{6.1}$$

Substituting the density of states in three dimensions assuming a parabolic band

$$g_{3D}(E) = \frac{1}{2\pi^2} \left(\frac{2m^*}{\hbar^2} \right)^{3/2} \sqrt{E} \tag{6.2}$$

into Eq.6.1 yields the following relationship which shows that τ also dependent on effective mass in this case.

$$\tau \propto \frac{1}{(m^*)^{3/2}} \tag{6.3}$$

Inserting Eq 6.3 into the expression for mobility, the following proportionality is acquired for mobility limited by acoustic phonon scattering.

$$\mu \propto \frac{\tau}{m^*} \propto \frac{1}{(m^*)^{5/2}} \tag{6.4}$$

The Seebeck coefficients (α) of $Yb_9Mn_{4.2-x}Zn_xSb_9$ (x = 0, 1, 2, 3 and 4.2) samples are shown as a function of temperature and carrier concentration in Fig. 6.4a and b, respectively. The Seebeck coefficients decrease as the amount of Zn, and thus the carrier concentration, increases. However the decrease in α is much greater than should be expected if m^* is unchanged. From the experimental Seebeck coefficients,

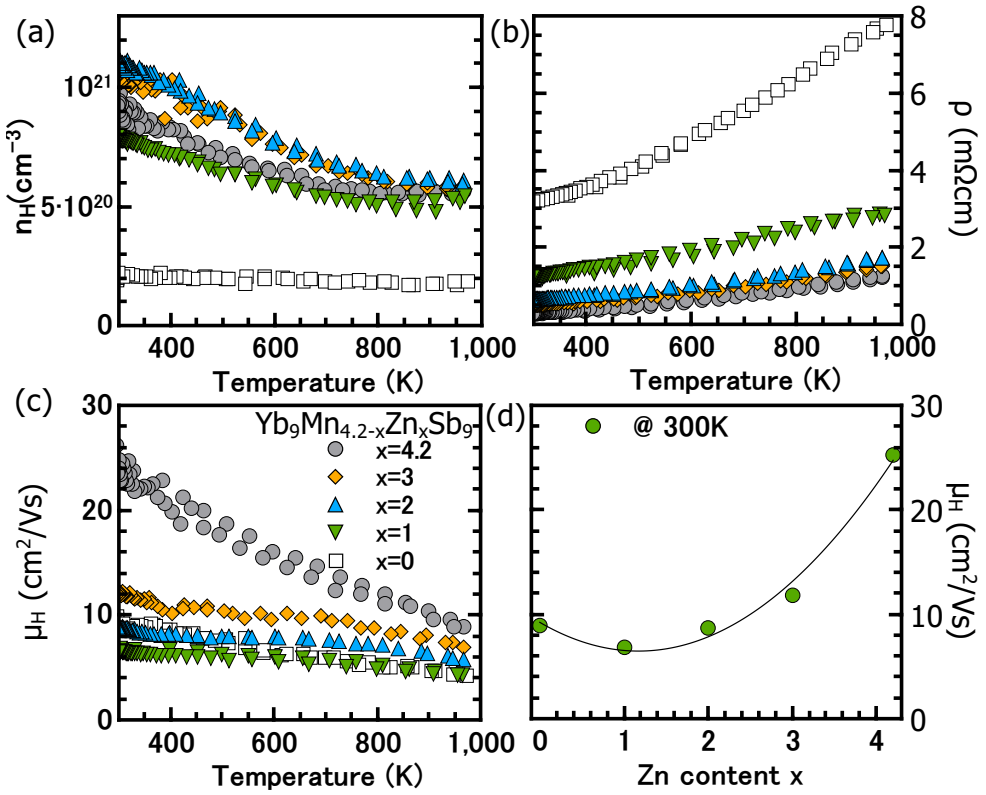

Figure 6.3: With increasing Zn content, x, the (a) Hall carrier concentration of $Yb_9Mn_{4.2-x}Zn_xSb_9$ samples increases and (b) the resistivity decreases. (c) The Hall mobility decreases with temperature due to acoustic phonon scattering. (d) As a function of x at 300 K, the mobility decreases due to alloy scattering and then rises sharply with complete substitution of Mn by Zn.

the chemical potentials (η) at 975K are calculated within a single parabolic band (SPB)[148] model using Eq. 6.5 with $\lambda = 0$ (acoustic-phonon scattering), where $F_j(\eta)$ is the Fermi integral given in Eq 6.7. The hole effective masses for the pure Zn and pure Mn samples (0.65 m_e and 1.2 m_e, respectively), determined from Eq 6.5 using the experimental n_H, were used to generate the dashed curved shown in Fig. 6.4b.

$$\alpha = \frac{k_B}{e}\left(\frac{(2+\lambda)\,F_{1+\lambda}(\eta)}{(1+\lambda)\,F_\lambda(\eta)} - \eta\right) \tag{6.5}$$

$$n = 4\pi\left(\frac{2m^* k_B T}{h^2}\right)^{3/2} F_{1/2}(\eta) \tag{6.6}$$

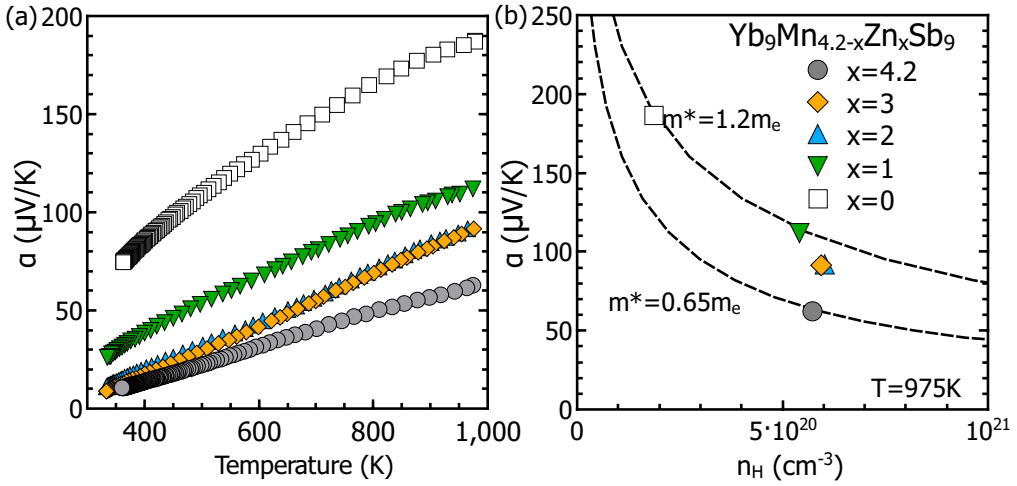

Figure 6.4: (a) The Seebeck coefficients of $Yb_9Mn_{4.2-x}Zn_xSb_9$ (x = 0, 1, 2, 3 and 4.2) samples are consistent with degenerate semiconducting behavior. (b) The dashed curves, calculated with an SPB model using the parameters shown in Table 4, indicate that m^* is decreasing as the amount of Zn is increased.

$$F_j(\eta) = \int_0^\infty \frac{\zeta^j d\zeta}{1 + \exp[\zeta - \eta]} \tag{6.7}$$

From Eq 6.4, we can see that the observed difference in m^* can fully explain the difference in mobility between the Mn and Zn analogues of the $Yb_9M_{4.2}Sb_9$ structure. An increased τ due to reduced spin disorder scattering is thus not necessary to explain the increased mobility in this case. This is in contrast to the $YbZn_{2-x}Mn_xSb_2$ system, in which m^* remained constant, and τ increased upon Zn substitution.

6.5 Thermal transport properties

Shown in Fig. 6.5a, the total thermal conductivity (κ_{total}) for $Yb_9Mn_{4.2-x}Zn_xSb_9$ samples was calculated from the measured thermal diffusivity D using $\kappa_{total} = DdC_p$, where d is the geometric density and C_p is the Dulong Petit heat capacity. In Zn-containing samples, κ_{total} is higher than in the Mn end-member due to the dominance of the electronic contribution. The lattice component (κ_L) of the thermal conductivity was obtained by subtracting the electronic component (κ_e), calculated *via* the Wiedemann-Flanz law from the total thermal conductivity ($\kappa_e = LT\sigma$, where L and σ are the Lorenz number and electrical conductivity, respectively). Often, L is calculated as a function of temperature using an SPB model, thus falling in between the non-degenerate and degenerate limits (1.5 and 2.4, respectively). Using an SPB model yields a lattice thermal conductivity (Fig. 6.5b) for $Yb_9Mn_{4.2}Sb_9$ that is near

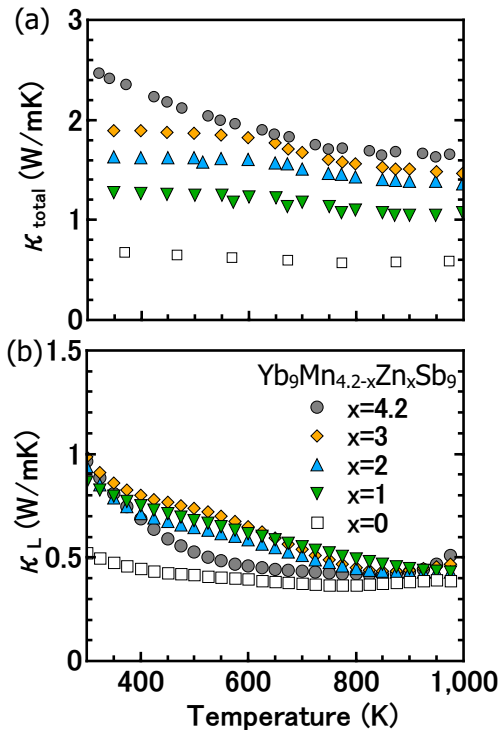

Figure 6.5: (a) The total thermal conductivity of $Yb_9Mn_{4.2-x}Zn_xSb_9$ (x = 0, 1, 2, 3 and 4.2) increases with x. (b) The lattice thermal conductivity was estimated for Zn-containing samples using the temperature independent Lorenz numbers given in Table 6.3.

the minimum theoretical value (κ_{glass}), defined by Eq 6.8.

$$\kappa_{glass} = \frac{1}{2}\left(\frac{\pi}{6}\right)^{1/3} k_B V^{-\frac{2}{3}} \left(2v_T + v_L\right) \tag{6.8}$$

Here, V, v_T, and v_L are the average volume per atom, the transverse speed of sound, and longitudinal speed of sound respectively.17, 42 Room temperature ultrasonic measurements of the Zn end-member show that v_T, and v_L are comparable to the Mn analogue, as shown in Table 6.2, suggesting that the Zn- and Mn-based samples should have similar values of κ_L;[30] however, in the Zn-containing samples, an SPB model yields unrealistically high values of L, and thus underestimates κ_L. Thus, in Fig. 6.5b, rather than using an SPB model for L in the Zn-containing samples, we use L as a temperature-independent "fitting parameter" by setting $\kappa_L = \kappa_{glass}$ at 923 K. The resulting values of L are given in Table 6.3. Note that the use of a temperature-independent L for the Zn-containing samples leads to slightly overestimated values of κ_L at lower temperatures.

Speed of sound	Longitudinal	Transverse
$Yb_9Zn_{4.2}Sb_9$	3228 m/s	1920 m/s
$Yb_9Mn_{4.2}Sb_9$	3070 m/s	1730 m/s

Table 6.2: Room temperature ultrasonic measurements: shows that the longitudinal and transverse speeds of sound Zn compound are slightly higher than the Mn analogue.

Composition	Lorenz number ($\times 10^{-8}\cdot W\cdot\Omega\cdot K^{-2}$)
$x = 1$	1.77
$x = 2$	1.61
$x = 3$	1.70
$x = 4.2$	1.50

Table 6.3: Lorenz numbers were obtained by setting the minimum experimental lattice thermal conductivities to the calculated thermal conductivity assuming glassy limit. For the pure Mn sample, L was calculated using an SPB model as shown in ref.[30].

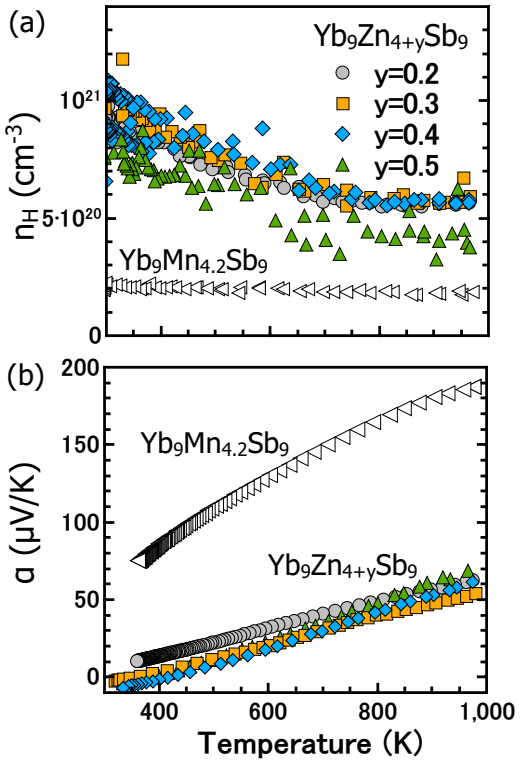

Figure 6.6: (a) The carrier concentration remains unchanged in samples with synthetic compositions of $Yb_9Zn_{4+y}Sb_9$ ($y = 2$, 3, 4 and 5). (b) The Seebeck coefficients are also unaffected by varying the synthetic Zn content.

6.6 Varying interstitial Zn content

Although the mobility of $Yb_9Zn_4Sb_9$ is three times higher than that of the Mn analogue, the carrier concentration is higher than typically desired for thermoelectric applications. In an attempt to control the carrier concentration by increasing the interstitial Zn concentration, we synthesized $Yb_9Zn_{4+y}Sb_9$ samples with y = 0.2, 0.3, 0.4 and 0.5. However, Hall measurements indicate that the carrier concentration remains constant ($n_H \sim 10^{21}$ h^+/cm^3) as the amount of Zn added synthetically is varied (Fig. 6.6a). The Seebeck coefficients, shown in Fig. 6.6b, also remain nearly constant as a function of synthetic Zn content, suggesting that the composition range of $Yb_9Zn_{4+y}Sb_9$ may be quite narrow, similar to that of the Mn analogue.

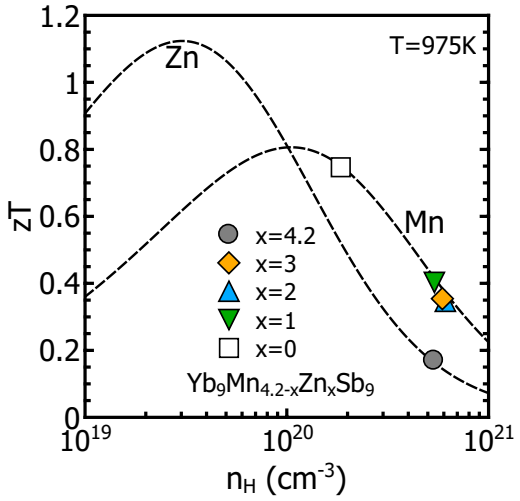

Figure 6.7: (a) The figure of merit of $Yb_9Mn_{4.2-x}Zn_xSb_9$ samples decreases with increasing carrier concentration and Zn content. An SPB model predicts an optimized zT of 1.1 in the Zn system at $n_H = 4\times10^{19}$ h^+/cm^3.

6.7 Figure of merit

Fig. 6.7 shows the experimental zT of $Yb_9Mn_{4.2-x}Zn_xSb_9$ solid solution samples (x = 0, 1, 2, 3, 4.2) as a function of carrier concentration at 975 K. An SPB model was used to predict the figure of merit as a function of n for the $Yb_9Mn_{4.2}Sb_9$ and $Yb_9Zn_{4.2}Sb_9$ end-members (shown as dashed curves) using the parameters in Table 6.4. The lower effective mass and higher mobility in the Zn analogue shift the optimal carrier concentration downwards relative to $Yb_9Mn_{4.2}Sb_9$. The predicted maximum figure of merit is somewhat higher for the Zn analogue due to its higher weighted mobility and dimensionless quality factor.[24, 41] However, the experimental zT of Zn containing samples is far lower than that of the Mn end-member, due to their

high carrier concentrations. While the carrier concentration of $Yb_9Mn_{4.2}Sb_9$ is very close the optimal value, samples with Zn have carrier concentrations that are far too large. However, if it is possible to reduce the carrier concentration of Zn-containing samples by doping with an *n*-type dopant,[104, 105] higher zT than that of Mn analogue could potentially be realized in future work.

-	$Yb_9Zn_{4.2}Sb_9$	$Yb_9Mn_{4.2}Sb_9$
Effective mass	0.65 m_e	1.2 m_e
Mobility parameter	18.95 $cm^2V^{-1}s^{-1}$	5.71 $cm^2V^{-1}s^{-1}$
Weighted mobility	9.94 WmK^{-1}	7.51 WmK^{-1}
Quality factor	0.445	0.328

Table 6.4: The parameters for the SPB model at 975 K. Lattice contribution to the thermal conductivity was calculated to be consistent with the total thermal conductivity.

6.8 Revisiting $Yb_9Zn_{4+y}Sb_9$

In Chapter 3, 4, and 5, we established and demonstrated an experimental concept we call phase boundary mapping to control defect formation energies of a target phase. In the case of $Yb_9Zn_{4+y}Sb_9$, whose structure is the same as $Ca_9Zn_{4+x}Sb_9$, either Yb vacancy or Zn deficiency can be primal candidates of stable defects (electron killer) preventing carrier density from being reduced. Thus, obtaining more Zn-rich or Ca-rich samples may lead to increasing formation energies of these undesired defects through increasing atomic chemical potentials, resulting in lowering carrier concentration. Based on the XRD result shown in Fig. 6.2(b), $YbZn_2Sb_2$ peaks appeared in the pattern of $Yb_9Zn_{4.5}Sb_9$ sample, while others don't have clear $YbZn_2Sb_2$ peaks. This indicates that the target 9-4-9 phase in $Yb_9Zn_{4.5}Sb_9$ sample is in different thermodynamic states from other three samples containing less amount of Zn, but the reduction of Zn deficiency is not sufficient to alter the electronic transport properties of the resulting sample. Therefore, full investigation of all accessible thermodynamic states is performed to examine if there are any states which can make the actual composition of 9-4-9 phase closer to charge balanced.

We first conducted DFT calculations to generate compositional and grand potential phase diagrams of Yb-Zn-Sb system to determine the accessible multi-phase regions. Fig. 6.8(a) shows the calculated Yb-Zn-Sb ternary phase diagram with all the stable compounds at 0K. As it can be seen in Fig. 6.8(a), there are five three-phase regions with no thermodynamic degrees of freedom around the target 9-4-9 phase.

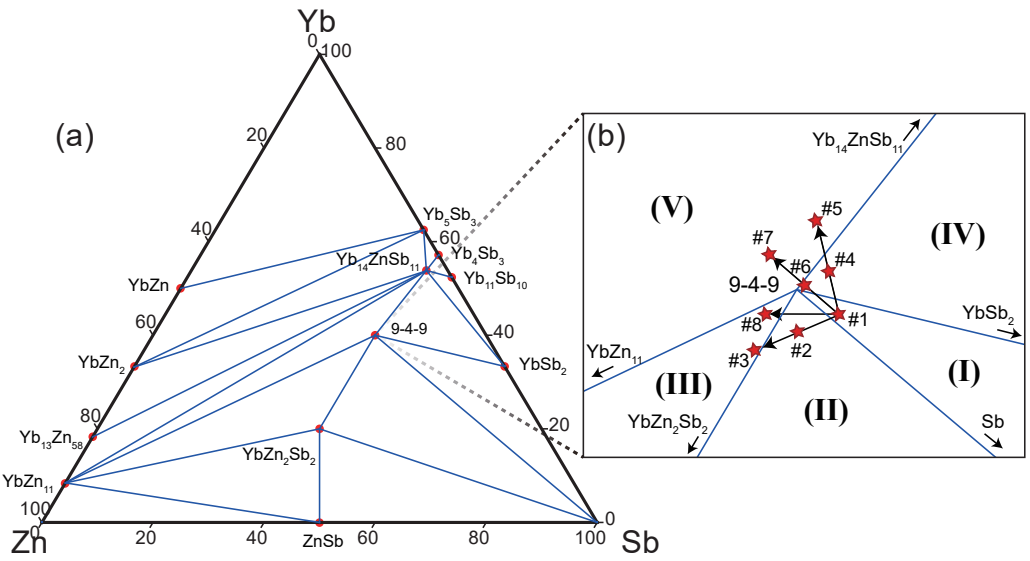

Figure 6.8: (a) Yb-Zn-Sb ternary phase diagram at 0 K constructed by DFT calculation and (b) the magnified region around the target 9-4-9 phase. There are five three-phase regions around this 9-4-9 and to access all the thermodynamic states of 9-4-9, multiple samples are synthesized with varied nominal compositions. Based on XRD, SEM, and transport properties, samples listed in table 6.5 belong to the phase region indicated in (b).

Sample number	Nominal Yb-Zn-Sb composition	zT at 750 K	phase region
#1	9 - 4.3 - 9	0.06	I
#2	9 - 4.5 - 9	0.09	II
#3	9 - 4.8 - 9	0.17	III
#4	9.2 - 4.3 - 9	0.06	IV
#5	9.5 - 4.3 - 9	0.30	V
#6	9 - 4.3 - 8.7	0.08	IV
#7	9 - 4.3 - 8.5	0.29	V
#8	9.3 - 4.6 - 9	0.18	III

Table 6.5: The sample numbers and their nominal composition, zT at 750 K, and most probable phase regions based on XRD, SEM, and transport properties.

To access all of these three-phase equilibria for the full investigation of this 9-4-9 phase, multiple samples with varied nominal compositions listed in table 6.5 were synthesized. Starting from a sample with nominal composition of $Yb_9Zn_{4.3}Sb_9$, we picked up four different directions to systematically explore different multi-phase equilibria: Zn-rich, Yb-rich, Sb-deficient, and Yb-Zn-rich directions (see Fig.6.8(b)). All samples were annealed for a week at 600 C to make sure samples are in equilibrium.

14-1-11 was found as a secondary phase in sample # 4-7, and 1-2-2 was found in sample #2, 3, and 8. Then, thermoelectric properties were measured to correlate the trend in measured properties to the thermodynamic states of samples. Based on the measured values, the predicted zT curve of 9-4-9 phase was obtained as shown in Fig. 6.9. The experimentally determined zT are the symbols in the figure. The trend in experimental zT is well captured by effective m^* model, which is a good indication of rigid electronic band structure. Comparing coexisting phases and measured transport properties, expected thermodynamic states of samples are listed as shown in table 6.5.

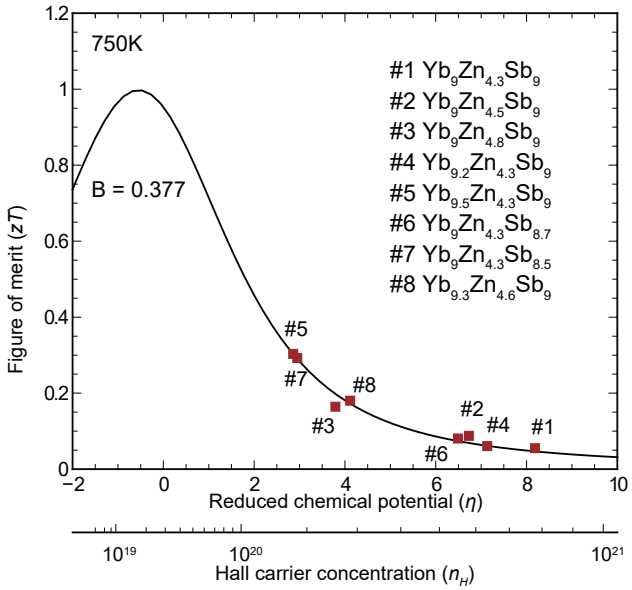

Figure 6.9: Predicted thermoelectric figure of merit zT curve within effective m* model at 750K (B = 0.377). Symbols are experimentally determined zT of 8 different samples.

The fact that the experimental zT values follow predicted curve fairly well also indicates that the secondary phases are not altering scattering and solely changes the carrier density although the less metallic samples of #5 and #7 contain a large amount of metallic 14-1-11. As a consequence, zT of sample #5 and #7 becomes about five times higher than that of #1.

6.9 Conclusion

The Zintl compound $Yb_9Mn_{4.2}Sb_9$ is a promising thermoelectric material due to its low, glass-like lattice thermal conductivity, essential for high zT. In this research, the effect of substituting Zn on the Mn site in $Yb_9Mn_{4.2-x}Zn_xSb_9$ was investigated.

Pursuing this strategy led to a factor of two reduction in the valence band mass, and thus increased carrier mobility and decreased Seebeck coefficients. The thermoelectric quality factor of the $Yb_9Mn_{4.2-x}Zn_xSb_9$ system was found to be somewhat higher in the Zn analogue due to its improved mobility. The carrier concentration in Zn-containing samples was too high, and varying the synthetic Zn content did not lead to desired carrier concentration control. On the other hand, phase boundary mapping revealed the thermodynamic states whose defect concentration is slightly lower, resulting in enhancing zT by a factor of five. There is still large room for zT enhancement, so in future studies *n*-type dopants might be able to be used to reduce the carrier concentration and achieve a higher figure of merit.

Appendix *A*: Basic thermodynamics for phase boundary mapping

Equilibrium conditions

When two substances are in a system and equilibrated, there are some conditions which are always satisfied. Consider α and β phases containing i different atom spices in a closed system. Assuming no interaction with outside, we have following relations:

$$\begin{aligned} V^\alpha + V^\beta = V = const., \quad dV^\alpha + dV^\beta = 0 \\ U^\alpha + U^\beta = U = const., \quad dU^\alpha + dU^\beta = 0 \\ n_i^\alpha + n_i^\beta = n_i = const., \quad dn_i^\alpha + dn_i^\beta = 0. \end{aligned} \tag{6.9}$$

In equilibrium, the total entropy of the system becomes maximum and remains constant,

$$dS = dS^\alpha + dS^\beta = 0. \tag{6.10}$$

In the case of closed system where there are multiple different substances, the fundamental thermodynamic relation for the change in the internal energy becomes

$$dU(S, V, n_i) = TdS - pdV + \sum_i \eta_i dn_i, \tag{6.11}$$

where i is an atom spices i, so

$$dS = \frac{1}{T}dU + \frac{p}{T}dV - \frac{1}{T}\sum_i \eta_i dn_i. \tag{6.12}$$

Therefore,

$$\begin{aligned} dS &= dS^\alpha + dS^\beta \\ &= \frac{dU^\alpha}{T^\alpha} + \frac{p^\alpha}{T^\alpha}dV^\alpha - \frac{1}{T^\alpha}\sum_i \mu_i^\alpha dn_i^\alpha + \frac{dU^\beta}{T^\beta} + \frac{p^\beta}{T^\beta}dV^\beta - \frac{1}{T^\beta}\sum_i \mu_i^\beta dn_i^\beta. \end{aligned} \tag{6.13}$$

With Eq. 6.9 and Eq. 6.10,

$$\left(\frac{1}{T^\alpha} - \frac{1}{T^\beta}\right)dU^\alpha - \left(\frac{p^\alpha}{T^\alpha} - \frac{p^\beta}{T^\beta}\right)dV^\alpha + \sum_i \left(\frac{\mu_i^\alpha}{T^\alpha} - \frac{\mu_i^\beta}{T^\beta}\right)dn_i^\alpha = 0. \tag{6.14}$$

Therefore,

$$\begin{aligned} T^\alpha &= T^\beta \\ p^\alpha &= p^\beta \\ \mu_i^\alpha &= \mu_i^\beta. \end{aligned} \tag{6.15}$$

This is the equilibrium condition that the two phases coexist in the closed system.

Gibbs phase rule

Change in Gibbs energy becomes following form under the constant temperature and pressure.

$$dG(T, p, n_i) = \sum_i \mu_i dn_i \tag{6.16}$$

Consider the total number of particle is fixed,

$$n^\alpha + n^\beta = n = const., \quad dn^\alpha + dn^\beta = 0. \tag{6.17}$$

Thus

$$dG = \mu^\alpha dn^\alpha + \mu^\beta dn^\beta = (\mu^\alpha - \mu^\beta) dn^\alpha \tag{6.18}$$

When the system is in equilibrium $dG = 0$. Thus $\mu^\alpha = \mu^\beta$. When $dG \neq 0$, the process has not reached the equilibrium (the difference in the chemical potentials is a driving force for the particle movement).

When there are P different phases and C different components, the equilibrium condition can be obtained as follows:

$$\begin{aligned}
T^\alpha &= T^\beta = T^\gamma = \cdots = T^P \\
p^\alpha &= p^\beta = p^\gamma = \cdots = p^P \\
\mu_1^\alpha &= \mu_1^\beta = \mu_1^\gamma = \cdots = \mu_1^P \\
\mu_2^\alpha &= \mu_2^\beta = \mu_2^\gamma = \cdots = \mu_2^P \\
&\cdots \\
&\cdots \\
\mu_C^\alpha &= \mu_C^\beta = \mu_C^\gamma = \cdots = \mu_C^P.
\end{aligned} \tag{6.19}$$

There are $(C+2)(P-1)$ equal signs and this is the number of constraints. According to the Gibbs-Duhem equation should be satisfied under the constant T and p for each phase, there are also P different constraint. Therefore the number of constraints is $(C + 2)(P - 1) + P$. On the other hand, the number of independent variables in each phase is the sum of the number of components + 2 (T and p). Thus, the total number of variables is $P(C + 2)$. Subtracting the number of constraints from the total number of independent variables, the degrees of freedom (F) can be obtained as follows:

$$\begin{aligned}
F &= (C + 2)P - [(C + 2)(P - 1) + P] \\
&= C - P + 2.
\end{aligned} \tag{6.20}$$

In solid, it is common to assume that two mixed phases have the same temperature and pressure from the beginning. If so,

$$\begin{aligned} F &= [CP + 2] - [C(P - 1) + P] \\ &= C - P + 2. \end{aligned} \tag{6.21}$$

Of course, the resulting relation becomes identical.

Point defect due to entropy

Any material cannot obtain the perfect crystal form (no point defect) due to entropy. Consider the simplest case where n vacancies form in a material with N atoms (n « N). Since a vacancy is created by moving an interior atom to the surface,[1] by defining a volume, entropy (primarily vibrational), and enthalpy associated with a formation of one vacancy as δ, S_v, and E_v, the Gibbs energy of a system at finite temperature T ($G(T)$) becomes

$$G(T) = G(0) + n(E_v + p\delta - TS_v) - TS_M, \tag{6.22}$$

where S_M is a configurational (mixing) entropy. Since there are n vacancies and N atoms, S_M becomes

$$S_M = k_B \ln {}^{N+n}C_n = k_B \ln \frac{(N+n)!}{N!n!}. \tag{6.23}$$

The most stable defect concentration is the n minimizing $G(T)$,

$$\left(\frac{dG}{dn}\right)_N = 0 = E_v + p\delta - TS_v + k_B T \ln\left(\frac{n}{N+n}\right). \tag{6.24}$$

Here we used Stirling's approximation. The vacancy concentration, $C = n/(N+n)$, is then calculated as

$$C = e^{-E_v/k_BT} e^{-p\delta/k_BT} e^{S_v/k_B}. \tag{6.25}$$

The latter two exponentials are very small compared to the effect from the first exponential, but the important information obtained from this result is that vacancy always exists in any systems at finite temperature. Fig. 6.10 shows a schematic diagram of contributions from each component (Formation enthalpy, vibrational entropy, and mixing enthalpy) to the total Gibbs energy. n_0 corresponds to the point defect concentration in equilibrium, which is always finite.

[1] Vacancy formation involves breaking bonds between atoms to remove an atom in the solid. In this sense, the process of forming vacancy is the same as vaporization. Thus, in the simple cases where there is only one constituent, the defect formation energy is roughly equal to the heat required for vaporization. In more complex solids, the electronegativity is one parameter to be considered.

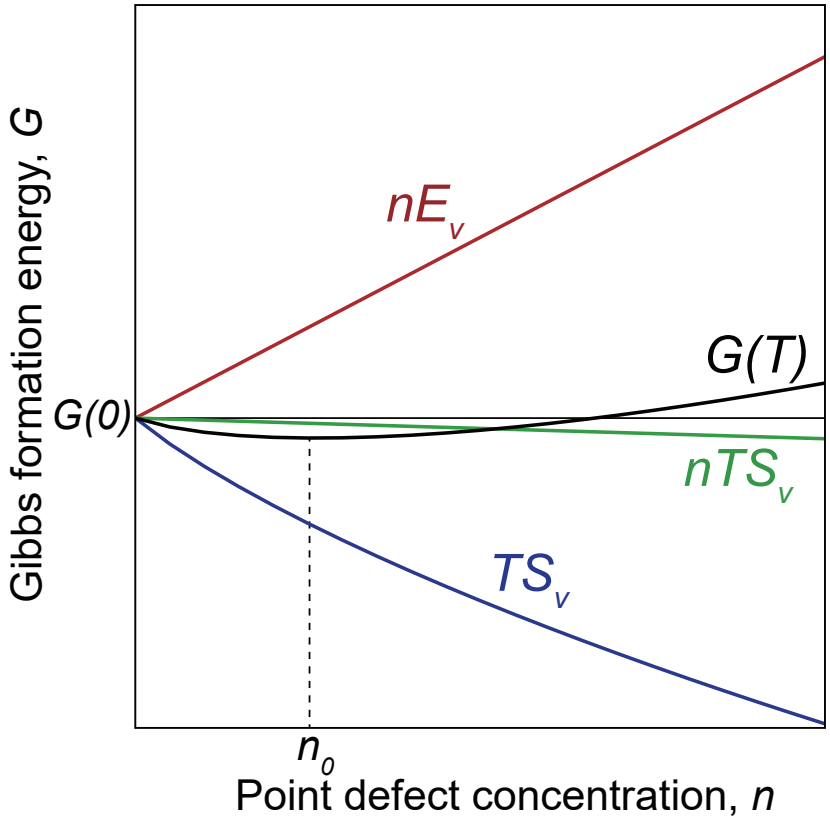

Figure 6.10: Schematic of each contributions to the total Gibbs energy as a function of point defect concentration. At finite temperature, there are always a curtain amount of point defects in a material due to entropy.

Bibliography

[1]E. Velmre, "Thomas Johann Seebeck and his contribution to the modern science and technology," in Electronics conference (bec), 2010 12th biennial baltic (IEEE, 2010), pp. 17–24.

[2]T. J. Seebeck, "Ueber die magnetische polarisation der metalle und erze durch temperatur-differenz," Annalen der Physik **82**, 133–160 (1826).

[3]J. Fourier and H. Oersted, "Sur quelques nouvelles experiences thermoelectriques," Ann. Chim. Phys, 375–389 (1823).

[4]J. Peltier, "Investigation of the heat developed by electric currents in homogeneous materials and at the junction of two different conductors," Ann. Chim. Phys **56**, 371 (1834).

[5]G. S. Ohm, *Die galvanische kette: mathematisch bearbeitet*, German (T.H. Riemann Berlin, 1827).

[6]T. C. Holgate, R. Bennett, T. Hammel, T. Caillat, S. Keyser, and B. Sievers, "Increasing the efficiency of the multi-mission radioisotope thermoelectric generator," Journal of Electronic Materials **44**, 1814–1821 (2015).

[7]L. R. Brown, "Building a sustainable society," Society **19**, 75–85 (1982).

[8]LLNL, *Lawrence Livermore National Laboratory: Energy Flow Charts*, `https://flowcharts.llnl.gov/commodities/energy`, [Accessed: 2017-04-13].

[9]T. C. Holgate, Y. Song, D. Shi, R. Utz, T. Chung, R. Bennett, S. Keyser, T. E. Hammel, R. Sievers, T. Caillat, et al., "Enhancement of the multi-mission radioisotope thermoelectric generator with efficient skutterudite thermoelectric couples: current status of the skutterudite technology maturation program," in 14th international energy conversion engineering conference (2016), p. 4817.

[10]S. K. Yee, S. LeBlanc, K. E. Goodson, and C. Dames, "$ per W metrics for thermoelectric power generation: beyond ZT," Energy Environ. Sci. **6**, 2561–2571 (2013).

[11]J. Martin, T. Tritt, and C. Uher, "High temperature Seebeck coefficient metrology," Journal of Applied Physics **108**, 14 (2010).

[12]A. V. Da Rosa, *Fundamentals of renewable energy processes* (Academic Press, 2012).

[13]A. F. Ioffe, L. Stil'bans, E. Iordanishvili, T. Stavitskaya, A. Gelbtuch, and G. Vineyard, "Semiconductor thermoelements and thermoelectric cooling," Physics Today **12**, 42 (1959).

[14]H. J. Goldsmid, *Introduction to thermoelectricity* (Springer, 2009).

[15]D. M. Rowe, *Crc handbook of thermoelectrics* (CRC press, 1995).

[16]D. M. Rowe and C. M. Bhandari, *Modern thermoelectrics* (Prentice Hall, 1983).

[17]C. Goupil, W. Seifert, K. Zabrocki, E. Müller, and G. J. Snyder, "Thermodynamics of thermoelectric phenomena and applications," Entropy **13**, 1481–1517 (2011).

[18]L. D. Zhao, S. H. Lo, Y. Zhang, H. Sun, G. Tan, C. Uher, C. Wolverton, V. P. Dravid, and M. G. Kanatzidis, "Ultralow thermal conductivity and high thermoelectric figure of merit in snse crystals," Nature **508**, 373–7 (2014).

[19]P.-C. Wei, S. Bhattacharya, J. He, S. Neeleshwar, R. Podila, Y. Y. Chen, and A. M. Rao, "The intrinsic thermal conductivity of snse," Nature **539**, E1–E2 (2016).

[20]G. J. Snyder and T. S. Ursell, "Thermoelectric efficiency and compatibility," Physical review letters **91**, 148301 (2003).

[21]B. B. Iversen, *First came the material*, `http://batteriselskab.dk/event/presentation/first-came-the-material.htm`, [Accessed: 2017-04-23].

[22]G. J. Snyder and E. S. Toberer, "Complex thermoelectric materials," Nature Mater. **7**, 105–114 (2008).

[23]A. F. May and G. J. Snyder, "Introduction to modeling thermoelectric transport at high temperatures," in *Materials, preparation, and characterization in thermoelectrics* (CRC Press, 2012), pp. 1–18.

[24]H. Wang, Y. Pei, A. D. LaLonde, and G. J. Snyder, "Materials design based on the thermoelectric quality factor," in *Thermoelectric nanomaterials*, edited by K. Koumoto and T. Mori (Springer, 2013) Chap. 1, pp. 3–32.

[25]S. D. Kang and G. J. Snyder, "Charge-transport model for conducting polymers," Nature Materials (2016).

[26]Z. M. Gibbs, F. Ricci, G. Li, H. Zhu, K. Persson, G. Ceder, G. Hautier, A. Jain, and G. J. Snyder, "Effective mass and fermi surface complexity factor from ab initio band structure calculations," npj Computational Materials **3**, 8 (2017).

[27]B. M. Askerov, *Electron transport phenomena in semiconductors* (World scientific, 1994).

[28]A. Zevalkink, E. S. Toberer, W. G. Zeier, E. Flage-Larsen, and G. J. Snyder, "Ca_3AlSb_3: an inexpensive, non-toxic thermoelectric material for waste heat recovery," Energy & Environmental Science **4**, 510 (2011).

[29]A. Zevalkink, J. Swallow, S. Ohno, U. Aydemir, S. Bux, and G. J. Snyder, "Thermoelectric properties of the $Ca_5Al_{2-x}In_xSb_6$ solid solution," Dalton Transactions **43**, 15872–15878 (2014).

[30]S. K. Bux, A. Zevalkink, O. Janka, D. Uhl, S. Kauzlarich, J. G. Snyder, and J.-P. Fleurial, "Glass-like lattice thermal conductivity and high thermoelectric efficiency in $Yb_9Mn_{4.2}Sb_9$," Journal of Materials Chemistry A **2**, 215–220 (2014).

[31]S. Ohno, A. Zevalkink, Y. Takagiwa, S. K. Bux, and G. J. Snyder, "Thermoelectric properties of the $Yb_9Mn_{4.2-x}Zn_xSb_9$ solid solutions," Journal of Materials Chemistry A **2**, 7478–7483 (2014).

[32]S. Ohno, U. Aydemir, M. Amsler, J.-H. Pöhls, S. Chanakian, A. Zevalkink, M. A. White, S. K. Bux, C. Wolverton, and G. J. Snyder, "Achieving $zT > 1$ in inexpensive Zintl phase $Ca_9Zn_{4+x}Sb_9$ by phase boundary mapping," Advanced Functional Materials **In press** (2017) 10.1002/adfm.201606361.

[33]A. May, J.-P. Fleurial, and G. Snyder, "Thermoelectric performance of lanthanum telluride produced via mechanical alloying," Physical Review B **78** (2008) 10.1103/PhysRevB.78.125205.

[34]A. May, E. Toberer, A. Saramat, and G. Snyder, "Characterization and analysis of thermoelectric transport in n-type $Ba_8Ga_{16-x}Ge_{30+x}$," Physical Review B **80** (2009) 10.1103/PhysRevB.80.125205.

[35]P. H. M. Böttger, G. S. Pomrehn, G. J. Snyder, and T. G. Finstad, "Doping of p-type ZnSb: single parabolic band model and impurity band conduction," physica status solidi (a) **208**, 2753–2759 (2011).

[36]G. D. Mahan, "Good thermoelectrics," in *Solid state phys.* Vol. 51 (1998).

[37]R. P. Chasmar and R. Stratton, "The thermoelectric figure of merit and its relation to thermoelectric generators," Journal of Electronics and Control **7**, 52–72 (1959).

[38]P. Gorai, D. Gao, B. Ortiz, S. Miller, S. A. Barnett, T. Mason, Q. Lv, V. Stevanović, and E. S. Toberer, "TE Design Lab: a virtual laboratory for thermoelectric material design," Computational Materials Science **112**, 368–376 (2016).

[39]H. Wang, Y. Pei, A. D. LaLonde, and G. J. Snyder, "Weak electron-phonon coupling contributing to high thermoelectric performance in n-type PbSe," Proceedings of the National Academy of Sciences **109**, 9705–9709 (2012).

[40]Y. Pei, X. Shi, A. LaLonde, H. Wang, L. Chen, and G. J. Snyder, "Convergence of electronic bands for high performance bulk thermoelectrics," Nature **473**, 66–9 (2011).

[41]Y. Pei, H. Wang, and G. J. Snyder, "Band engineering of thermoelectric materials," Advanced Materials **24**, 6125–6135 (2012).

[42]H.-S. Kim, N. A. Heinz, Z. M. Gibbs, Y. Tang, S. D. Kang, and G. J. Snyder, "High thermoelectric performance in $(Bi_{0.25}Sb_{0.75})_2Te_3$ due to band convergence and improved by carrier concentration control," Submitted (2017).

[43]W. Li, L. Zheng, B. Ge, S. Lin, X. Zhang, Z. Chen, Y. Chang, and Y. Pei, "Promoting SnTe as an eco-friendly solution for p-PbTe thermoelectric via band convergence and interstitial defects," Advanced Materials (2017).

[44]W. Liu, X. Tan, K. Yin, H. Liu, X. Tang, J. Shi, Q. Zhang, and C. Uher, "Convergence of conduction bands as a means of enhancing thermoelectric performance of *n*-type $Mg_2Si_{1-x}Sn_x$ solid solutions," Phys. Rev. Lett. **108**, 166601 (2012).

[45]Y. Tang, Z. M. Gibbs, L. A. Agapito, G. Li, H.-S. Kim, M. B. Nardelli, S. Curtarolo, and G. J. Snyder, "Convergence of multi-valley bands as the electronic origin of high thermoelectric performance in $CoSb_3$ skutterudites," Nat Mater **14**, 1223–1228 (2015).

[46]C. Fu, T. Zhu, Y. Pei, H. Xie, H. Wang, G. J. Snyder, Y. Liu, Y. Liu, and X. Zhao, "High band degeneracy contributes to high thermoelectric performance in p-type Half-Heusler compounds," Advanced Energy Materials **4**, 1400600 (2014).

[47]H. Tamaki, H. K. Sato, and T. Kanno, "Isotropic conduction network and defect chemistry in $Mg_{3+\delta}Sb_2$-based layered Zintl compounds with high thermoelectric performance," Adv Mater **28**, 10182–10187 (2016).

[48]J. Zhang, L. Song, S. H. Pedersen, H. Yin, L. T. Hung, and B. B. Iversen, "Discovery of high-performance low-cost *n*-type Mg_3Sb_2-based thermoelectric materials with multi-valley conduction bands," Nat Commun **8**, 13901 (2017).

[49]H. Zhu, G. Hautier, U. Aydemir, Z. M. Gibbs, G. Li, S. Bajaj, J.-H. Pöhls, D. Broberg, W. Chen, A. Jain, et al., "Computational and experimental investigation of $TmAgTe_2$ and XYZ_2 compounds, a new group of thermoelectric materials identified by first-principles high-throughput screening," Journal of Materials Chemistry C **3**, 10554–10565 (2015).

[50]B. R. Ortiz, P. Gorai, L. Krishna, R. Mow, A. Lopez, R. W. McKinney, V. Stevanović, and E. Toberer, "Potential for high thermoelectric performance in *n*-type Zintl compounds: a case study of Ba doped $KAlSb_4$," Journal of Materials Chemistry A (2017) 10.1039/C6TA09532A.

[51]V. I. Fistul, *Heavily doped semiconductors* (Plenum Press, 1969).

[52]M. Lundstrom, *Fundamentals of carrier transport* (Cambridge University Press, 2009).

[53]E. S. Toberer, A. Zevalkink, and G. J. Snyder, "Phonon engineering through crystal chemistry," J. Mater. Chem. **21**, 15843 (2011).

[54]O. Delaire, J. Ma, K. Marty, A. F. May, M. A. McGuire, M.-H. Du, D. J. Singh, A. Podlesnyak, G. Ehlers, M. Lumsden, et al., "Giant anharmonic phonon scattering in PbTe," Nature materials **10**, 614–619 (2011).

[55]Y. Zhang, E. Skoug, J. Cain, V. Ozolins, D. Morelli, and C. Wolverton, "First-principles description of anomalously low lattice thermal conductivity in thermoelectric Cu-Sb-Se ternary semiconductors," Physical Review B **85** (2012) 10.1103/PhysRevB.85.054306.

[56]C. W. Li, J. Hong, A. F. May, D. Bansal, S. Chi, T. Hong, G. Ehlers, and O. Delaire, "Orbitally driven giant phonon anharmonicity in SnSe," Nature Physics **11**, 1063–1069 (2015).

[57]S. A. Miller, P. Gorai, B. R. Ortiz, A. Goyal, D. Gao, S. A. Barnett, T. O. Mason, G. J. Snyder, Q. Lv, V. Stevanović, and E. S. Toberer, "Capturing anharmonicity in a lattice thermal conductivity model for high-throughput predictions," Chemistry of Materials **29**, 2494–2501 (2017).

[58]C. Kittel, *Introduction to solid state physics* (Wiley and Sons, 2004).

[59]N. W. Ashcroft, N. D. Mermin, and S. Rodriguez, *Solid state physics*, 1978.

[60]H. Ibach, *Physics of surfaces and interfaces*, Vol. 12 (Springer, 2006).

[61]J. Callaway and H. C. von Baeyer, "Efiect of point imperfections on lattice thermal conductivity," Phys. Rev. **120** (1960).

[62]J. Yang, G. P. Meisner, and L. Chen, "Strain field fluctuation effects on lattice thermal conductivity of ZrNiSn-based thermoelectric compounds," Applied Physics Letters **85**, 1140–1142 (2004).

[63]J. Shuai, Z. Liu, H. S. Kim, Y. Wang, J. Mao, R. He, J. Sui, and Z. Ren, "Thermoelectric properties of Bi-based Zintl compounds $Ca_{1-x}Yb_xMg_2Bi_2$," J. Mater. Chem. A **4**, 4312–4320 (2016).

[64]H. Xie, H. Wang, Y. Pei, C. Fu, X. Liu, G. J. Snyder, X. Zhao, and T. Zhu, "Beneficial contribution of alloy disorder to electron and phonon transport in half-heusler thermoelectric materials," Advanced Functional Materials **23**, 5123–5130 (2013).

[65]P. G. Klemens, "Thermal resistance due to point defects at high temperatures," Physical Review **119**, 507–509 (1960).

[66]B. Abeles, D. S. Beers, G. D. Cody, and J. P. Dismukes, "Thermal conductivity of ge-si alloys at high temperature," Phys. Rev. **125**, 44–46 (1962).

[67]H. Wang, A. D. LaLonde, Y. Pei, and G. J. Snyder, "The criteria for beneficial disorder in thermoelectric solid solutions," Advanced Functional Materials **23**, 1586–1596 (2013).

[68]Z. Wang, J. E. Alaniz, W. Jang, J. E. Garay, and C. Dames, "Thermal conductivity of nanocrystalline silicon: importance of grain size and frequency-dependent mean free paths," Nano letters **11**, 2206–2213 (2011).

[69]S. K. Bux, R. G. Blair, P. K. Gogna, H. Lee, G. Chen, M. S. Dresselhaus, R. B. Kaner, and J.-P. Fleurial, "Nanostructured bulk silicon as an effective thermoelectric material," Advanced Functional Materials **19**, 2445–2452 (2009).

[70]P. G. Klemens and M. Gell, "Thermal conductivity of thermal barrier coatings," Materials Science and Engineering **A245**, 143–149 (1998).

[71]C. B. Vining, "Thermoelectric properties of pressure-sintered $Si_{0.8}Ge_{0.2}$ thermoelectric alloys," J. Appl. Phys **69**, 4333–4340 (1991).

[72]P. G. Klemens, *Thermal conductivity and lattice vibrational modes*, Solid State Physics (1958).

[73]H.-S. Kim, S. D. Kang, Y. Tang, R. Hanus, and G. J. Snyder, "Dislocation strain as the mechanism of phonon scattering at grain boundaries," Materials Horizons **3**, 234–240 (2016).

[74]P. G. Klemens, "The scattering of low-frequency lattice waves by static imperfections," Proc. Phys. Soc. A **68**, 1113–1127 (1955).

[75]Z. Chen, B. Ge, W. Li, S. Lin, J. Shen, Y. Chang, R. Hanus, G. J. Snyder, and Y. Pei, "Vacancy-induced dislocations within grains for high-performance PbSe thermoelectrics," Nature Communications **8** (2017).

[76]Z. Chen, Z. Jian, W. Li, Y. Chang, B. Ge, R. Hanus, J. Yang, Y. Chen, M. Huang, G. J. Snyder, and Y. Pei, "Lattice dislocations enhancing thermoelectric PbTe in addition to band convergence," Advanced Materials, 1606768 (2017).

[77]G. S. Pomrehn, A. Zevalkink, W. G. Zeier, A. van de Walle, and G. J. Snyder, "Defect-controlled electronic properties in $A\mathrm{Zn_2Sb_2}$ Zintl phases," Angew Chem Int Ed Engl **53**, 3422–6 (2014).

[78]J. Shuai, Y. Wang, Z. Liu, H. S. Kim, J. Mao, J. Sui, and Z. Ren, "Enhancement of thermoelectric performance of phase pure Zintl compounds $\mathrm{Ca_{1-x}Yb_xZn_2Sb_2}$, $\mathrm{Ca_{1-x}Eu_xZn_2Sb_2}$, and $\mathrm{Eu_{1-x}Yb_xZn_2Sb_2}$ by mechanical alloying and hot pressing," Nano Energy **25**, 136–144 (2016).

[79]A. F. May, M. A. McGuire, J. Ma, O. Delaire, A. Huq, and R. Custelcean, "Properties of single crystalline $A\mathrm{Zn_2Sb_2}$ (A = Ca, Eu, Yb)," Journal of Applied Physics **111**, 033708 (2012).

[80]E. S. Toberer, A. F. May, B. C. Melot, E. Flage-Larsen, and G. J. Snyder, "Electronic structure and transport in thermoelectric compounds $\mathrm{AZn_2Sb_2}$ (A = Sr, Ca, Yb, Eu)," Dalton Trans **39**, 1046–54 (2010).

[81]J. Shuai, H. Geng, Y. Lan, Z. Zhu, C. Wang, Z. Liu, J. Bao, C. W. Chu, J. Sui, and Z. Ren, "Higher thermoelectric performance of Zintl phases $\mathrm{(Eu_{0.5}Yb_{0.5})_{1-x}Ca_xMg_2Bi_2}$ by band engineering and strain fluctuation," Proc Natl Acad Sci **113**, E4125–32 (2016).

[82]E. Zintl and E. Husemann, "Bindungsart und gitterbau binaerer magnesiumverbindungen. (12. mitteilung ueber metalle und legierungen)," Z. phys. Chem. **21**, 138 (1933).

[83]E. Zintl, "Intermetallische verbindungen," Angewandte Chemie **52**, 1–6 (1939).

[84]E. Zintl and G. Woltersdorf, "Lattice structure of lial," Z. Electrochem. B **41**, 876 (1935).

[85]H. Schäfer, B. Eisenmann, and W. Müller, "Zintl Phases: transitions between metallic and ionic bonding," Angewandte Chemie International Edition in English **12**, 694–712 (1973).

[86]S. M. Kauzlarich, A. Zevalkink, E. Toberer, and G. J. Snyder, "Chapter 1 Zintl Phases: recent developments in thermoelectrics and future outlook," 1–26 (2017).

[87]S. M. Kauzlarich, *Chemistry, structure, and bonding of Zintl phases and ions* (Wiley-VCH, 1996).

[88]H. Schäfer, "On the problem of polar intermetallic compounds: the stimulation of E. Zintl's work for the modern chemistry of intermetallics," Annual Review of Materials Science **15**, 1–42 (1985).

[89]E. S. Toberer, A. F. May, and G. J. Snyder, "Zintl chemistry for designing high efficiency thermoelectric materials," Chemistry of Materials **22**, 624–634 (2010).

[90]B. C. Sales, D. Mandrus, and R. K. Williams, "Filled skutterudite antimonides: A new class of thermoelectric materials," Science **272**, 1325–1328 (1996).

[91]S. K. Bux, M. T. Yeung, E. S. Toberer, G. J. Snyder, R. B. Kaner, and J.-P. Fleurial, "Mechanochemical synthesis and thermoelectric properties of high quality magnesium silicide," Journal of Materials Chemistry **21**, 12259–12266 (2011).

[92]M. Akasaka, T. Iida, A. Matsumoto, K. Yamanaka, Y. Takanashi, T. Imai, and N. Hamada, "The thermoelectric properties of bulk crystalline *n*-and *p*-type Mg_2Si prepared by the vertical bridgman method," Journal of Applied Physics **104**, 013703 (2008).

[93]G. J. Snyder, M. Christensen, E. Nishibori, T. Caillat, and B. B. Iversen, "Disordered zinc in Zn_4Sb_3 with phonon-glass and electron-crystal thermoelectric properties," Nat Mater **3**, 458–463 (2004).

[94]E. S. Toberer, P. Rauwel, S. Gariel, J. Taftø, and G. J. Snyder, "Composition and the thermoelectric performance of $\beta - Zn_4Sb_3$," Journal of materials chemistry **20**, 9877–9885 (2010).

[95]A. F. May, D. J. Singh, and G. J. Snyder, "Influence of band structure on the large thermoelectric performance of lanthanum telluride," Phys. Rev. B B **79**, 153101 (2009).

[96]T. Vo, P. von Allmen, C.-K. Huang, J. Ma, S. Bux, and J.-P. Fleurial, "Electronic and thermoelectric properties of Ce_3Te_4 and La_3Te_4 computed with density functional theory with on-site coulomb interaction correction," Journal of Applied Physics **116**, 133701 (2014).

[97]H. Zhang, H. Borrmann, N. Oeschler, C. Candolfi, W. Schnelle, M. Schmidt, U. Burkhardt, M. Baitinger, J.-T. Zhao, and Y. Grin, "Atomic interactions in the p-type clathrate I $Ba_8Au_{5.3}Ge_{40.7}$," Inorganic Chemistry **50**, 1250–1257 (2011).

[98]Y. Takasu, T. Hasegawa, N. Ogita, M. Udagawa, M. Avila, K. Suekuni, and T. Takabatake, "Off-center rattling and cage vibration of the carrier-tuned type-I clathrate $Ba_8Ga_{16}Ge_{30}$ studied by raman scattering," Physical Review B **82** (2010) 10.1103/PhysRevB.82.134302.

[99]Y. Saiga, B. Du, S. K. Deng, K. Kajisa, and T. Takabatake, "Thermoelectric properties of type-VIII clathrate $Ba_8Ga_{16}Sn_{30}$ doped with Cu," Journal of Alloys and Compounds **537**, 303–307 (2012).

[100]A. Zevalkink, G. Pomrehn, Y. Takagiwa, J. Swallow, and G. J. Snyder, "Thermoelectric properties and electronic structure of the Zintl-phase Sr_3AlSb_3," ChemSusChem **6**, 2316–21 (2013).

[101]A. Zevalkink, W. G. Zeier, G. Pomrehn, E. Schechtel, W. Tremel, and G. J. Snyder, "Thermoelectric properties of Sr_3GaSb_3 - a chain-forming Zintl compound," Energ. Environ. Sci. **5**, 9121 (2012).

[102]U. Aydemir, A. Zevalkink, A. Ormeci, H. Wang, S. Ohno, S. Bux, and G. J. Snyder, "Thermoelectric properties of the Zintl phases $Yb_5M_2Sb_6$ (M = Al, Ga, In)," Dalton Transactions **44**, 6767–6774 (2015).

[103]S. Brown, S. Kauzlarich, F. Gascoin, and G. J. Snyder, "$Yb_{14}MnSb_{11}$: New high efficiency thermoelectric material for power generation," Chemistry of Materials **18**, 1873–1877 (2006).

[104]E. S. Toberer, S. R. Brown, T. Ikeda, S. M. Kauzlarich, and G. Jeffrey Snyder, "High thermoelectric efficiency in lanthanum doped $Yb_{14}MnSb_{11}$," Applied Physics Letters **93**, 062110 (2008).

[105]E. S. Toberer, C. A. Cox, S. R. Brown, T. Ikeda, A. F. May, S. M. Kauzlarich, and G. J. Snyder, "Traversing the metal-insulator transition in a Zintl phase: rational enhancement of thermoelectric efficiency in $Yb_{14}Mn_{1-x}Al_xSb_{11}$," Advanced Functional Materials **18**, 2795–2800 (2008).

[106]J. H. Grebenkemper, Y. Hu, D. Barrett, P. Gogna, C.-K. Huang, S. K. Bux, and S. M. Kauzlarich, "High temperature thermoelectric properties of $Yb_{14}MnSb_{11}$ prepared from reaction of MnSb with the elements," Chemistry of Materials **27**, 5791–5798 (2015).

[107]Y. Hu, J. Wang, A. Kawamura, K. Kovnir, and S. M. Kauzlarich, "$Yb_{14}MgSb_{11}$ and $Ca_{14}MgSb_{11}$ - new Mg-containing Zintl compounds and their structures, bonding, and thermoelectric properties," Chemistry of Materials **27**, 343–351 (2015).

[108]N. Kazem, J. V. Zaikina, S. Ohno, G. J. Snyder, and S. M. Kauzlarich, "Coinage-metal-stuffed $Eu_9Cd_4Sb_9$: metallic compounds with anomalous low thermal conductivities," Chemistry of Materials **27**, 7508–7519 (2015).

[109]A. Zevalkink, E. S. Toberer, T. Bleith, E. Flage-Larsen, and G. J. Snyder, "Improved carrier concentration control in Zn-doped $Ca_5Al_2Sb_6$," Journal of Applied Physics **110**, 013721 (2011).

[110]S. Chanakian, U. Aydemir, A. Zevalkink, Z. M. Gibbs, J.-P. Fleurial, S. Bux, and G. J. Snyder, "High temperature thermoelectric properties of Zn-doped $Eu_5In_2Sb_6$," Journal of Materials Chemistry C **3**, 10518–10524 (2015).

[111]F. Gascoin, S. Ottensmann, D. Stark, M. S. Haile, and G. Snyder, "Zintl phases as thermoelectric materials: tuned transport properties of the compounds $Ca_xYb_{1-x}Zn_2Sb_2$," Adv. Funct. Mater. **15**, 1860–1864 (2005).

[112]X.-J. Wang, M.-B. Tang, H.-H. Chen, X.-X. Yang, J.-T. Zhao, U. Burkhardt, and Y. Grin, "Synthesis and high thermoelectric efficiency of Zintl phase $YbCd_{2-x}Zn_xSb_2$," Applied Physics Letters **94**, 092106 (2009).

[113]H. Zhang, L. Fang, M.-B. Tang, H.-H. Chen, X.-X. Yang, X. Guo, J.-T. Zhao, and Y. Grin, "Synthesis and properties of $CaCd_2Sb_2$ and $EuCd_2Sb_2$," Intermetallics **18**, 193–198 (2010).

[114]S. Chanakian, R. Weber, U. Aydemir, A. Ormeci, J.-P. Fleurial, S. Bux, and G. J. Snyder, "High temperature electronic and thermal transport properties of $EuGa_{2-x}In_xSb_2$," Journal of Electronic Materials, 1–7 (2017).

[115]N. Kazem and S. M. Kauzlarich, "Chapter 288 - thermoelectric properties of Zintl antimonides," in *Handbook on the physics and chemistry of rare earths*, Vol. Volume 50, edited by G. B. Jean-Claude and K. P. Vitalij (Elsevier, 2016), pp. 177–208.

[116]A. Zevalkink, U. Aydemir, and G. J. Snyder, "Chapter 11 Chain-Forming A_3MPn_3 and $A_5M_2Pn_6$ Zintl phases," in *Materials aspect of thermoelectricity* (CRC Press, 2016), pp. 385–404.

[117]S.-Q. Xia and S. Bobev, "Interplay between size and electronic effects in determining the homogeneity range of the $A_9Zn_{4+x}Pn_9$ and $A_9Cd_{4+x}Pn_9$ phases, A = Ca, Sr, Yb, Eu; Pn = Sb, Bi," J. Am. Chem. Soc **129**, 10011–10018 (2007).

[118]S.-Q. Xia and S. Bobev, "New manganese-bearing antimonides and bismuthides with complex structures. synthesis, structural characterization, and electronic properties of $Yb_9Mn_{4+x}Pn_9$ (Pn = Sb or Bi)," Chemistry of Materials **22**, 840–850 (2009).

[119]E. Flage-Larsen, Ø. Prytz, E. S. Toberer, and A. F. May, "Valence band study of thermoelectric Zintl-phase $SrZn_2Sb_2$ and $YbZn_2Sb_2$: X-ray photoelectron spectroscopy and density functional theory," Physical Review B **81**, 205204 (2010).

[120]A. F. May, M. A. McGuire, D. J. Singh, R. Custelcean, and J. Jellison G. E., "Structure and properties of single crystalline $CaMg_2Bi_2$, $EuMg_2Bi_2$, and $YbMg_2Bi_2$," Inorg Chem **50**, 11127–33 (2011).

[121]J. Shuai, Y. Wang, H. S. Kim, Z. Liu, J. Sun, S. Chen, J. Sui, and Z. Ren, "Thermoelectric properties of Na-doped Zintl compound: $Mg_{3-x}Na_xSb_2$," Acta Materialia **93**, 187–193 (2015).

[122]Q.-G. Cao, H. Zhang, M.-B. Tang, H.-H. Chen, X.-X. Yang, Y. Grin, and J.-T. Zhao, "Zintl phase $Yb_{1-x}Ca_xCd_2Sb_2$ with tunable thermoelectric properties induced by cation substitution," Journal of Applied Physics **107**, 053714 (2010).

[123]C. Yu, T. J. Zhu, S. N. Zhang, X. B. Zhao, J. He, Z. Su, and T. M. Tritt, "Improved thermoelectric performance in the Zintl phase compounds $YbZn_{2-x}Mn_xSb_2$ via isoelectronic substitution in the anionic framework," J. Appl. Phys **104**, 013705 (2008).

[124]H. Zhang, M. Baitinger, M. B. Tang, Z. Y. Man, H. H. Chen, X. X. Yang, Y. Liu, L. Chen, Y. Grin, and J. T. Zhao, "Thermoelectric properties of $Eu(Zn_{1-x}Cd_x)_2Sb_2$," Dalton Trans **39**, 1101–4 (2010).

[125]H. Zhang, L. Fang, M. B. Tang, Z. Y. Man, H. H. Chen, X. X. Yang, M. Baitinger, Y. Grin, and J. T. Zhao, "Thermoelectric properties of $yb_xeu_{1-x}cd_2sb_2$," J Chem Phys **133**, 194701 (2010).

[126]K. Guo, Q.-G. Cao, X.-J. Feng, M.-B. Tang, H.-H. Chen, X. Guo, L. Chen, Y. Grin, and J.-T. Zhao, "Enhanced thermoelectric figure of merit of Zintl phase $YbCd_{2-x}Mn_xSb_2$ by chemical substitution," European Journal of Inorganic Chemistry **26**, 4043–4048 (2011).

[127]I. Schellenberg, M. Eul, W. Hermes, and R. Pöttgen, "A 121Sb and 151Eu mössbauer spectroscopic investigation of $EuMn_2Sb_2$, $EuZn_2Sb_2$, $YbMn_2Sb_2$, and $YbZn_2Sb_2$," Zeitschrift für anorganische und allgemeine Chemie **636**, 85–93 (2010).

[128]A. May, M. McGuire, D. Singh, J. Ma, O. Delaire, A. Huq, W. Cai, and H. Wang, "Thermoelectric transport properties of $CaMg_2Bi_2$, $EuMg_2Bi_2$, and $YbMg_2Bi_2$," Physical Review B **85**, 035202 (2012).

[129]K. Kihou, H. Nishiate, A. Yamamoto, and C.-H. Lee, "Thermoelectric properties of As-based Zintl compounds $Ba_{1-x}K_xZn_2As_2$," Inorganic Chemistry **56**, PMID: 28252946, 3709–3712 (2017).

[130]P. Klüfers and A. Mewis, "AB_2X_2 compounds with $CaAl_2Si_2$ structure. 3. crystal-structure of $CaZn_2P_2$, $CaCd_2P_2$, $CaZn_2As_2$, and $CaCd_2As_2$," Zeitschrift für Naturforschung B **32**, 753–756 (1977).

[131]R. Hermann, F. Grandjean, S. Kauzlarich, J. Jiang, and S. Brown, "A Europium-151 Mo1ssbauer spectral study of $Eu_{14}MnP_{11}$, $Eu_{14}MnAs_{11}$, and $Eu_{14}MnSb_{11}$," Inorg. Chem. **43**, 7005–7013 (2004).

[132]H. Kim, "Neutron diffraction study of the ternary transition metal Zintl compound $Ca_{14}MnSb_{11}$," Journal of Solid State Chemistry **168**, 162–168 (2002).

[133]A. Rehr, T. Y. Kuromoto, S. Kauzlarich, J. D. Castillo, and D. J. Webb, "Structure and properties of the transition-metal Zintl compounds $A_{14}MnPn_{11}$ (A = Ca, Sr, Ba; Pn = As, Sb)," Chem. Mater. **6** (1994).

[134]R. A. Ribeiro, Y. Hadano, S. Narazu, K. Suekuni, M. A. Avila, and T. Takabatake, "Low-temperature thermoelectric properties of $Yb_{14}MSb_{11}$ (M = Mn, Zn)," Journal of Physics: Condensed Matter **19**, 376211 (2007).

[135]K. Star, A. Zevalkink, C.-K. Huang, B. Dunn, and J. P. Fleurial, "Synthesis and thermoelectric properties of doped $Yb_{14}MnSb_{11-x}Bi_x$ Zintls," **1267**, 1267–DD03 (2010).

[136]C. A. Uvarov, F. Ortega-Alvarez, and S. M. Kauzlarich, "Enhanced high-temperature thermoelectric performance of $Yb_{14-x}Ca_xMnSb_{11}$," Inorg Chem **51**, 7617–24 (2012).

[137]W.-J. Tan, Y.-T. Liu, M. Zhu, T.-J. Zhu, X.-B. Zhao, X.-T. Tao, and S.-Q. Xia, "Structure, magnetism, and thermoelectric properties of magnesium-containing antimonide Zintl phases $Sr_{14}MgSb_{11}$ and $Eu_{14}MgSb_{11}$," Inorganic Chemistry **56**, PMID: 28072534, 1646–1654 (2017).

[138]A. Zevalkink, G. S. Pomrehn, S. Johnson, J. Swallow, Z. M. Gibbs, and G. J. Snyder, "Influence of the triel elements (M = Al, Ga, In) on the transport properties of $Ca_5M_2Sb_6$ Zintl compounds," Chemistry of Materials **24**, 2091–2098 (2012).

[139]G. Cordier, H. Schafer, and M. Stelter, "Perantimonidogallate und -indate: Zur Kenntnis von $Ca_5Al_2Sb_6$, $Ca_5In_2Sb_6$, $Sr_5In_2Sb_6$," Z. Naturforsch., B **33**, 5–8 (1986).

[140]G. Cordier and M. Stelter, "$Sr_5Al_2Sb_6$ und $Ba_5In_2Sb_6$: Zwei neue Zintlphasen mit unterschiedlichen Baenderanionen," Z. Naturforsch **43b**, 463–466 (1988).

[141]G. Cordier, H. Schaefer, and M. Stelter, "Ca_3AlSb_3 und $Ca_5Al_2Bi_6$, zwie neue zintlphasen mit kettenförmigen anionen," Z. Naturforsch **39b**, 727–732 (1984).

[142]Y. L. Yan and Y. X. Wang, "High thermoelectric performance of $Ca_5Ga_2As_6$ as a Zintl compound," (2011).

[143]X.-C. Liu, Z. Wu, S.-Q. Xia, X.-T. Tao, and S. Bobev, "Structural variability versus structural flexibility. a case study of $Eu_9Cd_{4+x}Sb_9$ and $Ca_9Mn_{4+x}Sb_9$ (x ~ 1/2)," Inorganic chemistry **54**, 947–955 (2014).

[144]S. Bobev, J. D. Thompson, J. L. Sarrao, M. M. Olmstead, H. Hope, and S. M. Kauzlarich, "Probing the limits of the Zintl concept: structure and bonding in rare-earth and alkaline-earth Zinc-Antimonides $Yb_9Zn_{4+x}Sb_9$ and $Ca_9Zn_{4.5}Sb_9$," Inorganic Chemistry **43**, 5044–5052 (2004).

[145]S.-M. Park, E. S. Choi, W. Kang, and S.-J. Kim, "$Eu_5In_2Sb_6$, $Eu_5In_{2-x}Zn_xSb_6$: rare earth zintl phases with narrow band gaps," Journal of Materials Chemistry **12**, 1839–1843 (2002).

[146]S. R. Brown, E. S. Toberer, T. Ikeda, C. A. Cox, F. Gascoin, S. M. Kauzlarich, and G. J. Snyder, "Improved thermoelectric performance in $Yb_{14}Mn_{1-x}Zn_xSb_{11}$ by the reduction of spin-disorder scattering," Chemistry of Materials **20**, 3412–3419 (2008).

[147]W. G. Zeier, A. Zevalkink, Z. M. Gibbs, G. Hautier, M. G. Kanatzidis, and G. J. Snyder, "Thinking like a chemist: intuition in thermoelectric materials," Angewandte Chemie International Edition **55**, 6826–6841 (2016).

[148]E. S. Toberer, A. Zevalkink, N. Crisosto, and G. J. Snyder, "The Zintl compound $Ca_5Al_2Sb_6$ for low-cost thermoelectric power generation," Adv. Funct. Mater. **20**, 4375–4380 (2010).

[149]A. Zevalkink, J. Swallow, and G. J. Snyder, "Thermoelectric properties of Mn-doped $Ca_5Al_2Sb_6$," Journal of Electronic Materials **41**, 813–818 (2012).

[150]D. Cahill, S. Watson, and R. Pohl, "Lower limit to the thermal conductivity of disordered crystals," Phys. Rev. B **46**, 6131–6140 (1992).

[151]A. Einstein, "Planck's theory of radiation and the theory of specific heat," Ann. Phys **22**, 180–190 (1907).

[152]D. G. Cahill and R. Pohl, "Lattice vibrations and heat transport in crystals and glasses," Ann. Rev. Mater. Sci **39**, 93–121 (1988).

[153]C. Chiritescu, D. G. Cahill, N. Nguyen, D. Johnson, A. Bodapati, P. Keblinski, and P. Zschack, "Ultralow thermal conductivity in disordered, layered WSe_2 crystals," Science **315**, 351–353 (2007).

[154]R. M. Costescu, D. G. Cahill, F. H. Fabreguette, Z. A. Sechrist, and S. M. George, "Ultra-low thermal conductivity in W/Al_2O_3 nanolaminates," Science **303**, 989–990 (2004).

[155]T.-R. Wei, C.-F. Wu, W. Sun, Y. Pan, and J.-F. Li, "Is Cu_3SbSe_3 a promising thermoelectric material?" RSC Advances **5**, 42848–42854 (2015).

[156]J.-H. Pöhls, M. B. Johnson, and M. A. White, "Origins of ultralow thermal conductivity in bulk [6,6]-phenyl-C61-butyric acid methyl ester (pcbm)," Physical Chemistry Chemical Physics **18**, 1185–1190 (2016).

[157]S. B. Zhang and J. E. Northrup, "Chemical potential dependence of defect formation energies in GaAs: application to Ga self-diffusion," Phys Rev Lett **67**, 2339–2342 (1991).

[158]S. Lany and A. Zunger, "Dopability, intrinsic conductivity, and nonstoichiometry of transparent conducting oxides," Physical Review Letters **98**, 045501 (2007).

[159]C. G. Van de Walle, D. Laks, G. Neumark, and S. Pantelides, "First-principles calculations of solubilities and doping limits: Li, Na, and N in ZnSe," Physical Review B **47**, 9425 (1993).

[160]W. Shockley and J. L. Moll, "Solubility of flaws in heavily-doped semiconductors," Physical Review **119**, 1480–1482 (1960).

[161]P. Bogusl, E. Briggs, J. Bernholc, et al., "Native defects in gallium nitride," Physical Review B **51**, 17255 (1995).

[162]C. L. Condron, S. M. Kauzlarich, F. Gascoin, and G. J. Snyder, "Thermoelectric properties and microstructure of Mg_3Sb_2," Journal of Solid State Chemistry **179**, 2252–2257 (2006).

[163]T. Kajikawa, N. Kimura, and T. Yokoyama, "Thermoelectric properties of intermetallic compounds Mg_3Bi_2 and Mg_3Sb_2 for medium temp," Proceedings of the 22nd International Conference on Thermoelectrics, 2003, 305 (2003).

[164]J. W. Gibbs, "On the equilibrium of heterogeneous substances," American Journal of Science, 441–458 (1878).

[165]A. Findlay, *The phase rule and its applications* (Longmans, Green, 1906).

[166]C. Freysoldt, B. Grabowski, T. Hickel, J. Neugebauer, G. Kresse, A. Janotti, and C. G. Van de Walle, "First-principles calculations for point defects in solids," Reviews of modern physics **86**, 253 (2014).

[167]C. Suryanarayana, "Mechanical alloying and milling," Progress in Materials Science **46**, 1–184 (2001).

[168]P. Baláž, "High-energy milling," in *Mechanochemistry in nanoscience and minerals engineering* (Springer Berlin Heidelberg, Berlin, Heidelberg, 2008), pp. 103–132.

[169]M. G. Kanatzidis, R. Pöttgen, and W. Jeitschko, "The metal flux: a preparative tool for the exploration of intermetallic compounds," Angewandte Chemie International Edition **44**, 6996–7023 (2005).

[170]S.-Q. Xia and S. Bobev, "On the crystal structure of the quasicrystalline approximant $YbCd_6$ at low temperature," Intermetallics **15**, 550–556 (2007).

[171]B. Saparov, S. Bobev, A. Ozbay, and E. R. Nowak, "Synthesis, structure and physical properties of the new Zintl phases $Eu_{11}Zn_6Sb_{12}$ and $Eu_{11}Cd_6Sb_{12}$," Journal of Solid State Chemistry **181**, 2690–2696 (2008).

[172]N.-T. Suen, Y. Wang, and S. Bobev, "Synthesis, crystal structures, and physical properties of the new Zintl phases $A_{21}Zn_4Pn_{18}$ (A= Ca, Eu; Pn = As, Sb) - versatile arrangements of [ZnPn_4] tetrahedra," Journal of Solid State Chemistry **227**, 204–211 (2015).

[173]N. Kazem, W. Xie, S. Ohno, A. Zevalkink, G. J. Miller, G. J. Snyder, and S. M. Kauzlarich, "High-temperature thermoelectric properties of the solid–solution Zintl Phase $Eu_{11}Cd_6Sb_{12-x}As_x$ (x < 3)," Chemistry of Materials **26**, 1393–1403 (2014).

[174]J. S. Benjamin, "Mechanical alloying - a perspective," Metal Powder Report **45**, 122–127 (1990).

[175]J. S. Benjamin, "Dispersion strengthened superalloys by mechanical alloying," Metallurgical Transactions **1**, 2943–2951 (1970).

[176]J. S. Benjamin and T. E. Volin, "The mechanism of mechanical alloying," Metallurgical Transactions **5**, 1929–1934 (1974).

[177]C. C. Koch and J. Whittenberger, "Mechanical milling/alloying of intermetallics," Intermetallics **4**, 339–355 (1996).

[178]C. Koch, O. Cavin, C. McKamey, and J. Scarbrough, "Preparation of "amorphous" $Ni_{60}Nb_{40}$ by mechanical alloying," Applied Physics Letters **43**, 1017–1019 (1983).

[179]D. R. Maurice and T. Courtney, "The physics of mechanical alloying: a first report," Metallurgical Transactions A **21**, 289–303 (1990).

[180]M. Abdellaoui and E. Gaffet, "The physics of mechanical alloying in a planetary ball mill: mathematical treatment," Acta metallurgica et materialia **43**, 1087–1098 (1995).

[181]P. Le Brun, L. Froyen, and L. Delaey, "The modelling of the mechanical alloying process in a planetary ball mill: comparison between theory and in-situ observations," Materials Science and Engineering: A **161**, 75–82 (1993).

[182]C. F. Burmeister and A. Kwade, "Process engineering with planetary ball mills," Chemical Society Reviews **42**, 7660–7667 (2013).

[183]P. Raghuraman, R. R. Raman, and B. Pitchumani, "Studies in fine grinding in an attritor mill," Developments in Mineral Processing **13**, C4–94 (2000).

[184]R. M. Davis, B. McDermott, and C. C. Koch, "Mechanical alloying of brittle materials," Metallurgical Transactions A **19**, 2867–2874 (1988).

[185]*Spex sampleprep*, `http://www.spexsampleprep.com/mixermill`, Accessed: 2017-04-10.

[186]K. Yamada and C. C. Koch, "The influence of mill energy and temperature on the structure of the TiNi intermetallic after mechanical attrition," Journal of materials research **8**, 1317–1326 (1993).

[187]J. Benjamin, "Mechanical alloying," Scientific American **234**, 40–48 (1976).

[188]P.-Y. Lee, J.-L. Yang, and H.-M. Lin, "Amorphization behaviour in mechanically alloyed Ni-Ta powders," Journal of Materials Science **33**, 235–239 (1998).

[189]P. M. Fahey, P. Griffin, and J. Plummer, "Point defects and dopant diffusion in silicon," Reviews of modern physics **61**, 289 (1989).

[190]A. D. LaLonde, T. Ikeda, and G. J. Snyder, "Rapid consolidation of powdered materials by induction hot pressing," Rev. Sci. Instrum. **82**, 025104 (2011).

[191]Z. Munir, U. Anselmi-Tamburini, and M. Ohyanagi, "The effect of electric field and pressure on the synthesis and consolidation of materials: a review of the spark plasma sintering method," Journal of Materials Science **41**, 763–777 (2006).

[192]C. J. Vineis, A. Shakouri, A. Majumdar, and M. G. Kanatzidis, "Nanostructured thermoelectrics: big efficiency gains from small features," Adv Mater **22**, 3970–80 (2010).

[193]J. J. Donovan, D. A. Snyder, and M. L. Rivers, "An improved interference correction for trace element analysis," in Proceedings of the annual meeting-electron microscopy society of america (SAN FRANCISCO PRESS, 1992), pp. 1646–1646.

[194]*Advanced electron probe micro-analyzer: jeol jxa-8200 with probe for epma*, http://web.gps.caltech.edu/facilities/analytical/probe.html, Accessed: 2017-04-8.

[195]S. Iwanaga, E. S. Toberer, A. LaLonde, and G. J. Snyder, "A high temperature apparatus for measurement of the Seebeck coefficient," Review of Scientific Instruments **82**, 063905 (2011).

[196]C. Wood, D. Zoltan, and G. Stapfer, "Measurement of Seebeck coefficient using a light pulse," Rev. Sci. Instruments **56**, 719 (1985).

[197]K. A. Borup, J. de Boor, H. Wang, F. Drymiotis, F. Gascoin, X. Shi, L. Chen, M. I. Fedorov, E. Müller, B. B. Iversen, and G. J. Snyder, "Measuring thermoelectric transport properties of materials," Energy Environ. Sci. **8**, 423–435 (2015).

[198]V. Ponnambalam, S. Lindsey, N. Hickman, and T. M. Tritt, "Sample probe to measure resistivity and thermopower in the temperature range of 300–1000 K," Review of scientific instruments **77**, 073904 (2006).

[199]H. Wang, W. D. Porter, H. Böttner, J. König, L. Chen, S. Bai, T. M. Tritt, A. Mayolet, J. Senawiratne, C. Smith, F. Harris, P. Gilbert, J. W. Sharp, J. Lo, H. Kleinke, and L. Kiss, "Transport properties of bulk thermoelectrics - an international round-robin study, part I: Seebeck coefficient and electrical resistivity," Journal of Electronic Materials **42**, 654–664 (2013).

[200]L. Van der Pauw, "A method of measuring specific resistivity and hall effect of discs of arbitrary shape," Philips Res. Rep **13**, 1–9 (1958).

[201]K. A. Borup, E. S. Toberer, L. D. Zoltan, G. Nakatsukasa, M. Errico, J. P. Fleurial, B. B. Iversen, and G. J. Snyder, "Measurement of the electrical resistivity and hall coefficient at high temperatures," Rev Sci Instrum **83**, 123902 (2012).

[202]E. H. Putley, *The hall effect and related phenomena* (Butterworth, 1960).

[203]G. S. Nolas, J. Sharp, and J. Goldsmid, *Thermoelectrics: basic principles and new materials developments*, Vol. 45 (Springer Science & Business Media, 2013).

[204]J. de Boor and V. Schmidt, "Complete characterization of thermoelectric materials by a combined van der pauw approach," Advanced Materials **22**, 4303–4307 (2010).

[205]V. K. Zaitsev, M. I. Fedorov, E. A. Gurieva, I. S. Eremin, P. P. Konstantinov, A. Y. Samunin, and M. V. Vedernikov, "Highly effective $Mg_2Si_{1-x}Sn_x$ thermoelectrics," Phys. Rev. B **74**, 045207 (2006).

[206]G. Alekseeva, E. Gurieva, P. Konstantinov, L. Prokof'eva, and M. Fedorov, "Thermoelectric figure of merit of hetero-and isovalently doped pbse," Semiconductors **30**, 1125–1127 (1996).

[207]D. G. Cahill, H. E. Fischer, T. Klitsner, E. Swartz, and R. Pohl, "Thermal conductivity of thin films: measurements and understanding," Journal of Vacuum Science & Technology A: Vacuum, Surfaces, and Films **7**, 1259–1266 (1989).

[208]D. G. Cahill, "Thermal conductivity measurement from 30 to 750 K: the 3ω method," Review of scientific instruments **61**, 802–808 (1990).

[209]B. Sales, B. Chakoumakos, R. Jin, J. Thompson, and D. Mandrus, "Structural, magnetic, thermal, and transport properties of $X_8Ga_{16}Ge_{30}$ (X = Eu, Sr, Ba) single crystals," Physical Review B **63**, 245113 (2001).

[210]A. Pope, B. Zawilski, and T. Tritt, "Description of removable sample mount apparatus for rapid thermal conductivity measurements," Cryogenics **41**, 725–731 (2001).

[211]S.-H. Lo, J. He, K. Biswas, M. G. Kanatzidis, and V. P. Dravid, "Phonon scattering and thermal conductivity in *p*-type nanostructured PbTe-BaTe bulk thermoelectric materials," Advanced Functional Materials **22**, 5175–5184 (2012).

[212]W. Parker, R. Jenkins, C. Butler, and G. Abbott, "Thermal diffusivity measurements using the flash technique," J. Appl. Phys **32**, 1679–1684 (1961).

[213]R. D. Cowan, "Pulse method of measuring thermal diffusivity at high temperatures," Journal of Applied Physics **34**, 926–927 (1963).

[214]L. Clark III and R. Taylor, "Radiation loss in the flash method for thermal diffusivity," Journal of Applied Physics **46**, 714–719 (1975).

[215]J. Cape and G. Lehman, "Temperature and finite pulse-time effects in the flash method for measuring thermal diffusivity," Journal of applied physics **34**, 1909–1913 (1963).

[216]*LFA 457 MicroFlash*, `https://www.netzsch-thermal-analysis.com/us/products-solutions/thermal-diffusivity-conductivity/lfa-457-microflash/`, Accessed: 2017-04-10.

[217]D. Zhao, X. Qian, X. Gu, S. A. Jajja, and R. Yang, "Measurement techniques for thermal conductivity and interfacial thermal conductance of bulk and thin film materials," Journal of Electronic Packaging **138**, 040802 (2016).

[218]S. C. Mraw and D. F. Naas, "The measurement of accurate heat capacities by differential scanning calorimetry comparison of DSC results on pyrite (100 to 800 K) with literature values from precision adiabatic calorimetry," The Journal of Chemical Thermodynamics **11**, 567–584 (1979).

[219]D. G. Archer, "Thermodynamic properties of synthetic sapphire (α – Al_2O_3), standard reference material 720 and the effect of temperature scale differences on thermodynamic properties," Journal of Physical and Chemical Reference Data **22**, 1441–1453 (1993).

[220]C. A. Kennedy, M. Stancescu, R. A. Marriott, and M. A. White, "Recommendations for accurate heat capacity measurements using a quantum design physical property measurement system," Cryogenics **47**, 107–112 (2007).

[221]R. Truell, C. Elbaum, and B. B. Chick, *Ultrasonic methods in solid state physics* (Academic press, 2013).

[222]A. Migliori, T. Darling, J. Baiardo, and F. Freibert, "5. resonant ultrasound spectroscopy (RUS)," Experimental Methods in the Physical Sciences **39**, 189–220 (2001).

[223]A. Migliori, J. Sarrao, W. M. Visscher, T. Bell, M. Lei, Z. Fisk, and R. Leisure, "Resonant ultrasound spectroscopic techniques for measurement of the elastic moduli of solids," Physica B: Condensed Matter **183**, 1–24 (1993).

[224]G. Kresse and J. Furthmuller, "Efficiency of ab-initio total energy calculations for metals and semiconductors using a plane-wave basis set," Comput. Mater. Sci. **6**, 15–50 (1996).

[225]J. P. Perdew, K. Burke, and M. Ernzerhof, "Generalized gradient approximation made simple," Phys. Rev. Lett. **77**, 3865–3868 (1996).

[226]J. Heyd, G. E. Scuseria, and M. Ernzerhof, "Hybrid functionals based on a screened coulomb potential," The Journal of Chemical Physics **118**, 8207–8215 (2003).

[227]J. Heyd, G. E. Scuseria, and M. Ernzerhof, "Erratum: "Hybrid functionals based on a screened coulomb potential" [J. Chem. Phys. 118, 8207 (2003)]," The Journal of Chemical Physics **124**, 219906 (2006).

[228]J. Paier, M. Marsman, K. Hummer, G. Kresse, I. C. Gerber, and J. G. Ángyán, "Screened hybrid density functionals applied to solids," The Journal of Chemical Physics **124**, 154709 (2006).

[229]S. Bajaj, H. Wang, J. W. Doak, C. Wolverton, and G. J. Snyder, "Calculation of dopant solubilities and phase diagrams of X–Pb–Se (X = Br, Na) limited to defects with localized charge," Journal of Materials Chemistry C **4**, 1769–1775 (2016).

[230]V. Ozoliņš and M. Asta, "Large vibrational effects upon calculated phase boundaries in Al-Sc," Physical Review Letters **86**, 448–451 (2001).

[231]G. Kresse and J. Hafner, "Ab initio molecular dynamics for liquid metals," Phys. Rev. B **47**, 558–561 (1993).

[232]L. E. Bell, "Cooling, heating, generating power, and recovering waste heat with thermoelectric systems," Science **321**, 1457 (2008).

[233]G. K. Madsen, "Automated search for new thermoelectric materials: the case of LiZnSb," J Am Chem Soc **128**, 12140–6 (2006).

[234]D. L. Medlin and G. J. Snyder, "Interfaces in bulk thermoelectric materials," Current Opinion in Colloid & Interface Science **14**, 226–235 (2009).

[235]E. S. Toberer, A. F. May, C. J. Scanlon, and G. J. Snyder, "Thermoelectric properties of p-type liznsb: assessment of ab initio calculations," Journal of Applied Physics **105**, 063701 (2009).

[236]S. Kim, C. Kim, Y.-K. Hong, T. Onimaru, K. Suekuni, T. Takabatake, and M.-H. Jung, "Thermoelectric properties of Mn-doped Mg-Sb single crystals," Journal of Materials Chemistry A **2**, 12311 (2014).

[237]K. X. Zhang, X. Y. Qin, H. X. Xin, H. J. Li, and J. Zhang, "Transport and thermoelectric properties of nanocrystal substitutional semiconductor alloys $(Mg_{1-x}Cd_x)_3Sb_2$ doped with Ag," Journal of Alloys and Compounds **484**, 498–504 (2009).

[238]A. Bhardwaj, N. S. Chauhan, S. Goel, V. Singh, J. J. Pulikkotil, T. D. Senguttuvan, and D. K. Misra, "Tuning the carrier concentration using Zintl chemistry in Mg_3Sb_2, and its implications for thermoelectric figure-of-merit," Phys Chem Chem Phys **18**, 6191–200 (2016).

[239]H. X. Xin, X. Y. Qin, J. H. Jia, C. J. Song, K. X. Zhang, and J. Zhang, "Thermoelectric properties of nanocrystalline $(Mg_{1-x}Zn_x)_3Sb_2$ isostructural solid solutions fabricated by mechanical alloying," Journal of Physics D: Applied Physics **42**, 165403 (2009).

[240]V. Ponnambalam and D. T. Morelli, "On the thermoelectric properties of Zintl compounds $Mg_3Bi_{2-x}Pn_x$ (Pn = P and Sb)," Journal of Electronic Materials **42**, 1307–1312 (2013).

[241]H. X. Xin and X. Y. Qin, "Electrical and thermoelectric properties of nanocrystal substitutional semiconductor alloys $Mg_3(Bi_xSb_{1-x})_2$ prepared by mechanical alloying," Journal of Physics D: Applied Physics **39**, 5331–5337 (2006).

[242]A. Bhardwaj and D. K. Misra, "Enhancing thermoelectric properties of a p-type Mg_3Sb_2- based Zintl phase compound by Pb substitution in the anionic framework," RSC Advances **4**, 34552 (2014).

[243]S. Kim, C. M. Kim, Y.-K. K. Hong, I. S. Kim, J. Hoon., T. Onimaru, T. Takabatake, and M.-H. Jung, "Thermoelectric properties of $Mg_3Sb_{2-x}Bi_x$ single crystals grown by bridgman method," Materials Research Express **2**, 055902 (2015).

[244]A. Bhardwaj, A. Rajput, A. K. Shukla, J. J. Pulikkotil, A. K. Srivastava, A. Dhar, G. Gupta, S. Auluck, D. K. Misra, and R. C. Budhani, "Mg_3Sb_2-based Zintl compound: a non-toxic, inexpensive and abundant thermoelectric material for power generation," RSC Advances **3**, 8504 (2013).

[245]D. J. Singh and D. Parker, "Electronic and transport properties of Zintl phase $Ae Mg_2 Pn_2$, Ae = Ca, Sr, Ba, Pn = As, Sb, Bi in relation to Mg_3Sb_2," Journal of Applied Physics **114**, 143703 (2013).

[246]C. M. Jaworski, V. Kulbachinskii, and J. P. Heremans, "Resonant level formed by tin in Bi_2Te_3 and the enhancement of room-temperature thermoelectric power," Physical Review B **80** (2009) 10.1103/PhysRevB.80.233201.

[247]Y. Pei, A. LaLonde, S. Iwanaga, and G. J. Snyder, "High thermoelectric figure of merit in heavy hole dominated PbTe," Energy & Environmental Science **4**, 2085 (2011).

[248]J. Shuai, J. Mao, S. Song, Q. Zhu, J. Sun, Y. Wang, R. He, J. Zhou, G. Chen, D. J. Singh, and Z. Ren, "Tuning the carrier scattering mechanism to effectively improve the thermoelectric properties," Energy & Environmental Science (2017) 10.1039/C7EE00098G.

[249]A. Zunger, "Practical doping principles," Applied Physics Letters **83**, 57 (2003).

[250]A. Zevalkink, W. G. Zeier, E. Cheng, J. Snyder, J.-P. Fleurial, and S. Bux, "Nonstoichiometry in the Zintl phase $Yb_{1-\delta}Zn_2Sb_2$ as a route to thermoelectric optimization," Chemistry of Materials **26**, 5710–5717 (2014).

[251]M. Paliwal and I.-H. Jung, "Thermodynamic modeling of the Mg-Bi and Mg-Sb binary systems and short-range-ordering behavior of the liquid solutions," Calphad **33**, 744–754 (2009).

[252]G. Grube and R. Bornhak, "The shape diagram of magnesium-antimony," Zeitschrift fur Elektrochemie und Angewandte Physikalische Chemie **40**, 140–142 (1934).

[253]U. Aydemir, J.-H. Pöhls, H. Zhu, G. Hautier, S. Bajaj, Z. M. Gibbs, W. Chen, G. Li, S. Ohno, D. Broberg, S. D. Kang, M. Asta, G. Ceder, M. A. White, K. Persson, A. Jain, and G. J. Snyder, "$YCuTe_2$: a member of a new class of thermoelectric materials with $CuTe_4$-based layered structure," Journal of Materials Chemistry A **4**, 2461–2472 (2016).

[254]S. Dongmin Kang and G. Jeffrey Snyder, "Charge-transport model for conducting polymers," Nat Mater (2016) 10.1038/nmat4784.

[255]A. A. Shabaldin, L. V. Prokofeva, G. J. Snyder, P. P. Konstantinov, G. N. Isachenko, and A. V. Asach, "The influence of weak tin doping on the thermoelectric properties of zinc antimonide," Journal of Electronic Materials **45**, 1871–1874 (2016).

[256]Y. Tang, S.-w. Chen, and G. J. Snyder, "Temperature dependent solubility of Yb in Yb-$CoSb_3$ skutterudite and its effect on preparation, optimization and lifetime of thermoelectrics," Journal of Materiomics **1**, 75–84 (2015).

[257]Y. Tang, R. Hanus, S.-w. Chen, and G. J. Snyder, "Solubility design leading to high figure of merit in low-cost Ce-$CoSb_3$ skutterudites," Nature Communications **6**, 7584 (2015).

[258]Y. Tang, Y. Qiu, L. Xi, X. Shi, W. Zhang, L. Chen, S.-M. Tseng, S.-w. Chen, and G. J. Snyder, "Phase diagram of In-Co-Sb system and thermoelectric properties of in-containing skutterudites," Energy & Environmental Science **7**, 812–819 (2014).

[259]P. Zawadzki, L. L. Baranowski, H. Peng, E. S. Toberer, D. S. Ginley, W. Tumas, A. Zakutayev, and S. Lany, "Evaluation of photovoltaic materials within the Cu-Sn-S family," Applied Physics Letters **103**, 253902 (2013).

[260]L. L. Baranowski, P. Zawadzki, S. Lany, E. S. Toberer, and A. Zakutayev, "A review of defects and disorder in multinary tetrahedrally bonded semiconductors," Semiconductor Science and Technology **31**, 123004 (2016).

[261]A. D. Martinez, B. R. Ortiz, N. E. Johnson, L. L. Baranowski, L. Krishna, S. Choi, P. C. Dippo, B. To, A. G. Norman, P. Stradins, V. Stevanović, E. S. Toberer, and A. C. Tamboli, "Development of $ZnSiP_2$ for Si-based tandem solar cells," IEEE Journal of Photovoltaics **5**, 17–21 (2015).

[262]A. S. Glen, "New materials and performance limits for thermoelectric cooling," in *Crc handbook of thermoelectrics* (CRC Press, 1995).

[263]W. G. Zeier, J. Schmitt, G. Hautier, U. Aydemir, Z. M. Gibbs, C. Felser, and G. J. Snyder, "Engineering half-heusler thermoelectric materials using zintl chemistry," Nature Reviews Materials, 16032 (2016).

[264]U. Aydemir, A. Zevalkink, A. Ormeci, Z. M. Gibbs, S. Bux, and G. J. Snyder, "Thermoelectric enhancement in $BaGa_2Sb_2$ by Zn doping," Chemistry of Materials **27**, 1622–1630 (2015).

[265]S. M. Kauzlarich, S. R. Brown, and G. J. Snyder, "Zintl phases for thermoelectric devices," Dalton Trans, 2099–107 (2007).

[266]S.-J. Kim, J. Salvador, D. Bilc, S. Mahanti, M. G. Kanatzidis, et al., "Yb9zn4bi9: extension of the zintl concept to the mixed-valent spectator cations," Journal of the American Chemical Society **123**, 12704–12705 (2001).

[267]H. S. E. Brechtel G. Cordier, Z. Naturforsch **34B**, 1229 (1979).

[268]Z. Wu, J. Li, X. Li, M. Zhu, K.-c. Wu, X.-t. Tao, B.-B. Huang, and S.-q. Xia, "Tuning the thermoelectric properties of $Ca_9Zn_{4+x}Sb_9$ by controlled doping on the interstitial structure," Chemistry of Materials **28**, 6917–6924 (2016).

[269]H. J. Goldsmid and J. W. Sharp, "Estimation of the thermal band gap of a semiconductor from Seebeck measurements," J. Electron. Mater. **28**, 869–872 (1999).

[270]A. Jain, S. P. Ong, G. Hautier, W. Chen, W. D. Richards, S. Dacek, S. Cholia, D. Gunter, D. Skinner, G. Ceder, et al., "Commentary: the materials project: a materials genome approach to accelerating materials innovation," Apl Materials **1**, 011002 (2013).

[271]J. E. Saal, S. Kirklin, M. Aykol, B. Meredig, and C. Wolverton, "Materials design and discovery with high-throughput density functional theory: the open quantum materials database (oqmd)," Jom **65**, 1501–1509 (2013).

[272]N. Chen, F. Gascoin, G. J. Snyder, E. Müller, G. Karpinski, and C. Stiewe, "Macroscopic thermoelectric inhomogeneities in $(AgSbTe_2)_x(PbTe)_{1-x}$," Applied Physics Letters **87**, 171903 (2005).

[273]F. M. Andrew and G. J. Snyder, "Introduction to modeling thermoelectric transport at high temperatures," in *Materials, preparation, and characterization in thermoelectrics* (CRC Press, 2012), pp. 1–18.

[274]X.-J. Wang, M.-B. Tang, J.-T. Zhao, H.-H. Chen, and X.-X. Yang, "Thermoelectric properties and electronic structure of Zintl compound $BaZn_2Sb_2$," Applied Physics Letters **90**, 232107 (2007).

[275]E. J. Skoug, J. D. Cain, and D. T. Morelli, "Structural effects on the lattice thermal conductivity of ternary antimony- and bismuth-containing chalcogenide semiconductors," Applied Physics Letters **96**, 181905 (2010).

[276]A. Zevalkink, J. Swallow, and G. J. Snyder, "Thermoelectric properties of Zn-doped $Ca_5In_2Sb_6$," Dalton Transactions **42**, 9713–9719 (2013).

[277]B. Sales, D. Mandrus, B. C. Chakoumakos, V. Keppens, and J. R. Thompson, "Filled skutterudite antimonides: electron crystals and phonon glasses," Phys. Rev. B **56** (1997).

[278]T. Caillat, J. P. Fleurial, and A. Borshchevsky, "Preparation and thermoelectric properties of semiconducting Zn_4Sb_3," Journal of Physics and Chemistry of Solids **58**, 1119–1125 (1997).

[279]C. Haas, "Spin-disorder scattering and magnetoresistance of magnetic semiconductors," Physical Review **168**, 531–538 (1968).

[280]H. Liu, X. Shi, F. Xu, L. Zhang, W. Zhang, L. Chen, Q. Li, C. Uher, T. Day, and G. J. Snyder, "Copper ion liquid-like thermoelectrics," Nat Mater **11**, 422–425 (2012).

[281]B. Yu, W. Liu, S. Chen, H. Wang, H. Wang, G. Chen, and Z. Ren, "Thermoelectric properties of copper selenide with ordered selenium layer and disordered copper layer," Nano Energy **1**, 472–478 (2012).

[282]A. M. Mills, R. Lam, M. J. Ferguson, L. Deakin, and A. Mar, "Chains, planes, and antimonides," Coord. Chem. Rev. **233**, 207–222 (2002).

[283]W. G. Zeier, A. Zevalkink, E. Schechtel, W. Tremel, and G. J. Snyder, "Thermoelectric properties of Zn-doped Ca_3AlSb_3," Journal of Materials Chemistry **22**, 9826 (2012).

[284]M. Christensen, A. B. Abrahamsen, N. B. Christensen, F. Juranyi, N. H. Andersen, K. Lefmann, J. Andreasson, C. R. Bahl, and B. B. Iversen, "Avoided crossing of rattler modes in thermoelectric materials," Nat Mater **7**, 811–5 (2008).

[285]A. M. Guloy, R. Ramlau, Z. Tang, W. Schnelle, M. Baitinger, and Y. Grin, "A guest-free germanium clathrate," Nature **443**, 320–3 (2006).

[286]I. Bednar, E. Royanian, S. Bühler-Paschen, E. Bauer, N. Nasir, A. Grytsiv, N. Melnychenko-Koblyuk, and P. Rogl, "Giant thermopower at low temperatures in novel clathrates $Ba_8(Cu,Zn)_xGe_{46-x}$," Journal of Electronic Materials **39**, 1687–1691 (2010).

[287]T. Yi, C. A. Cox, E. S. Toberer, G. J. Snyder, and S. M. Kauzlarich, "High-temperature transport properties of the Zintl phases $Yb_{11}GaSb_9$ and $Yb_{11}InSb_9$," Chemistry of Materials **22**, 935–941 (2010).

[288]H. Hua, A. Zevalkink, Z. M. Gibbs, G. J. Snyder, and S. Bobev, "Synthesis, structural characterization, and physical properties of the Type-I clathrates $A_8Zn_{18}As_{28}$ (A = K, Rb, Cs) and $Cs_8Cd_{18}As_{28}$," Chem. Mater. (2012).

[289]G. Nolas, G. A. Slack, D. Morelli, T. M. Tritt, and A. C. Ehrlich, "The effect of rare-earth filling on the lattice thermal conductivity of skutterudites," J. Appl. Phys **79** (1996).

[290]H. Kleinke, "New bulk materials for thermoelectric power generation: clathrates and complex antimonides," Chemistry of Materials **22**, 604–611 (2010).

[291]X. Shi, Y. Pei, G. J. Snyder, and L. Chen, "Optimized thermoelectric properties of $Mo_3Sb_{7-x}Te_x$ with significant phonon scattering by electrons," Energy & Environmental Science **4**, 4086 (2011).

[292]S. R. Brown, S. M. Kauzlarich, F. Gascoin, and G. Jeffrey Snyder, "High-temperature thermoelectric studies of $A_{11}Sb_{10}$ (A = Yb, Ca)," Journal of Solid State Chemistry **180**, 1414–1420 (2007).

[293]Y. Wu, A. P. Litvinchuk, E. S. Toberer, G. J. Snyder, N. Newman, A. Fischer, E. W. Scheidt, W. Scherer, and U. Haüssermann, "Thermoelectric properties of $Zn_5Sb_4In_{2-\delta}$ (δ = 0.15)," Journal of Applied Physics **111**, 123712 (2012).

[294]A. Prokofiev, A. Sidorenko, K. Hradil, M. Ikeda, R. Svagera, M. Waas, H. Winkler, K. Neumaier, and S. Paschen, "Thermopower enhancement by encapsulating cerium in clathrate cages," Nat Mater **12**, 1096–1101 (2013).

[295]M. Lundstrom, *Fundamentals of carrier transport* (Cambridge University Press, 2009).